Spectroscopic Studies of Three Novae

V. P. Arkhipova[*], M. A. Burlak, and V. F. Esipov

Sternberg Astronomical Institute, Universitetskii pr. 13, Moscow, 119899 Russia
Received July 16, 2001; in final form, September 27, 2001

Abstract—We present our spectroscopic observations of the novae V1425, V1493, and V1494 Aql carried out with the 125-cm telescope at the Crimean Station of the Sternberg Astronomical Institute in the wavelength range 4000–11 000 Å. We measured the emission-line intensities, determined the nova shell expansion velocities from the line profile FWHMs and components, and estimated the interstellar reddening from the first members of the Balmer series. The chemical composition of the nova shells is analyzed. Nitrogen and oxygen were found to be overabundant in V1425 and V1494 Aql; the helium abundance turned out to be normal in the two stars. © *2002 MAIK "Nauka/Interperiodica"*.

Key words: *novae, spectroscopic studies, shell chemical composition*

INTRODUCTION

Novae are the product of a late evolutionary stage of binary components. In a close binary, the material lost by the less massive lobe-filling red component is accreted onto the hot white dwarf that evolved from the more massive component. When the accreted material reaches a critical mass, a thermonuclear flash occurs on the white-dwarf surface, and we observe a nova outburst. The outburst development rate and strength significantly depend on white-dwarf parameters: the mass and surface chemical composition. The CNO elements in the most luminous and fastest novae are currently believed to be overabundant. The numerous abundance determinations for nova shells available to date are in poor agreement with theoretical predictions. In particular, a correlation between the CNO abundances and the brightness decline rate is barely traceable. Progress in establishing the chemical composition of novae and its relationship to stellar evolution can be made both by increasing the quantity and quality of observational data and by improving the theory of nucleosynthesis at late stages of stellar evolution. Accordingly, we set the objective of investigating the shell chemical composition for all the recent novae accessible to observation. Our study of three novae that erupted in 1995–1999 is part of this program and the subject of this paper.

OBSERVATIONAL DATA AND THEIR REDUCTION

All nova spectra were taken at the Crimean Station of the Sternberg Astronomical Institute at the Cassegrain focus of the 125-cm reflector with a fast spectrograph. The detectors were SBIG ST-6 and ST-6I CCD arrays with 375×242 pixels and, in the spectral mode, with 750×242 pixels. The spectral resolution with a 600 lines mm^{-1} diffraction grating was ≈ 6 Å per pixel and ≈ 3 Å per pixel in the spectral mode. The observed spectral range was 4000–11000 Å. The complete nova spectrum consisted of two (occasionally three or four) partially overlapping frames that corresponded to different grating rotation angles. The spectral range of each frame was ≈ 2000 Å. We took several frames with different exposure times and chose the best ones in our data reduction.

First, we preprocessed the frames with the ST6 and ST-6I programs supplied with the CCD arrays. Next, we corrected the frames for the CCD spectral sensitivity and for the atmosphere by using the observed standard stars. Their absolute energy distributions (in erg cm^{-2} s^{-1} Å^{-1}) were taken from the spectrophotometric catalog by Glushneva *et al.* (1982). The airmass difference between the standard and program stars did not exceed 0.1 and was disregarded in our data reduction. The spectra were calibrated with the ESIP.EXE and KOEF.EXE programs written by A.M. Tatarnikov. Subsequently, we used the SPE program written by S. Sergeev at the Crimean Astrophysical Observatory to process the spectra.

The line intensities were determined by using this program. Weak lines were always measured in the spectra with the highest signal-to-noise ratio, generally the spectra with the longest exposure time. Strong lines were measured in all the spectra where

[*]E-mail: `vera@sai.msu.ru`

Table 1. Spectroscopic observations of V1425 Aql

Date (1995)	Δt, days	m_V	Spectral range	Exposure time, s
May 28	124	~12	1	180
			2	180
			3	180
			4	180
May 29	125	~12	1	600
			2	600, 60
			3	600
			4	600
July 26	183	~12.6	1	900
			2	900
			3	900
			4	1200
Sep. 2	221	~12.8	3	1200
			4	1800

Table 2. Spectroscopic observations of V1493 Aql

Date (1999)	Δt, days	m_V	Spectral range	Exposure time, s
July 17	4	~11	1	600
			2	600, 180, 60
			3	600
July 19	6	~11.6	2	600
			3	600
			4	1800
July 21	8	~12	1	600, 1800
			2	600, 60
July 22	9	~12	1	60, 1800
			2	60,60
Aug. 4	22	~13	1	1800
			2	1200, 60, 180
			3	1200
Sep. 16	65	~15	1	1800
			2	1800, 180
Oct. 18	97	~16	2	1800
Nov. 2	112	~15	1	1800
Nov. 5	115	~16	1	3600

they were not saturated. For each date of observation, we calculated a mean. We estimated the accuracy of measuring the intensities of weak lines to be 30%.

Our observational data are given in Tables 1–3. These tables also list Δt, the epoch after maximum light, and m_V, the magnitude of the star at this epoch estimated from the overall light curves constructed below. We carried out the spectroscopic observations of V1425 Aql and V1494 Aql when the two novae were at the nebular stage. The spectroscopic observations of V1493 Aql began on day 4 after maximum light and continued until the nebular phase. The numbers in the Spectral range columns denote the following wavelength ranges: 1—4000–5800 Å, 1.5—4750–6650 Å, 2—5700–7600 Å, 3—7500–9400 Å, and 4—9300–11000 Å.

AN OVERVIEW OF THE NOVAE STUDIED

Light Curves

The nova V1425 Aquilae was discovered on February 7, 1995 (Takamizava 1995), when its apparent magnitude was ~8^m. According to Kolotilov *et al.* (1996), this occurred ≤20 days after its

outburst and ≤10 days after the onset of brightness decline. The nova V1493 Aql was discovered on July 13, 1999 (Tago 1999) near maximum light, when its apparent magnitude was 8^m8. The nova V1494 Aql was discovered when its brightness was rising. Figures 1–3 show the overall light curves of the novae that were constructed from the various estimates taken from IAU Circulars (2000) and, for V1425 Aql, from the data in Kolotilov *et al.* (1996). Table 4 presents the photometric parameters of the novae that we obtained from the overall light curves and took from three other papers. The data sources are indicated in the table as follows: (1)—Mason *et al.* (1996); (2)—Kolotilov *et al.* (1996); (3)—this paper; and (4)—Kiss and Thomson (2000). The nova types, as inferred from the brightness decline rate, are given according to the classification by Payne-Gaposchkin (1957); the luminosities were determined from t_{2V}.

Color Excesses

We determined the color excesses $E(B-V)$ from our measured Balmer decrement by using mostly the first Balmer lines. Theoretical values of the decrement

Table 3. Spectroscopic observations of V1494 Aql

Date (2000)	Δt, days	m_V	Spectral range	Exposure time, s
Mar. 30	118	≥ 10	1	300, 60
			2	300, 60
			3	300
May 8	175	≥ 10	1	300
			2	300, 60
			3	600
			4	1200
May 26	175	≥ 10	1	600, 180
			2	600, 180, 60
			3	1200
			4	1800
June 30	210	≥ 10	1	1200, 180
			2	600, 60
July 2	212	≥ 10	1	1200, 60
			2	1200, 60
			3	1200
			4	1800
July 24	234	≥ 10	1	1800, 60
			1.5	600
			2	1200, 60
			3	1200
			4	1800
Sep. 3	275	≥ 10	1	1800, 300
			2	1200, 300
Sep. 29	301	≥ 10	1	1800, 300
			2	1800
			3	1800
Oct. 25	327	≥ 10	1	1800
			2	1800

were taken from Aller (1984). Our results are presented in Table. 4.

EVOLUTION OF THE NOVA SPECTRA OVER THE OBSERVING PERIOD

V1425 Aquilae. No significant changes occurred in the spectrum over the observing period. The spectrum exhibited Balmer hydrogen lines ($H\alpha$, $H\beta$, $H\gamma$);

lines of neutral and ionized helium (He I $\lambda5876$ Å, $\lambda6678$ Å, $\lambda7065$ Å, He II $\lambda4686$ Å); permitted and forbidden lines of singly and doubly ionized nitrogen (N II $\lambda5680$ Å, [N II] $\lambda5755$ Å, N III $\lambda4640$ Å); and forbidden lines of oxygen ([O I] $\lambda6300$ Å, $\lambda6364$ Å, [O II] $\lambda7320 + 7330$ Å, [O III] $\lambda4363$ Å, $\lambda4959$ Å, $\lambda5007$ Å), argon ([Ar III] $\lambda7135$ Å, [Ar IV] $\lambda7236$ Å, [Ar V] $\lambda7006$ Å), and iron ([Fe VII] $\lambda6087$ Å). Noteworthy among the weak lines is a blend of forbidden iron lines, [Fe VI] $\lambda5146 + 5176$ Å, and the [Ca V] $\lambda5309$ Å line. The May 29, 1995 spectrum of V1425 Aql is shown in Fig. 4.

V1493 Aquilae. The July 1999 spectra exhibited Balmer hydrogen lines, lines of ionized iron (37, 38, 42, 48, 49, 74 multiplets), N II $\lambda5680$ Å, and, possibly, He I $\lambda5876$ Å. On August 4 ($\Delta t = 22^d$), the iron lines disappeared, although an unresolvable feature near 5000 Å remained. However, nebular lines began to grow on this date. An intense line of ionized oxygen, [O II] $\lambda7320 + 7330$ Å, and the [N II] $\lambda5755$ Å line appeared. On September 16 ($\Delta t = 65^d$), V1493 Aql was at the nebular phase. The He I $\lambda6678$ Å, $\lambda7065$ Å and [O I] $\lambda6300$, $\lambda6364$ Å lines appeared. The nebular [O III] $\lambda5007$ Å line split up into two components with a separation of $\sim$2800 km s^{-1}. By the last (in time) observations ($\Delta t = 112^d$ and $\Delta t = 115^d$), only the Balmer hydrogen lines and the forbidden oxygen and nitrogen lines remained in the spectrum. All lines in the spectrum of V1493 Aql were broad. Figures 5 and 6 show the spectrum of V1493 Aql.

V1494 Aquilae. By the beginning of its observations, V1494 Aql was at the nebular phase. The spectrum exhibited Balmer hydrogen lines, lines of neutral and ionized helium (He I $\lambda5876$ Å, $\lambda6678$ Å, $\lambda7065$ Å; He II $\lambda4686$ Å, $\lambda5411$ Å); lines of ionized oxygen ([O II] $\lambda7320$ Å, $\lambda7330$ Å, [O III] $\lambda4363$ Å, $\lambda4959$ Å, $\lambda5007$ Å); lines of singly and doubly ionized nitrogen (N II $\lambda5678$ Å, [N II] $\lambda5755$ Å, N III $\lambda4640$ Å), [Fe VII] $\lambda6087$ Å; broad blends of [Fe VI] $\lambda5146$ Å, [Fe VII] $\lambda5159$ Å, [Fe VI] $\lambda5176$ Å, and [Ar III] $\lambda5191$ Å; as well as [O I] $\lambda6300$ Å, He II $\lambda6310$ Å, [O I] $\lambda6364$ Å and, possibly, [Fe X] $\lambda6374$ Å. Over the entire observing period, all lines were broad, FWHM = 2700$-$3100 km s^{-1}, and flat topped. The strongest lines split up into three components, with the central component generally being weakest. There was no such splitting at the beginning of our observations in the [Fe VII] $\lambda6087$ Å line. The profile splitting

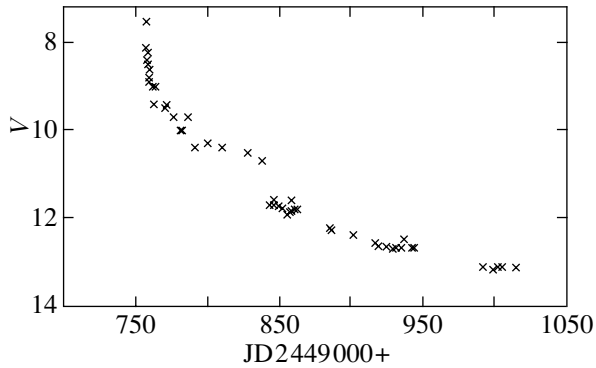**Fig. 1.** The light curve of V1425 Aql.

into components was most distinct in $H\alpha$ and [O III] $\lambda 5007$ Å (Figs. 7–10).

Later, the O VI $\lambda 5291$ Å and $\lambda 6195$ Å lines showed up; they were also broad but with unsplit sharp tops: O VI $\lambda 5291$ Å appeared on May ($\Delta t \geq 150^d$), and O VI $\lambda 6195$ Å appeared on July ($\Delta t \geq 213^d$). Before this time, something weak and shapeless was observed at the positions of these lines. On June 30 ($\Delta t \cong 210^d$), the [Fe VII] $\lambda 5721$ Å line was clearly present, and the [Fe VII] $\lambda 6087$ Å line exhibited a three-component profile. On May 26 ($\Delta t \cong 175^d$), the [Fe X] $\lambda 6374$ Å line assumed a characteristic flat shape, and its presence was beyond question. With the passage of time, the line top sharpened as in O VI. Noteworthy among the weak lines is the N III $\lambda 4515$ Å line. Of the unidentified lines, we mention the $\sim\lambda 5940$ Å (N II?, [Mn VI]?) and $\sim\lambda 6480$ Å (N III?) features, which were also characteristically flat topped.

With the passage of time, the nebular lines, the lines of ionized helium, and the O VI, [Fe VII], and [Fe X] lines strengthened, while the He I lines weakened, fading away. An idea of the spectral evolution of V1494 Aql can be gotten from Figs. 11–12.

EXPANSION VELOCITIES OF THE V1425 Aql, V1493 Aql, AND V1494 Aql SHELLS

The spectrum of V1425 Aql exhibited narrow lines. The expansion velocities measured from full widths at half maximum (FWHM) are given in Table 5. The mean velocity was 1400 km s^{-1}. However, the velocities determined from nebular lines exceed 1600 km s^{-1}.

In the spectrum of V1493 Aql, all lines were broad and had complex multicomponent profiles. Since there is virtually no isolated line, the measured widths of even moderately intense lines are very uncertain. Only the Balmer hydrogen lines were clearly distinguishable. These were used to estimate the shell expansion velocities. Table 6 gives the expansion velocities measured from the Balmer-line FWHMs. The mean velocity was 3400 km s^{-1}.

For V1494 Aql, the profiles of almost all lines showed a characteristic tabletop shape with a double- or often triple-peaked top without extended wings. High-excitation lines, such as O VI $\lambda 5291$ Å and [Fe X] $\lambda 6374$ Å, were unsplit, and had broad wings and sharp tops. We measured the separations between the extreme profile components for various lines. The results are presented in Table 7. The splitting was largest in $H\alpha$ and in lines of neutral helium (≥ 2100 km s^{-1}) and smallest in the [O II] $\lambda 7320 + 7330$ Å line. We also measured the line FWHMs. The expansion velocity was, on the average, 2800 km s^{-1}. However, the velocity determined from the nebular [O III] $\lambda 5007$ Å line is ≥ 3100 km s^{-1}. The velocities derived from the FWHMs are given in Table 8.
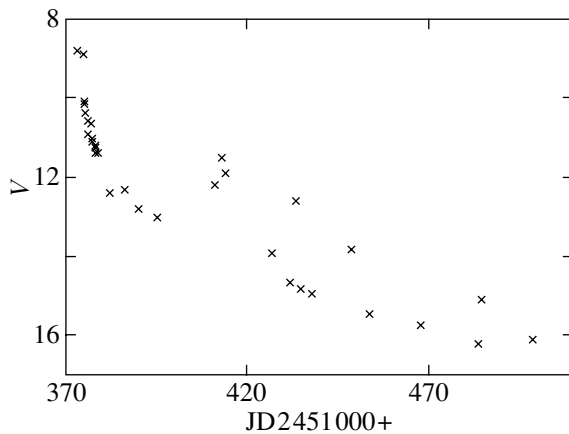

Fig. 2. The light curve of V1493 Aql.
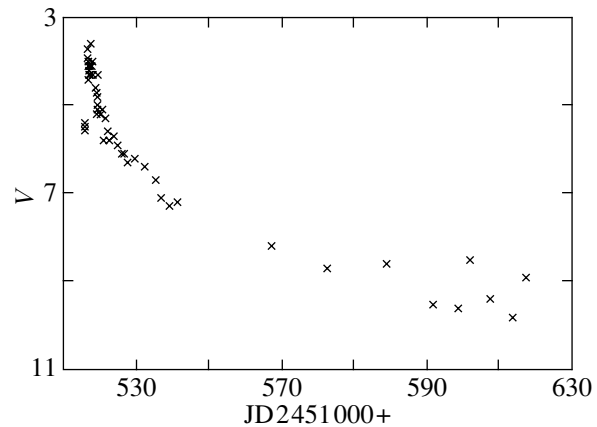

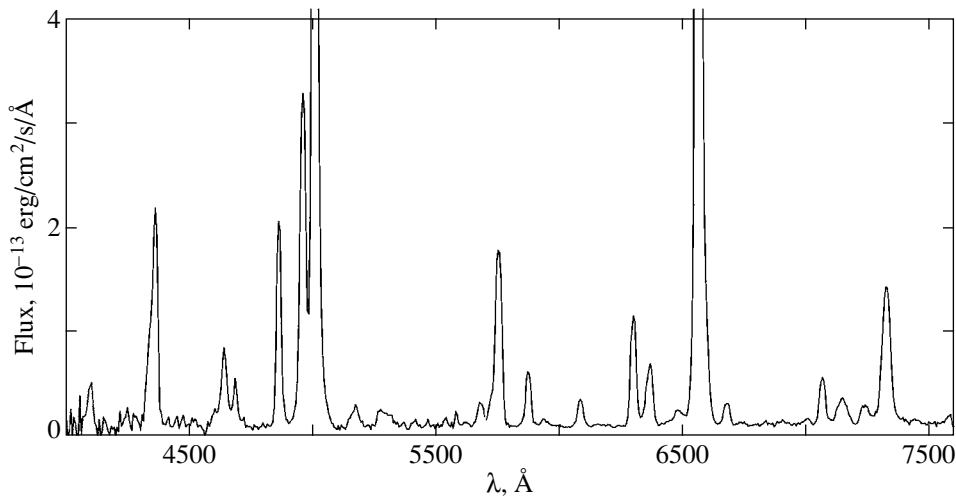**Fig. 3.** The light curve of V1494 Aql.

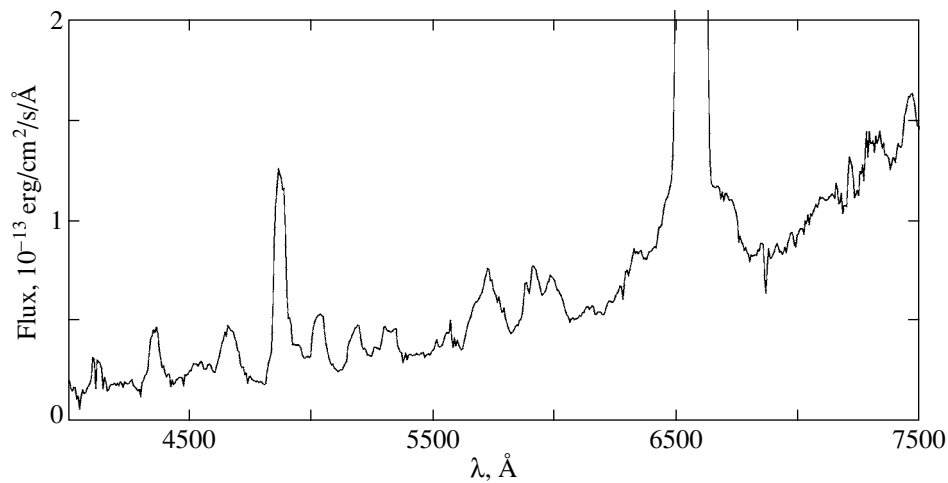**Fig. 4.** The 4000−7600 Å spectrum of V1425 Aql.

Fig. 5. The 4000−7500 Å spectrum of V1493 Aql taken on July 21, 1999.

EMISSION LINE INTENSITIES

To determine the color excess, we measured only the Balmer hydrogen lines in the spectrum of V1493 Aql and almost all the identified lines whose intensities exceeded one hundredth of the $H\beta$ intensity in the spectra of V1425 Aql and V1494 Aql. Below, to determine the chemical composition of these novae, we corrected the line intensities for interstellar reddening by using the derived color excesses.

Some lines in the spectrum of V1494 Aql turned out to be blended. Since we failed to resolve blends by reconstructing the profiles of individual lines because of the complex line shape, we had to act differently in each case. Thus, for example, to determine the helium abundance required separating the He II $\lambda4686$ Å line from the blend with N III $\lambda4640$ Å. This procedure

was carried out manually: the blend was simply divided in two at the central wavelength. This method yielded a rough, but, in our view, quite plausible estimate of the He^{++} abundance in the V1494 Aql shell. In addition, the [Fe VII] $\lambda5721$ Å and [N II] $\lambda5755$ Å lines have been blended since July 2000. To separate the nitrogen lines, we subtracted the intensity of [Fe VII] $\lambda6087$ Å multiplied by 0.65 (Nussbaumer and Storey 1982) from the blend intensity.

All the measured line intensities uncorrected for interstellar reddening are given in Tables 9 and 10.

THE ELECTRON TEMPERATURE AND DENSITY IN THE NOVA SHELLS

To determine the plasma parameters in the shell of V1425 Aql, we used the line ratios $R(\text{O III}) =$
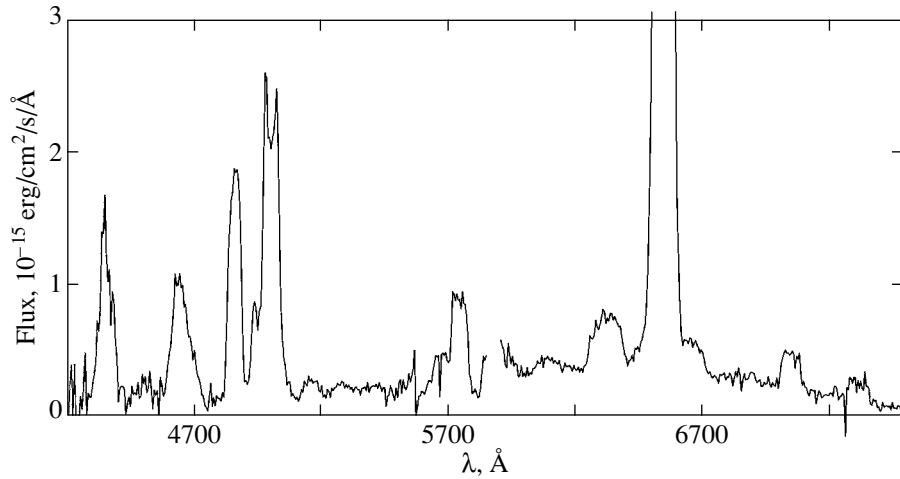
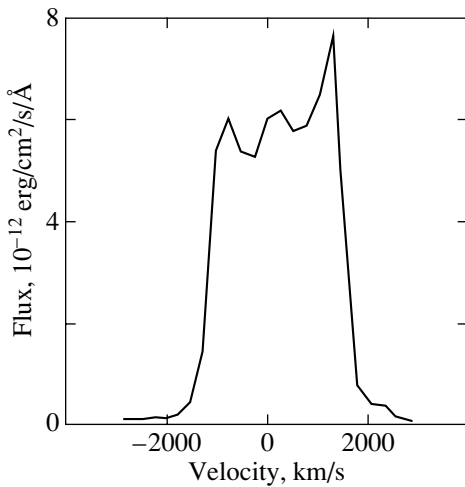**Fig. 6.** The 4200–7500 Å spectrum of V1493 Aql taken on September 16, 1999.

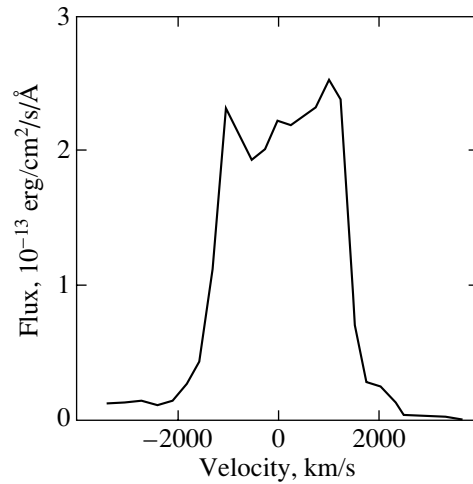**Fig. 7.** The $H\alpha$ profile in the spectrum of V1494 Aql taken on May 26, 2000.

Fig. 8. The $H\alpha$ profile in the spectrum of V1494 Aql taken on October 25, 2000.

$(I(\lambda4959) + I(\lambda5007))/I(\lambda4363)$ and $I(\lambda5176)/I(\lambda5146)$, which depend on the electron temperature T_e and density N_e. The theoretical data that show a dependence of these ratios on the plasma parameters were taken from De Robertis *et al.* (1987) for [O III] and from Nussbaumer and Storey (1978) for [Fe VI]. The temperature and density were assumed to be constant over the entire volume of the nebula. For V1425 Aql, we obtained the following gas parameters:

I. May 28 and 29, 1995: $N_e = 7 \times 10^6$ cm^{-3}, $T_e = 12000$ K;

II. June 26, 1995: $N_e = 4 \times 10^6$ cm^{-3}, $T_e = 12000$ K.

V1494 Aql exhibited broad lines with complex profiles. We failed to resolve the blend of [Fe VI]

$\lambda5146$ Å and $\lambda5176$ Å. Since we had only one ratio, R(O III), at our disposal to determine the temperature and electron density, we took a constant temperature of 11000 K for all the epochs of observations. This value is the mean for novae at the nebular phase (Snijders 1990). We estimated the electron density from R(O III). The temperature and density were assumed to be constant over the entire volume of the nebula. We used the following gas parameters in our chemical composition calculations for V1494 Aql:

I. May 8 and 26, 2000: $N_e = 4 \times 10^7$ cm^{-3}, $T_e = 11000$ K;

II. June 30, July 2 and 24, 2000: $N_e = 2 \times 10^7$ cm^{-3}, $T_e = 11000$ K;

III. September 3 and 29, October 25, 2000: $N_e = 10^7$ cm^{-3}, $T_e = 11000$ K.

**Table 4.** Photometric parameters and distances of the novae

Parameter	V1425 Aql	V1493 Aql	V1494 Aql
JD_{max}	2449742.5 ± 4.0 (1)	2451373 (3)	2451515 (3)
t_2	11^d (1)	3^d (3)	6^d (3), 6.6 ± 0^d5 (4)
t_3	$\approx 39^d$ (2)	7^d (3)	15^d (3), 16 ± 0^d5 (4)
$m_{V\,max}$	$5^m9 - 6^m5$ (1)	8^m8 (3)	3^m7 (3)
	$\approx 7^m4$ (2)		
$M_{V\,max}$	-8^m6 (1)	-9^m6 (3)	-8^m8 (3)
	$\approx -7^m5$ (2)		
$E(B-V)$	≥ 0.53(1), 0.65(2), 1(3)	≈ 1.5(3)	0.66 (3)
Type	F	vF	vF
D	$3.6-4.8$ kpc (1), 3.7 kpc (2)	4.2 kpc (3)	1.2 kpc (3)

DETERMINING THE CHEMICAL COMPOSITION OF THE NOVA SHELLS

Helium

The total helium abundance is the sum of the He^0, He^+, and He^{++} abundances. The unobservable ionization state He^0 is disregarded, because the entire helium in the nova shell is assumed to be ionized. We determined the He^+ abundance from the He I $\lambda 5876$ Å and $\lambda 6678$ Å lines (Aller 1984):

$$\log \frac{N(He^+)}{N(H^+)} = -0.133 + 0.235$$

$$\times \log t_e + \log \frac{I(\lambda 5876)}{I(H\beta)},$$

$$\log \frac{N(He^+)}{N(H^+)} = 0.851 + 0.216 \times \log t_e$$
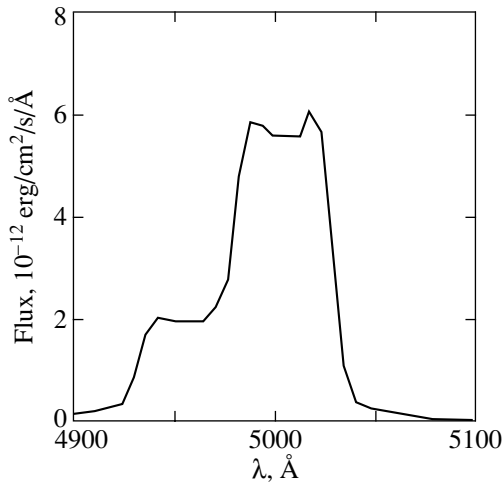
$$+ \frac{0.0158}{t_e} + \log \frac{I(\lambda 6678)}{I(H\alpha)},$$

where $t_e = T_e/10^4$ K.

The He^{++} abundance was determined from the $\lambda 4686$ Å line (Aller 1984):

$$\log \frac{N(He^{++})}{N(H^+)} = -1.077 + 0.135 \times \log t_e$$

$$+ \frac{0.135}{t_e} + \log \frac{I(\lambda 4686)}{I(H\beta)}.$$

To obtain the true He^+ abundance, we must allow for the collision excitation of the He I $2s^2\,^3S$ metastable level, whose contribution increases with electron density. The method of allowance and the correction factor C/R as a function of the temperature and density are given in Clegg (1987).
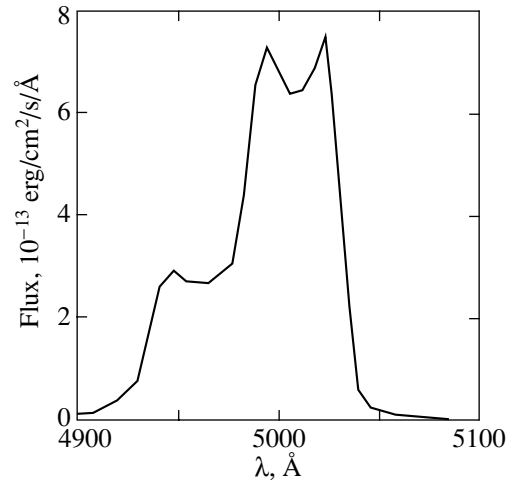
Fig. 9. The nebular line profile in the spectrum of V1494 Aql taken on May 8, 2000.

Fig. 10. The nebular line profile in the spectrum of V1494 Aql taken on October 25, 2000.

Table 5. The expansion velocity of the V1425 Aql shell as derived from the FWHM, in km s^{-1}

λ, Å	May 28, 1995	May 29, 1995	July 7, 1995	Mean
4640	1700	1700	1760	1720
$H\beta$	1300	1340	1340	1330
4959	1720	1720	1580	1670
5007	1670	1680	1560	1640
5755	1600	1610	1460	1660
5876	1290	1330	1450	1360
6087	1320	1290	1180	1260
6300	1350	1330	1220	1300
$H\alpha$	1230	–	1270	1250
6678	1340	1330	1200	1290
7065	1230	1180	1180	1200
7325	1650	1630	1460	1580

The results are presented in Table 11. The mean helium abundances were taken to be $\langle He/H \rangle = 0.11$ for V1425 Aql and $\langle He/H \rangle = 0.14$ for V1494 Aql.

Oxygen

The oxygen abundance was calculated by two methods: first, by adding up all the observable ionization stages:

$$\frac{O}{H} = \frac{O^0(\lambda 6300)}{H^+(H\beta)} + \frac{O^+(\lambda 7325)}{H^+(H\beta)} + \frac{O^{++}(\lambda 5007)}{H^+(H\beta)},$$

and, second, by using the He/He$^+$ ratio as the ICF (Aller 1984):

$$\frac{O}{H} = \left[\frac{O^+(7320 + 7330) + O^{++}(5007)}{H^+(H\beta)} \right] \times \frac{He}{He^+}.$$

The ionization correction factor (ICF) was used to allow for the unobservable ionization stages of the element. It is calculated by assuming that the abundance ratios of two ions with approximately equal ionization potentials are equal to the ratio of their total abundances. Since the first formula disregards the higher ionization stages, it gives only a lower limit on the oxygen abundance. We used this method only for V1425 Aql, because we failed to separate the [O I] $\lambda 6300$ Å line from the blend with He II $\lambda 6310$ Å in the spectrum of V1494 Aql.

Table 6. The expansion velocities of the V1493 Aql shell as derived from the FWHMs for $H\beta$ and $H\alpha$, in km s^{-1}

Date (1999)	$H\beta$	$H\alpha$
July 17	3300	3610
July 21	3220	3540
July 22	3160	3450
Aug. 4	3360	3180
Sept. 16	3400	3120
Oct. 18	–	3640

The results of our calculations are presented in Table 12. For V1425 Aql, the estimate obtained by the first method (the next-to-last column) agrees with the estimate obtained by the second method (the last column). The mean oxygen abundances were taken to be $\langle O/H \rangle = 1.5 \times 10^{-3}$ for V1425 Aql and $\langle O/H \rangle = 1.9 \times 10^{-2}$ for V1494 Aql.

Nitrogen

The nitrogen abundance was calculated by three methods: first, by adding up all the observable ionization stages (for V1425 Aql alone):

$$\frac{N}{H} = \frac{N^+(\lambda 5755)}{H^+(H\beta)} + \frac{N^{2+}(\lambda 5680)}{H^+(H\beta)} + \frac{N^{3+}(\lambda 4640)}{H^+(H\beta)},$$

second, by using the He/He$^+$ ratio as the ICF (Aller 1984):

$$\frac{N}{H} = \left[\frac{N^+(\lambda 5755) + N^{++}(\lambda 5680)}{H^+(H\beta)} \right] \times \frac{He}{He^+},$$

and, third, by using the O/O$^+$ ratio as the ICF (Aller 1984):

$$\frac{N}{H} = \frac{N^+}{H^+} \times \frac{O}{O^+}.$$

For V1425 Aql, the $\lambda 5680$ Å line was used in the abundance determination by the first and second methods. It always gives a large nitrogen abundance, which may be due to its peculiar excitation. In our case, the first and second estimates proved to be an order of magnitude larger than the third estimate. Therefore, we retained two values for the nitrogen abundance: those obtained with and without the $\lambda 5680$ Å line, $\langle N/H \rangle = 2.3 \times 10^{-2}$ and $\langle N/H \rangle = 4.2 \times 10^{-3}$, respectively. For V1494 Aql, we disregarded N^{++}; accordingly, the estimate obtained with the He/He$^+$ ratio is a lower limit on the

Table 7. The expansion velocities of the V1494 Aql shell (in km s^{-1}) as estimated from the separation between the extreme profile peaks

Date (2000)	$H\beta$	$\lambda5007$ Å	$\lambda5755$ Å	$\lambda5876$ Å	$\lambda6087$ Å	$H\alpha$	$\lambda7065$ Å	$\lambda7325$ Å
Mar. 30	1790	1740	2110	2120	–	2200	2080	1720
May 8	1790	1740	2110	2040	–	2100	2080	1470
May 26	1790	1740	2110	2040	–	2100	2080	1680
June 30	1420	2040	2110	2070	1970	2060	2080	1680
July 2	1610	2040	1820	2220	1970	2330	2290	1680
July 24	1610	1720	1980	2110	1950	2170	2080	1680
Sept. 3	1790	2040	2090	2110	1970	2100	–	1580
Sept. 29	1790	1740	2110	–	1970	2060	–	1470
Oct. 25	1790	1740	–	–	2250	2060	–	1560
Mean	1710	1840	2060	2100	2010	2130	2120	1610

Table 8. The expansion velocities of the V1494 Aql shell (in km s^{-1}) as estimated from the line FWHMs

Date (2000)	$H\beta$	$\lambda5007$ Å	$\lambda5755$ Å	$\lambda5876$ Å	$\lambda6087$ Å	$H\alpha$	$\lambda7065$ Å	$\lambda7325$ Å
Mar. 30	2900	3070	2790	2790	–	2910	2750	2770
May 8	2850	3100	2780	2800	2990	2690	2770	2800
May 26	2870	3170	2780	2760	2820	2720	2810	2790
June 30	2920	3110	2870	2780	2790	2800	2890	2770
July 2	2900	3120	2870	2770	2860	2750	2840	2720
July 24	2890	3350	2820	2800	2820	2710	3020	2800
Sept. 3	2950	3030	2730	2810	2800	2760	–	2790
Sept. 29	2910	3000	2740	–	2790	2710	–	2790
Oct. 25	2940	3150	–	–	2820	2720	–	2890
Mean	2900	3120	2800	2790	2840	2750	2850	2790

nitrogen abundance. The mean nitrogen abundances determined by different methods (using the He/He$^+$ and O/O$^+$ ratios as the ICF) differ by a factor of 30. We retained two mean values for the nitrogen abundance: those obtained with helium and oxygen, $\langle N/H \rangle = 1.5 \times 10^{-3}$ and $\langle N/H \rangle = 4.3 \times 10^{-2}$, respectively. The results for the two novae are presented in Table 13.

Argon

The argon abundance was determined only for V1425 Aql, because the spectrum of V1494 Aql exhibited no detectable argon lines. The argon abundance can be estimated by using nitrogen data. However, this requires the N II $\lambda5680$ Å line, whose peculiarity was already noted above. Thus, we calculated the argon abundance by different methods: first, by
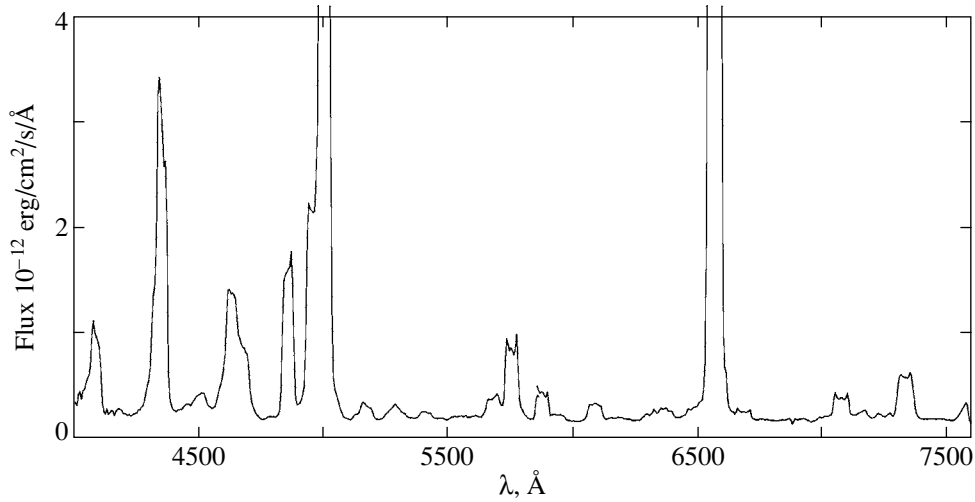
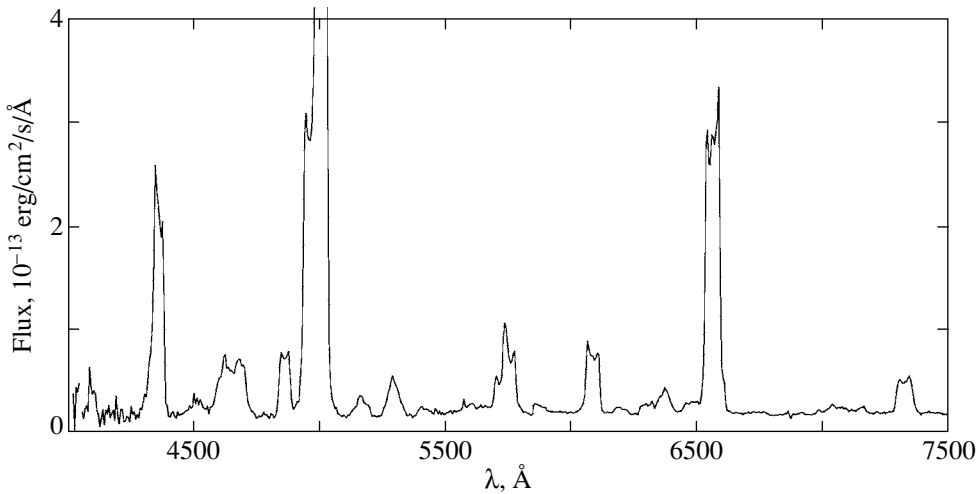**Fig. 11.** The 4000−7500 Å spectrum of V1494 Aql taken on May 8, 2000.

Fig. 12. The 4000−7500 Å spectrum of V1494 Aql taken on September 29, 2000.

adding up all the observable ionization stages

$$\frac{\text{Ar}}{\text{H}} = \frac{\text{Ar}^{2+}(\lambda7135)}{\text{H}^+(H\beta)}$$
$$+ \frac{\text{Ar}^{3+}(\lambda7236)}{\text{H}^+(H\beta)} + \frac{\text{Ar}^{4+}(\lambda7006)}{\text{H}^+(H\beta)};$$

and, second, by using the He/He^{++} ratio as the (Saizar *et al.* 1992)

$$\frac{\text{Ar}}{\text{H}} = \frac{\text{Ar}^{4+}(\lambda7006)}{\text{H}^+} \times \frac{\text{He}}{\text{He}^{++}(\lambda4686)}.$$

The first estimate was found to be an order of magnitude larger than the second estimate, with Ar^{3+} giving the largest contribution to the total argon abundance. Yet another line, most likely the C II doublet,

may contribute appreciably to the $\lambda7236$ Å intensity. For argon, we also retained two estimates: $\langle\text{Ar/H}\rangle = 9.4 \times 10^{-6}$, which was derived by the summation over the three ionization stages; and $\langle\text{Ar/H}\rangle = 1.12 \times 10^{-6}$, which was calculated by using the ionization correction. The results are presented in Table 14.

Iron

The iron abundance is commonly determined from the ratio (Andrea *et al.* 1994)

$$\frac{\text{Fe}}{\text{H}} = \left[\frac{\text{Fe}^{5+} + \text{Fe}^{6+}}{\text{H}^+(H\beta)}\right] \times \frac{\text{He}}{\text{He}^{++}}.$$

In our case, the [Fe VI] lines were weak and blended in the spectra of both novae. Therefore, we

Table 9. The line intensities relative to $H\beta$ uncorrected for interstellar reddening, R(O III), and the intensity ratio of [Fe VI] $\lambda5176$ Å and $\lambda5146$ Å for V1425 Aql

λ	May 28, 1995	May 29, 1995	July 26, 1995
$H\gamma$	0.31	0.46	0.39
$H\beta$	1.00	1.00	1.00
$H\alpha$	12.28	8.64	9.15
4363 [O III]	1.07	1.00	1.09
4640 N III	0.52	0.48	0.47
4686 He II	0.24	0.21	0.23
4959 [O III]	1.97	2.05	3.27
5007 [O III]	6.16	6.41	10.42
5309 [Ca V]	0.09	–	–
5680 N II	0.19	0.18	0.16
5755 [N II]	1.2	1.13	1.27
5876 He I	0.33	0.32	0.29
6087 [Fe VII]	0.17	0.17	0.28
6300 [O I]	0.73	0.64	0.35
6364 [O I]	0.47	0.42	0.24
6678 He I	0.18	0.15	0.11
7006 [Ar V]	0.07	0.05	0.06
7065 He I	0.34	0.31	0.24
7135 [Ar III]	0.34	0.28	0.33
7236 [Ar IV]	0.23	0.19	0.14
7320+7330 [O II]	1.31	1.21	1.25
R(O III)	4.36	4.89	7.15
$I(\lambda5176)/I(\lambda5146)$ [Fe VI]	1.9	–	2.3

estimated a lower limit on the iron abundance in both cases by taking into account only Fe^{6+} and by using the [Fe VII] $\lambda6087$ Å line. The calculated ratios were taken from Nussbaumer and Storey (1982)

$$\frac{N(Fe^{6+})}{N(H^+)} = \frac{\varepsilon(H\beta) \times N_e}{n(^1D) \times A(\lambda6087) \times h\nu} \times \frac{I(\lambda6087)}{I(H\beta)},$$

where $A(\lambda6087)$ is the emission probability in the $\lambda6087$ Å line, and $n(^1D) = \dfrac{N(Fe^{6+\,1}D_2)}{N(Fe^{6+})}$ is tabulated in the above paper.

The mean iron abundances were taken to be $\langle Fe/H \rangle = 2.5 \times 10^{-5}$ for V1425 Aql and $\langle Fe/H \rangle = 4.8 \times 10^{-5}$ for V1494 Aql. The results are presented in Table 15.

CONCLUSIONS

We have determined the chemical composition of the shells for three novae from their optical spectra. The spectra of standard stars were used to calibrate the nova spectra. In principle, this procedure is reliable, and it introduces minimum errors. However, since the CCD spectral sensitivity is low in the wavelength range $4000-4500$ Å, the intensities of the lines in this range are measured with a much lower accuracy than the line intensities in other wavelength ranges and using them increases the uncertainty of the result.

The question of plasma parameters is crucially important in an abundance analysis. The proper choice of the electron density and, particularly, temperature is of great importance in obtaining reliable estimates. The shell temperatures differ for different ions. In

Table 10. The line intensities for V1494 Aql uncorrected for interstellar reddening. The $H\beta$ intensity $=1.00$

λ	May 8, 2000	May 26, 2000	June 30, 2000	July 2, 2000	July 24, 2000	Sep. 3, 2000	Sep. 29, 2000	Oct. 25, 2000
4340 $H\gamma$+4363 [O III]	2.23	2.70	2.77	2.65	3.09	3.03	3.66	3.09
4515 N III	0.22	–	0.20	0.22	0.22	0.20	0.28	0.37
4640 N III	1.03	0.67	0.98	1.00	1.01	1.04	1.17	1.11
4686 He II	0.48	0.39	0.65	0.69	0.62	0.72	0.93	1.17
4959+5007 [O III]	5.66	8.89	9.75	8.99	10.98	21.17	17.57	18.31
5291 O VI	0.11	0.17	0.25	0.28	0.33	0.47	0.65	0.76
5411 He II	0.05	0.05	0.07	0.09	0.07	0.09	0.12	0.12
5678 N II	0.18	0.18	–	–	–	–	–	–
5721 [Fe VII]	–	–	–	–	0.28	0.47	0.67	0.66
5755 [N II]	0.60	2.11	0.89	0.84	1.05	1.30	1.10	0.72
5876 He I	0.20	0.22	0.17	0.17	0.15	0.12	0.08	0.07
5941 N II	0.03	0.03	0.03	0.03	0.02	–	–	–
6087 [Fe VII]	0.15	0.20	0.40	0.38	0.51	0.84	1.21	1.17
6195 O VI	0.04	–	0.04	0.04	0.06	0.08	0.10	0.13
6300 [O I]+6310 He II	–	0.22	–	0.06	–	0.16	0.16	
6374 [Fe X]	–	–	0.14	0.10	0.18	0.31	0.37	0.45
6480	–	–	–	–	–	0.15	0.19	0.28
6563 $H\alpha$	5.43	7.98	6.35	5.85	5.96	6.20	5.85	5.43
6678 He I	0.07	0.07	0.07	0.05	–	–	–	–
7065 He I	0.21	0.23	0.18	0.21	0.18	0.18	–	–
7320+7330 [O II]	0.39	1.17	0.50	0.53	0.61	1.06	0.75	0.50
R(O III)	2.12	2.65	2.82	2.73	2.81	5.51	3.71	4.68

Table 11. Helium abundances in the shells of V1425 Aql and V1494 Aql

Star	Date	He$^+$/H$^+$			He^{++}/H$^+$	He/H
		λ5876 Å	λ6678 Å	mean	λ4686 Å	
V1425 Aql	May 28, 1995	0.085	0.117	0.096	0.024	0.12
	May 29, 1995	0.080	0.107	0.089	0.021	0.11
	July 26, 1995	0.073	0.076	0.074	0.024	0.10
V1494 Aql	May 8, 2000	0.072	0.082	0.075	0.060	0.135
	May 26, 2000	0.078	0.056	0.071	0.048	0.119
	June 30, 2000	0.060	0.070	0.063	0.081	0.114
	July 2, 2000	0.060	0.051	0.057	0.086	0.143
	July 24, 2000	0.054	–	0.054	0.077	0.131
	Sept. 3, 2000	0.042	–	0.042	0.089	0.131
	Sept. 29, 2000	0.030	–	0.030	0.115	0.145
	Oct. 25, 2000	0.024	–	0.024	0.145	0.169

practice, however, the dependence of temperature on the ionization stage is disregarded. We did not introduce a temperature stratification in the nova shells either. For example, the temperatures in the He$^+$ and He^{++} zones were assumed to be equal, which appears to be untrue. The assumption of a uniform density is also a simplification of the actual mass distribution in the shells. Much of the shell mass may be concentrated in dense clumps, so the filling factor will be very small. This all is confirmed by

Table 12. Oxygen abundances in the shells of V1425 Aql and V1494 Aql

Star	Date	O^{++}/H^+, 10^{-3}	O^+/H^+, 10^{-4}	O^0/H^+, 10^{-4}	O/H, 10^{-3}	O/H(He), 10^{-2}
V1425 Aql	May 28, 1995	1.1	0.89	1.5	1.3	0.15
	May 29, 1995	1.2	0.83	1.4	1.4	0.16
	July 26, 1995	1.3	0.71	0.5	1.4	0.18
V1494 Aql	May 8, 2000	6.13	2.36	–	–	1.15
	May 26, 2000	9.62	7.07	–	–	1.73
	June 30, 2000	5.36	1.75	–	–	1.00
	July 2, 2000	4.95	1.85	–	–	1.29
	July 24, 2000	6.04	2.14	–	–	1.52
	Sept. 3, 2000	6.01	2.36	–	–	1.95
	Sept. 29, 2000	4.99	1.67	–	–	2.49
	Oct. 25, 2000	5.20	1.12	–	–	3.74

Table 13. Nitrogen abundances in the shells of V1425 Aql и V1494 Aql

Star	Date	N^+/H^+, 10^{-4}	N^{2+}/H^+, 10^{-2}	N^{3+}/H^+, 10^{-3}	N/H, 10^{-2}	N/H(He), 10^{-3}	N/H(O), 10^{-2}
V1425 Aql	May 28, 1995	2.1	1.8	8	2.6	23	0.38
	May 29, 1995	1.9	1.7	7.3	2.4	21	0.37
	July 26, 1995	2	1.5	7.1	2.2	20	0.51
V1494 Aql	May 8, 2000	4.58	–	–	–	0.824	2.22
	May 26, 2000	16.0	–	–	–	2.68	3.92
	June 30, 2000	4.43	–	–	–	0.802	2.54
	July 2, 2000	4.19	–	–	–	1.05	2.92
	July 24, 2000	5.22	–	–	–	1.27	3.70
	Sept. 3, 2000	4.80	–	–	–	1.50	3.96
	Sept. 29, 2000	4.04	–	–	–	1.95	6.03
	Oct. 25, 2000	2.63	–	–	–	1.85	8.78

Table 14. Argon abundances in the shell of V1425 Aql

Date (1995)	Ar^{2+}/H^+, 10^{-6}	Ar^{3+}/H^+, 10^{-6}	Ar^{4+}/H^+, 10^{-7}	Ar/H, 10^{-6}	Ar/H(He), 10^{-7}
May 28	1.2	10	2.9	11.5	14.5
May 29	0.95	8.6	1.9	9.7	10.0
July 26	0.86	5.8	2.2	6.9	9.0

the observed coexistence of high- and low-excitation lines. The emission line profiles (e.g., in V1494 Aql) occasionally show a complex structure with several components, which are probably related to many separate condensations.

Apart from the measurement errors in the intensities of the lines used to determine the ion abundances, the large uncertainty stems from the fact that many collisionally excited lines are very sensitive to the assumed temperature and density. In this sense, the helium abundance is determined most reliably, because the recombination lines used for our analysis are not very sensitive to the temperature and density. It should be noted that the He I λ7065 Å line with a

Table 15. Iron abundances in the shells of V1425 Aql and V1494 Aql

Star	Date	Fe^{6+}/H^+, 10^{-5}	Fe/H, 10^{-5}
V1425 Aql	May 28, 1995	0.52	2.6
	May 29, 1995	0.51	2.7
	July 26, 1995	0.57	2.3
V1494 Aql	May 8, 2000	1.46	3.28
	May 26, 2000	2.01	4.97
	June 30, 2000	2.01	2.82
	July 2, 2000	1.91	3.18
	July 24, 2000	2.55	4.34
	Sept. 3, 2000	4.08	6.00
	Sept. 29, 2000	5.85	7.37
	Oct. 25, 2000	5.67	6.61

Table 16. The chemical composition of several novae and the Sun

$\log N/H + 12$	Sun	V1425 Aql	V1494 Aql	V443 Sct
He	11.00	11.0	11.1	11.4
N	7.98	10.4 (9.6)	10.6 (9.2)	9.9
O	8.91	9.2	9.3	9.0
Ar	6.57	7.0 (6.0)	–	7.3
Fe	7.53	7.4	7.7	7.4

large contribution of the collision excitation was not involved in our abundance analysis.

The total elemental abundance in gaseous shells can be determined through the ion abundance. An uncertainty arises during the passage from the ion abundance to the elemental abundance. Depending on the physical conditions in the shell and on the observing conditions for the spectrum, not all of the existing ionization stages are usually considered because of a lack of suitable lines. The smaller the number of observed ionization stages, the larger the uncertainty in the elemental abundance. A comparison with theoretical calculations shows that the results obtained by using the ICF are correct, to within a factor of 2 (Andrea *et al.* 1994).

We have investigated three recent novae: V1425 Aql, V1493 Aql, and V1494 Aql. For all novae, we constructed the light curves and used them to determine the photometric parameters that characterize the brightness decline rate. For V1425 Aql, we identified lines, measured the interstellar reddening from the Balmer decrement, determined the plasma parameters, and obtained the abundances of several

chemical elements. For V1493 Aql, we identified lines, determined the expansion velocities, and estimated the interstellar reddening. For V1494 Aql, we identified lines and measured their intensities, measured the shell expansion velocities, and determined the interstellar reddening, plasma parameters, and chemical composition.

All observations were carried out with the same equipment. The observations of all novae were reduced by the same methods. Since the same theoretical data were used to determine the chemical composition, our observational data are homogeneous and can be compared with other data.

The thermonuclear theory of nova outbursts predicts an overabundance of CNO nuclei in the shells of fast novae. There is a correlation between the chemical composition and the class of nova decline rate. However, when this correlation is analyzed, a dependence on the white-dwarf mass and luminosity must also be taken into account.

We compared our results with data for the nova V443 Sct from Andrea *et al.* (1994). This nova has similar parameters that characterize the brightness decline rate: $t_2 = 19^d$ and $t_3 = 39^d$. Table 16 gives the chemical composition for V443 Sct, the two novae studied here, and the Sun. The solar data were taken from Aller (1984).

There are no O–Ne–Mg novae among the stars considered here. Nitrogen and oxygen are considerably enhanced in the two novae compared to the Sun, which is in agreement with the predictions of the thermonuclear theory for nova outbursts. The helium abundance is solar in V1425 Aql and exceeds its solar value only slightly in V1494 Aql. For comparison, the helium abundance in V443 Sct is twice as large, although V1494 Aql is classified by its decline rate as a very fast nova, while V443 Sct belongs to fast novae. The iron abundance exceeds its solar value in V1494 Aql and is lower than its solar value in V1425 Aql.

REFERENCES

1. L. H. Aller, *Physics of Thermal Gaseous Nebulae* (D. Reidel, Dordrecht, 1984).
2. J. Andrea, H. Drechsel, and S. Starrfield, Astron. Astrophys. **291**, 869 (1994).
3. R. E. S. Clegg, Mon. Not. R. Astron. Soc. **229**, 31P (1987).
4. M. M. De Robertis, R. J. Dufour, and R. W. Hunt, J. R. Astron. Soc. Can. **81**, 195 (1987).
5. IAU Circ., No. 6133 (1995); No. 6134 (1995); No. 6135 (1995); No. 6146 (1995); No. 6154 (1995); No. 6155 (1995); No. 6172 (1995); No. 6175 (1995); No. 6255 (1995); No. 7223 (1999); No. 7225 (1999); No. 7228 (1999); No. 7232 (1999); No. 7254 (1999); No. 7273 (1999); No. 7313 (1999); No. 7325 (1999);

No. 7326 (1999); No. 7327 (1999); No. 7328 (1999); No. 7330 (1999); No. 7337 (1999); No. 7381 (2000).

6. L. L. Kiss and J. R. Thomson, Astron. Astrophys. **335**, L9 (2000).

7. E. A. Kolotilov, A. M. Tatarnikov, V. I. Shenavrin, and B. F. Yudin, Pis'ma Astron. Zh. **22**, 813 (1996) [Astron. Lett. **22**, 729 (1996)].

8. C. G. Mason, R. D. Gehrz, C. E. Woodward, *et al.*, Astrophys. J. **470**, 577 (1996).

9. H. Nussbaumer and P. J. Storey, Astron. Astrophys. **70**, 37 (1978).

10. H. Nussbaumer and P. J. Storey, Astron. Astrophys. **113**, 21 (1982).

11. C. Payne-Gaposchkin, *The Galactic Novae* (North-Holland, Amsterdam, 1957).

12. P. Saizar, S. Starrfield, G. J. Ferland, *et al.*, Astrophys. J. **398**, 651 (1992).

13. M. A. J. Snijders, in *Proceedings of the 122nd IAU Colloquium on Physics of Classical Novae,* Ed. by A. Cassatella and R. Viotti (Springer-Verlag, New York, 1990), p. 188.

14. A. Tago, IAU Circ., No. 7223 (1999).

15. I. B. Voloshina, I. N. Glushneva, V. T. Doroshenko, *et al.*, *Spectrophotometry of Bright Stars,* Ed. by I. N. Glushnev (Nauka, Moscow, 1982).

Translated by V. Astakhov

Solar-Radius Variations from Transits of Mercury Across the Solar Disk

M. L. Sveshnikov[*]

Institute of Applied Astronomy, Russian Academy of Sciences, St. Petersburg, Russia
Received June 18, 2001

Abstract—We analyze the internal contact timings for transits of Mercury across the solar disk during 1631−1973. The revealed secular decrease in the solar radius, $0''06 \pm 0''03$, is attributed to systematic observational errors. We have found 80- and 11-year cycles in the solar-radius variations. The amplitudes of the 80- and 11-year cycles are $0''24 \pm 0''05$ and $0''08 \pm 0''02$, respectively. There is a positive correlation between the solar-radius and sunspot-number variations. This result is shown to be in conflict with the results of Laclare *et al.* (1996) for the sign of correlation. The possible error sources are discussed.
© 2002 MAIK "Nauka/Interperiodica".

Key words: *Mercury, Sun, Solar radius*

INTRODUCTION

Investigation of global oscillations of the figure of the Sun provides additional information on its internal structure. In the first half of the 20th century, the figure of the Sun was studied in relation to solar activity. With the detection of a deficit of the neutrino flux from the Sun during the Brookhaven ^{37}Cl experiment, with the development of gravitational theories alternative to the general theory of relativity, and with the progress made in helioseismology, astrometric studies of the Sun have intensified sharply. Of particular interest are the possible secular and long-period components in the oscillations of the solar radius and its variations with a period close to the 11-year solar cycle.

Various techniques for measuring the solar diameter are used to study the figure of the Sun: meridian, micrometric, heliometric, and astrolabe measurements; observations of the isophote distribution over the solar disk; and observations of solar eclipses and Mercury's transits across the solar disk. Each of the above techniques has characteristic systematic errors. Of the direct techniques, meridian measurements are least accurate, while astrolabe measurements are most accurate. For solar eclipses, one has to invoke the complex theory of lunar motion and to take into account the errors related to the lunar profile. The contact timings during transits of Mercury are easier to process, but the events themselves are much more rare.

A true boom in solar astrometry began in the 1970s. In particular, it resulted from the discovery

by Eddy and Boornazian (1979) of a decrease in solar radius $\dot{R}_\odot$ by $1''1$ per century based on Greenwich meridian measurements during 1836−1953. This study was immediately followed by several studies in which the authors obtained $|\dot{R}_\odot| < 0''1-0''2$ per century by analyzing solar eclipses and Mercury's transits (Parkinson *et al.* 1980; Shapiro 1980; Gilliland 1981; Krasinsky *et al.* 1985). In addition, having processed Mercury's transits, Shapiro and Gilliland found an 80-year variation of the solar radius with an amplitude of $\sim 0''2$. By analyzing 30 classical series of 1660−1985 measurements, Toulmonde (1997) showed that the deviation of $R_\odot$ from the mean $960''0 \pm 0''1$ on an interval of 300 years in the meridian observations is mainly attributable to an inadequate allowance for diffraction.

The results for the 11-year oscillations are more contradictory. Such variations were found to probably exist at a $0''1-0''3$ level, but there is disagreement as to the sign of the correlation between solar radius and Wolf number $W_\odot$. For example, Noel (1997) and Basu (1998) favor a positive correlation between $R_\odot$ and $W_\odot$, while Delache (1988) and Laclare *et al.* (1996) provide convincing evidence for a negative correlation based on 50000 astrolabe measurements during 1974−1995. In his review of the studies over the past 15 years, Rozelot (1998) concludes that the amplitude of the $R_\odot$ variations is $< 0''7$ and, probably, about $0''3$ (with a $0''1$ accuracy) in the last 5 years. There may also be solar oblateness, which varies with solar cycle. Moreover, the profile of the Sun (helioid) is not static but has a complex pulsating shape; i.e., the global geometry of the Sun depends on its irradiance. Rozelot provides an empirical relation between

[*]E-mail: `sml@quasar.ipa.nw.ru`

solar irradiance S [W m^{-2}] and Wolf number supplemented with the radius (with a positive correlation):

$$S = 539.14 + 0.0084W_{\odot} + 0.87R_{\odot}''. \quad (1)$$

The irradiance and $R_{\odot}$ correlate at a 0.8 level. Regarding the observations of Laclare's group, Rozelot points out the following: "the main conclusion is the remarkable likeness between the irradiance and diameter time series when a time lag of about half a solar cycle period is applied." It should be noted that all results for the 11-year variations are based only on direct solar-radius measurements, because, in the opinion of Gilliland (1981), transits of Mercury across the solar disk are unsuited to searches for 11-year solar-radius variations, as the mean separation between the data is about 9 years.

Here, we study the above components of the solar-radius variations based on an independent analysis of Mercury's transits across the solar disk on a 300-year interval.

OBSERVATIONS OF MERCURY'S TRANSITS

An archive of more than 4500 contact-timing observations for Mercury's transits across the solar disk from 1631 until 1973 has been created at the Institute of Applied Astronomy (Russian Academy of Sciences). This archive is most complete not only in the number of observations but also in auxiliary information on them, because it contains data on the observing sites, observers, instruments, and observing techniques and conditions. The observations were taken from original publications and, if the latter were inaccessible, from other known compilations (Sveshnikov 1999). The reduction of the observations included correction for instrumental errors and reduction of the initial times to the UT time scale and geocenter. About 2700 internal-contact observations were involved in the final data reduction. External-contact observations were used to estimate the quality of the inner-contact observations by various authors and to assign weights. As the reference ephemerides in calculating $(O-C)$ for the contact timings, we used DE200, DE403, and DE405. These ephemerides are essentially based on radar observations of inner planets and accurately describe the relative positions of the Sun, Mercury, and the Earth. The calculations were performed with a universal programming system (ERA) to solve the problems of ephemeris and dynamical astronomy (Vasilyev and Krasinsky 1997).

The conditional equations for the contact timings are

$$\sin(Q - i)(V + \dot{V}T) + \sin(Q + i)(W + \dot{W}T) \quad (2)$$

$$\pm \cos(Q \mp i)(N + \dot{N}T) + \left(\frac{1}{r} - \frac{1}{r_{\odot}}\right)\Delta R_{\odot}$$

$$+ 0.911\frac{\rho}{r}\dot{D}T^2k = \frac{\rho}{r}(\Delta\sigma + \dot{D}\Delta T^{\text{s}}).$$

The right-hand parts contain the ephemeris angular distance $\Delta\sigma$ between the solar and Mercury's limbs at the observed contact time. It can be calculated from $(O-C)$ for the times Δt corrected for the difference between the ephemeris and universal time scales, ΔT^{s}. Here, $\dot{D}$ is the apparent approach velocity of the solar and Mercury's centers (in [arcsec s^{-1}], ρ is the geocentric distance of Mercury, and r, $r_{\odot}$ are the heliocentric distances of Mercury and the Earth (in AU), respectively.

The Newcomb parameters V, W, N and their secular variations $\dot{V}$, $\dot{W}$, $\dot{N}$ are linear combinations of the corrections to the Keplerian orbital elements of Mercury and the Earth. T is given in centuries from 1900.0, and Q and i are auxiliary angles. The term $\Delta R_{\odot}$ contains a constant correction $\Delta R_{\odot}^{\text{o}}$ to the initial ephemeris solar radius 959.''63, the secular radius variation $\dot{R}_{\odot}$, and the terms that describe the solar-radius oscillations with periods of 80 and 11 years:

$$\Delta R_{\odot} = \Delta R_{\odot}^{\text{o}} + \dot{R}_{\odot}T + \sin(2\pi\varphi_1)\Delta R_{80}^{\text{s}} \quad (3)$$

$$+ \cos(2\pi\varphi_1)\Delta R_{80}^{\text{c}} + \frac{W_{\odot,m}}{100}[\sin(2\pi\varphi)\Delta R_{11}^{s}$$

$$+ \cos(2\pi\varphi)\Delta R_{11}^{\text{c}}].$$

For the 80-year terms, $\varphi_1 = (t - 1919.0)/80$. The terms for the 11-year cycle have a more complex structure. It indicates that the solar-cycle duration changes from 8 to 15 years; therefore, the cycle phase is calculated from the dates of the preceding (t_m^1) and succeeding (t_m^2) solar minima closest to the epoch of observation: $\varphi = (t - t_m^1)/(t_m^2 - t_m^1)$. Since, in addition, the solar activity $(W_{\odot})$ changes from cycle to cycle, we chose a simple model of proportionality between the amplitudes of the solar-radius and Wolf-number variations at maximum for a given cycle $W_{\odot,m}$ with a normalization to the mean $W_{\odot,m} = 100$ for the entire interval under study. Such a form of the terms for the 11-year cycle allowed us to reduce $\Delta R_{\odot}$ at the epoch of observation to a uniform system of cycle phases with the standard Wolf number at maximum and, thus, increases the probability of detecting the possible effect of solar-radius variations.

In principle, a correction to the adopted lunar tidal deceleration can be included in the equations. However, since it can be reliably and with a much higher accuracy determined from laser observations of the Moon, k need not be included in the equations (it was introduced in some variants for checking purposes). The coefficient 0.911 results from the transformation of residuals at the Moon's observed longitude due to decelartion of the Earth's rotation into corrections for the reduction to a uniform time scale.

Table 1. Influence of the observing technique and the system of weights (in $0.''01$)

Unknown	Var Ia 1677−1973	Var Ib 1720−1940	Var Ic 1677−1973	Var I 1677−1973	Var II 1677−1973	Var III 1677−1973
	all observations		without screen			
	$p_{obs}/15^s\dot{D}$		$p_{obs}/15^s\dot{D}$		1	p_{obs}
$\Delta R_\odot^o$	$+8 \pm 2$	$+17 \pm 2$	$+12 \pm 2$	$+16 \pm 2$	$+15 \pm 2$	$+15 \pm 2$
$\dot{R}_\odot$	-16 ± 3	$+4 \pm 4$	-6 ± 3	-6 ± 3	-8 ± 4	-8 ± 4
ΔR_{11}^s	$+13 \pm 2$	$+14 \pm 2$	$+15 \pm 2$	$+8 \pm 2$	$+10 \pm 2$	$+9 \pm 2$
ΔR_{11}^c	-6 ± 2	$+0 \pm 2$	-6 ± 2	$+2 \pm 2$	$+2 \pm 2$	$+1 \pm 2$
ΔR_{80}^s	$-$	$-$	$-$	-18 ± 3	-15 ± 3	-14 ± 2
ΔR_{80}^c	$-$	$-$	$-$	$+16 \pm 3$	$+17 \pm 3$	$+17 \pm 2$
σ_o	1.188	1.194	1.192	1.127	1.452	1.342

RESULTS OF THE DATA REDUCTION

Table 1 lists solutions for the unknowns related to the solar-radius variations for various sets of observations and systems of weights. We see that a change of the observing interval significantly affects the determination of $\Delta R_\odot^o$ and $\dot{R}_\odot$ (Var Ia and Var Ib). Weights were assigned to the observations according to the scheme $P = p_{obs}/15^s\dot{D}$, where p_{obs} is the relative weight of a given observation (from 0 to 1) in the set of observations of a given contact for a given transit.

The appearance of an appreciable secular decrease in the solar radius (Var Ia) is attributable to a sharp deviation of the correction $\Delta R_\odot$ for the observations after 1940. This is because a large number of amateur observations with a screen appeared in the second half of the 20th century. In these observations, the internal contact timings are systematically shifted to the midtime of the event, thereby effectively reducing the apparent solar radius. When the screen observations are excluded on the entire interval (Var Ic), the value of $\dot{R}_\odot$ decreases by more than a factor of 2. We also see that the solution depends weakly on the choice of a weight system (Var I, Var II, Var III; Var II corresponds to an equal-weight solution). The radius-variation parameters are determined quite reliably. As the final solution, we chose Var I.

Our determinations of the 80-year solar-radius variations agree with the data of Shapiro (1980) and Gilliland (1981), both in amplitude and in phase.

Figure 1 compares the detected 11-year variations in solar radius ΔR_{11} and in yearly mean Wolf numbers $W_\odot$. Interestingly, the solar-radius and Wolf-number variations are close in phase. Their slight discrepancy can be explained by a difference between the curve shapes: the curve is virtually a sine wave

for $\Delta R_\odot$ and asymmetric with a phase shift of the maximum, depending on its magnitude, for $W_\odot$. In general, the correlation between the curves is 0.7. Figure 2 compares the determinations of the 11-year variations from transit observations before 1973 (Var I) with direct solar-radius measurements after 1974. It shows monthly mean Wolf numbers, the 11-year radius variations according to Var I (*1*), and the radius variations derived from astrolabe measurements in the Southern Alps (*2*) with an amplitude of $\sim 0.''1$ and in antiphase with the Wolf numbers (Laclare *et al.* 1996). Also shown in the figure are the means of several series of meridian and astrolabe measurements as inferred from the data in Laclare *et al.* (1996), Noel (1997), and Toulmonde (1997). Their average (*3*) roughly agrees in phase with the Wolf-number variations and has an amplitude of $\sim 0.''1 - 0.''2$. Noteworthy are the Santiago astrolabe solar-radius measurements by Noel (1997), which coincide in phase with the $W_\odot$ variations but differ sharply from the remaining observations both in absolute value of the radius and in variation amplitude.

Let us now consider the possible causes of the appearance of an 11-year cycle in $\Delta R_\odot$ when processing Mercury's transits.

(1) The influence of instrumental errors on the 300-year interval gives rise to a secular component, as was shown for direct solar-radius measurements by Toulmonde (1997) and by using a screen for transit observations. Clearly, these errors can also appear in long-period variations. Therefore, the detected secular effect, $\dot{R} \simeq 0.''1$ per century, should be considered to be fictitious from a physical point of view. However, the emergence of an 11-year cycle due to such effects is unlikely.

(2) The main transit repetition period is 46 years: the duration of 46 revolution periods of the Earth
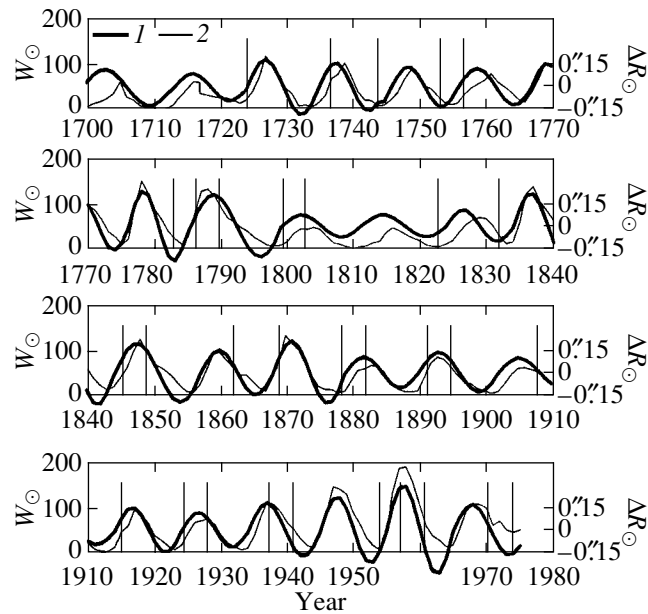
Fig. 1. A comparison of the 11-year variations in solar radius ΔR_{11} (*1*) and in yearly mean Wolf numbers $W_\odot$ (*2*). The vertical bars indicate the data that correspond to the observed transits of Mercury.
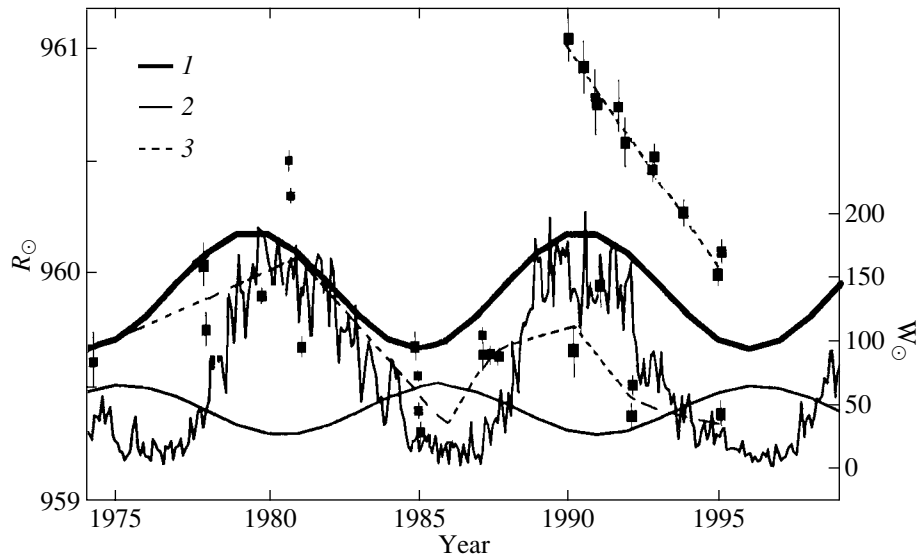

Fig. 2. The solar radius as measured from the 1974−1998 observations (see the text).

relative to Mercury's nodes is 191 draconic periods of Mercury. The ratios of Mercury's draconic and synodic periods produce additional periods of 7, 13, and 33 years in the transit phenomenon. In addition, May transits are often separated from November transits by an interval of 3 years. In these cases, Mercury's tracks are systematically displaced over the solar disk (Fig. 3). Track displacements from the equatorial region to polar regions of the Sun in the case of its noticeable oblateness could give a periodic radius variation. However, helioseismic measurements of solar equipotential surfaces and the processing of radar ranging observations for planets yielded a dynamical oblateness of $\sim 10^{-7}$, which apparently gives a difference between the equatorial and polar radii within a few hundredths of an arcsecond. This is also confirmed by direct measurements of the apparent solar oblateness at Pik du Midi (Rozelot 1998). On the other hand, track displacements change the geometric observing conditions for transits and, thus,

Table 2. Influence of various factors on the formation of an 11-year term in the from $\Delta R = A\sin(2\pi\varphi) + B\cos(2\pi\varphi) = C\sin(2\pi\varphi + \varphi_0)$

N	Variant	A''	B''	C''	φ_0, deg
		Solar radius			
1	Laclare *et al.* (1996)	$+0.04$	$+0.10$	$-$	$-$
1a		$-$	$-$	$+0.11$	$+135°$
		Transits			
2	All (Var I)	$+0.08 \pm 0.02$	$+0.02 \pm 0.02$	$+0.08 \pm 0.02$	$+11° \pm 12°$
3	Equatorial	$+0.08 \pm 0.03$	$+0.04 \pm 0.02$	$+0.09 \pm 0.02$	$+30° \pm 15°$
4	High-latitude	$+0.05 \pm 0.03$	-0.09 ± 0.04	$+0.10 \pm 0.04$	$-60° \pm 20°$
		Planetary radii			
5	All techniques	$+0.04 \pm 0.03$	$+0.00 \pm 0.03$	$+0.04 \pm 0.03$	$0° \pm 25°$
6	Heliometer + double-image technique	$+0.04 \pm 0.03$	$+0.03 \pm 0.03$	$+0.05 \pm 0.03$	$+30° \pm 20°$

Note. In row $N1$, the expression for $\Delta R_\odot$ was derived for $\varphi = (t - 1985.15)/P$, $P = 10.4$. Row $N1a$ presents Laclare's result recalculated to the common (for all the remaining rows) epoch of phase measurement, $t_0 = 1987.1$.

indirectly affect the determination of the effective solar radius.

To determine the influence of track displacements, we divided the transits into equatorial ones, for which the minimum separation between the centers did not exceed 820″, and high-latitude ones. The results are presented in Table 2. We see that the oscillation amplitudes are equal and that the positive correlation between solar radius and Wolf number is preserved for both variants, being 0.6 and 0.8 for the equatorial and high-latitude transits, respectively.

(3) The explanation of the $\Delta R_\odot$ variations as resulting from variations in the Earth's atmospheric turbulence, whose properties depend on the phase of solar activity, is very popular. Indeed, the concept of solar radius is ambiguous and in many respects depends on observing conditions. This is probably one of the main reasons why the results disagree, particularly for meridian measurements. In particular, the peculiarity of local astroclimatic conditions could explain the disagreement between the results obtained by different authors. From this viewpoint, the contact-timing observations are more objective, because the optical phenomenon of disk contact is observed, which may be considered as an analog of double-image micrometer measurements. In this case, however, caution must also be exercised when simultaneously analyzing observations with widely separated epochs. A comparison of observations at adjacent transits is highly reliable. The atmospheric effect can be completely checked only by the methods of space astrometry, but a rough check can be performed by directly measuring the diameters of large planets. If this effect is present, the planetary-radius measurements must also contain an 11-year oscillation. To this end, we used determinations of

the equatorial and polar radii for Mars and Jupiter and Saturn's equatorial radius on the interval 1820–1950 by various methods (Dollfus 1970; Kozlovskaya 1963). We determined the amplitudes and phases of the possible 11-year harmonic in the measurements of planetary radii R in the same form as we did when studying the solar-radius variations from transits. The results in Table 2 show that the 11-year cycle in $R_\odot$ can be explained by the atmospheric effect. Nevertheless, this effect is indistinct in the planetary-radius measurements. Therefore, the atmospheric influence on our result for the solar-radius variations cannot be considered to have been proven.

(4) Finally, the apparent solar-radius oscillations can be directly attributed to some average photospheric surface, but in this case, the interpretation can also be ambiguous. Clearly, during (visual or CCD) observations, an isophote of some surface brightness is recorded. The detected 11-year variations can be a reflection of the actual solar-radius
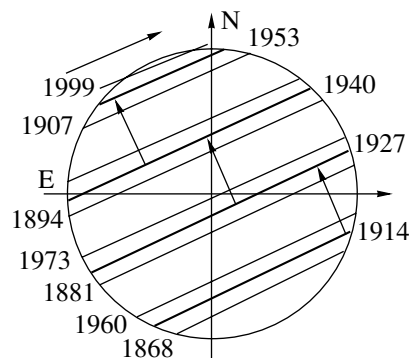

Fig. 3. Displacement of the Mercury's tracks across the solar disk with a 13-year period.

oscillations or a change in the isophote distribution because of temperature variations in a ~100-km-thick surface layer of the photosphere during the solar cycle (Tripathy and Antia 1999).

CONCLUSIONS

Based on a dynamical analysis of the observations of internal contact timings for Mercury's transits across the solar disk on a time interval spanning more than 25 solar cycles (see Table 1, Var I), we

(1) have found a correction of $0.''16 \pm 0.''02$ to the ephemeris solar radius, which is consistent both with the estimate by Toulmonde (1997) on the 300-year interval obtained from direct astrometric observations and with most currently available solar-radius measurements;

(2) have shown that the secular decrease in solar radius $\dot{R}_\odot$ does not exceed $0.''06 \pm 0.''03$ and is caused by systematic observational errors;

(3) have found an 80-year component in the $R_\odot$ variations; our determinations of its amplitude $(0.''24 \pm 0.''05)$ and phase agree with the data of Shapiro (1980) and Gilliland (1981);

(4) have determined the 11-year component in the apparent $R_\odot$ variations with an amplitude of $0.''08 \pm 0.''02$; the oscillations are close in phase to the solar cycle; this result is consistent with the results of other authors, except for the result obtained by Laclare *et al.* (1996) (the amplitude estimates agree, while the phase estimates significantly differ);

(5) have shown that transit observations do not provide a reliable physical interpretation of the 11-year solar-radius oscillations.

REFERENCES

1. D. Basu, Sol. Phys. **183**, 291 (1998).
2. Ph. Delache, Adv. Space Res. **8**, 119 (1988).
3. *Surface and Interface of Planets and Satellites,* Ed. by A. Dollfus (Academic, London, 1970; Mir, Moscow, 1974).
4. J. A. Eddy and A. A. Boornazian, Bull. Am. Astron. Soc. **11**, 437 (1979).
5. R. L. Gilliland, Astrophys. J. **248**, 1144 (1981).
6. S. V. Kozlovskaya, Bull. ITA Akad. Nauk SSSR **9**, 330 (1963).
7. G. A. Krasinsky, E. Yu. Saramonova, M. L. Sveshnikov, *et al.*, Astron. Astrophys. **145**, 90 (1985).
8. F. Laclare, S. Delmas, J. Koin, *et al.*, Sol. Phys. **166**, 211 (1996).
9. F. Noel, Astron. Astrophys. **325**, 825 (1997).
10. J. H. Parkinson, L. V. Morrison, and F. R. Stephenson, Nature **288**, 548 (1980).
11. F. P. Pijpers, Mon. Not. R. Astron. Soc. **297**, L76 (1998).
12. J. P. Rozelot, Sol. Phys. **177**, 321 (1998).
13. I. I. Shapiro, Science **208**, 51 (1980).
14. M. L. Sveshnikov, Tr. IPA RAN **4**, 69 (1999).
15. M. Toulmonde, Astron. Astrophys. **325**, 1174 (1997).
16. S. C. Tripathy and H. M. Antia, Sol. Phys. **186**, 1 (1999).
17. M. V. Vasilyev and G. A. Krasinsky, Tr. IPA RAN **2**, 228 (1997).

Translated by V. Astakhov

Spatial Variations in Parameters of Quasi-Hourly Sunspot Fragment Oscillations and a Singular Penumbra Oscillator

E. Yu. Nagovitsyna and Yu. A. Nagovitsyn[*]

Pulkovo Astronomical Observatory, Russian Academy of Sciences,
Pulkovskoe sh. 65, St. Petersburg, 196140 Russia
Received June 18, 2001

Abstract—We obtained three-dimensional interpolated portraits for the radial and torsional oscillations of fragments of 12 sunspots in the form of deviations of their polar coordinates from drift as functions of the time and distance from the sunspot center. We performed a wavelet analysis of the two orthogonal components and determined the dominant oscillation modes; the period varies between 40 and 100 min for different sunspots. We revealed two types of dominant modes, one is associated with the sunspot and the other is associated with its surrounding pores: the central-mode frequency depends on the maximum field strength of the sunspot and decreases from its center toward the boundary, while the peripheral-mode frequency depends on the heliographic latitude and decreases toward the sunspot boundary from the far periphery. We revealed radial variations in frequency and amplitude with a spatial period of 0.8 sunspot radius. The types of dominant modes and the radial variations in oscillation parameters are linked with the subphotospheric structure of an active region—with two types of spiral waves and concentric magnetic-field waves. We estimated the mean pore oscillation energy to be $\sim 10^{30}$ erg and found a singular oscillator with a mean energy of $\sim 10^{31}$ erg in the penumbra at a distance of 0.8 sunspot radius. We argue that the singular penumbra oscillator is the source of solar flares. © *2002 MAIK "Nauka/Interperiodica".*

Key words: *Sun*

INTRODUCTION

The quasi-hourly oscillations of atmospheric and photospheric objects on the Sun have aroused considerable interest since the 1960s. The need for multi-hour observations with a high spatial−temporal resolution and the complexity of the process itself, which in nonstationary and nonlinear, hinder rapid progress in this field. The relationship of these oscillations to the magnetic field is currently clear, and the main range of period variations, from several tens to several hundreds of minutes, has been determined. Quasi-hourly oscillations were found in a number of phenomena: in oscillations of sunspot matter (Gopasyuk 1985), in sunspot area oscillations (Demchenko *et al.* 1985), in latitudinal−longitudinal sunspot oscillations (Ikhsanov and Nagovitsyna 1990), in sunspot structure oscillations (Nagovitsyna 1990), in oscillations of sunspot magnetic field strengths (Nagovitsyn and Vyal'shin 1990, 1992), in prominence oscillations (Mashnicz and Bashkirtsev 1999), in intensity oscillations of radio sources (Gelfreikh *et al.* 2000), and in many others. Here, we continue to study the oscillations by analyzing the coordinate perturbations of sunspot fragments (flux tube bundles). Magnetic fragments are seen in the photosphere as pores and dark features of sunspots $\sim 10^{8}$ cm in size with lifetimes from several hours to several days. Our approach is unique in that it allows us to investigate the unobservable subphotospheric layers where most of the solar-activity phenomena generally originate.

We use the same observational data as in our previous study of periodicities by a harmonic analysis (Nagovitsyna and Nagovitsyn 1998a). Unfortunately, a harmonic analysis of the nonstationary and nonlinear processes yields incorrect results, for example, it underestimates the amplitude at high frequencies. Therefore, we directly estimated the oscillation amplitude and orientation on the solar surface, which allowed us to model the horizontal field configuration of bipolar sunspot groups (Nagovitsyna and Nagovitsyn 2001). We investigate the oscillation amplitude−frequency characteristics by a wavelet analysis. Such an analysis is most suitable in our case and has led us to more definitive conclusions regarding the observational data under consideration.

OBSERVATIONS AND DATA REDUCTION

A 340-min-long series of photoheliograms at 15-min intervals was obtained on June 24, 1989

Basic parameters of the sunspots under study

Number, polarity	B	L	S, m.s.h.	R, 10^9 cm	N	H, 10^2 G	H^*, 10^2 G	$\overline{\nu}_{\mathrm{c}}$, 10^{-4} Hz	$\overline{\nu}_{\mathrm{p}}$, 10^{-4} Hz	max A_{c}, 10^8 cm
5542-N	$-19°9$	$9°9$	292	1.68	9	24.5	30.2	3.919 ± 0.390	2.477 ± 0.188	1.85
5549-N	-16.2	337.6	106	1.01	5	22.5	22.8	2.500 ± 0.195	$-$	2.52
5552-N	-17.7	315.0	210	1.43	13	23	28.2	3.725 ± 0.616	3.077 ± 0.332	2.61
5552-S	-20.0	307.2	159	1.24	11	23	26.1	3.656 ± 0.292	3.324 ± 0.358	1.91
5555-N	26.5	296.6	299	1.70	15	24.5	30.3	3.772 ± 0.192	4.104 ± 0.278	0.50
5555-S	25.3	306.2	697	2.60	16	29.5	33.8	4.206 ± 0.261	3.496 ± 0.418	0.84
5556-N	-18.9	299.6	231	1.49	11	24.5	28.8	3.584 ± 0.056	2.386 ± 0.151	2.84
5558-S	8.4	282.7	200	1.39	8	25	27.8	4.162 ± 0.293	1.911 ± 0.114	1.62
5559-S	19.6	280.3	157	1.23	6	21	26.0	2.718 ± 0.253	$-$	2.06
5561-N	-19.2	292.7	186	1.34	7	25	27.3	3.094 ± 0.440	$-$	3.80
5561-S	-19.9	284.2	226	1.48	7	21	28.6	3.272 ± 0.334	2.520 ± 0.698	1.71
5563-N	-15.6	274.7	189	1.35	6	21.5	27.4	3.149 ± 0.479	$-$	2.04

(6:30–12:10 UT), with a special Pulkovo Observatory photoheliograph. Figure 1 shows the arrangement of sunspot groups on the visible solar surface during the observations. The sunspots marked by circles have a sufficient number of fragments to derive the radial dependences. The sample contains 114 fragments of 12 sunspots. The first seven columns in the table list their basic parameters: the sunspot group number and polarity, the latitude (B) and longitude (L) of the sunspot center, the sunspot area in millionths of the solar hemispheres (m.s.h.) (S), the sunspot radius (R), the number of fragments used (N), and the maximum sunspot field strength (H).
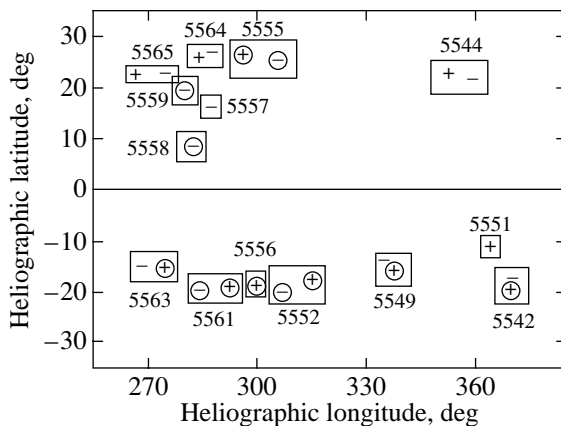

Fig. 1. The arrangement of sunspot groups during the observations. The circles mark the sunspots under study ("+" and "−" denote N- and S-polarity sunspots, respectively).

First, we determined the B and L coordinates of the sunspot centers and fragments with an accuracy of no less than $0.05° \approx 6 \times 10^7$ cm by the GELIKOP technique (Nagovitsyn and Nagovitsyna 1996). Next, the fragment coordinates were transformed to polar coordinates (r, φ) relative to the sunspot centers. The linear fragment drifts in r and φ were calculated by least squares; these drifts were previously studied in more detail (Nagovitsyna and Nagovitsyn 1998b, 1999). Subsequently, we subtracted the drifts from the time dependences of coordinates $r(t)$ and $\varphi(t)$ and obtained sequences of coordinate residuals $\Delta r(t)$ and $\Delta a(t)$ (Δa is the azimuthal component transformed from degrees to a linear measure). The radial residual is $\Delta r > 0$ when moving away from the sunspot center and $\Delta r < 0$ when moving toward the sunspot center; the azimuthal residual is $\Delta a > 0$ when moving counterclockwise around the sunspot center and $\Delta a < 0$ when moving clockwise.

Having the time dependences of coordinate residuals for fragments at various distances from the sunspot center and using a two-dimensional filtering with a cosinusoidal filter in the time × distance plane with the simultaneous interpolation of the residuals to equidistant 9 min × $0.1R$ nodes (R is the sunspot radius; see the table), we obtained three-dimensional portraits for the radial and torsional fragment oscillations of all sunspots. These portraits are shown in Fig. 2 for eight sunspots surrounded by pores, so that their oscillation "rugs" extend to $\rho \approx 3$ (ρ is the distance from the sunspot center normalized to R); the fragments of the remaining sunspots are localized inside, i.e., their $\rho \leq 1$. To simplify the picture, we used only two colors, white
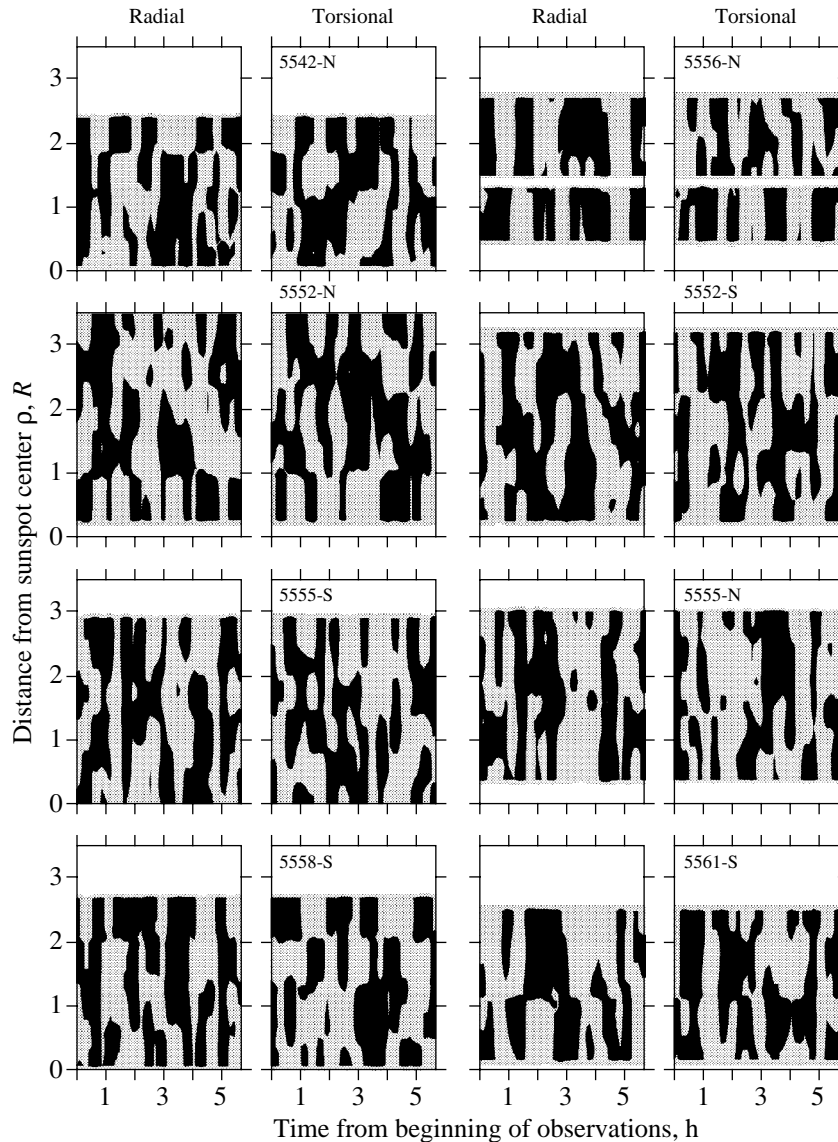
Fig. 2. Three-dimensional interpolated portraits of magnetic-fragment oscillations.

and black, which denote the positive and negative residuals, respectively (see above). In our view, Fig. 2 faithfully conveys the impression gained when considering the observational data: on the one hand, the oscillations are clearly not rigid (e.g., the pattern changes appreciably near the sunspot boundaries); on the other hand, we can trace individual synchronous perturbations of the entire region. These portraits are used below to study the amplitude−frequency parameters of magnetic-fragment oscillations by a wavelet analysis.

A wavelet analysis is a modern method of studying quasi-periodicities (peculiarities, signal-shape fractality, etc.). It is based on a decomposition of the observed function into the basis formed by orthogonal (or quasi-orthogonal) extensions and shifts of

a reference burst, a parent wavelet (Grosmann and Morlet 1984). In the context of our problem, we are primarily interested in constructing the amplitude−frequency dependences of the oscillations. Previously, we carried out this procedure using a real MHAT wavelet and Hilbert transformation (Gnedin *et al.* 1999). Here, we use a complex Morlet wavelet.

DOMINANT OSCILLATION MODES

A harmonic analysis reveals a number of peaks in the oscillation power spectrum (Nagovitsyna and Nagovitsyn 1998a). A wavelet analysis also reveals several peaks that are close in frequency to overtones, but in most cases, the dominant oscillation mode can be unambiguously determined. We do this
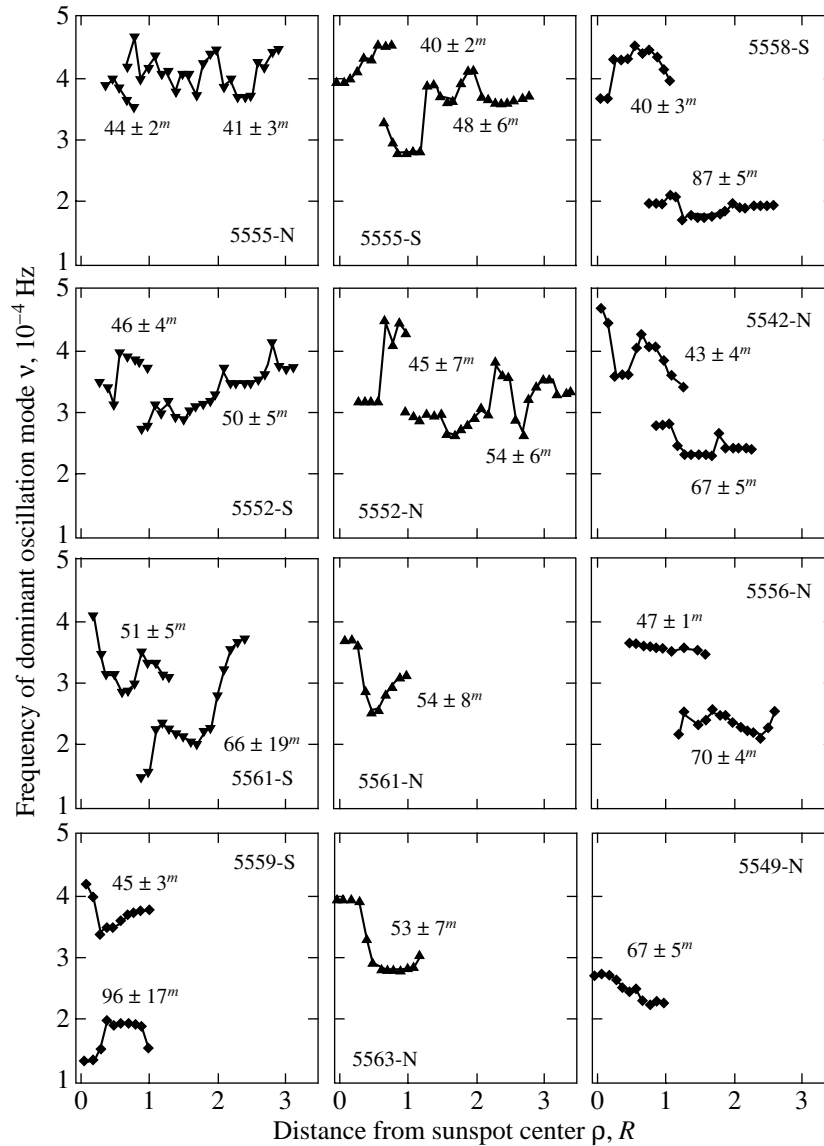
Fig. 3. The frequencies of dominant magnetic-fragment oscillation modes.

as follows. Since the oscillations were decomposed into orthogonal spatial components, radial and azimuthal, the amplitude–frequency parameters at the output are represented by two spectra, $A_r(\nu_r)$ and $A_a(\nu_a)$. We compare these spectra and identify individual peaks in them (in our case, their number generally does not exceed three). For each peak, we take the maximum amplitudes and the corresponding frequencies and determine the total horizontal amplitude and weighted mean frequency

$$A = \sqrt{A_r^2 + A_a^2}, \quad \nu = (\nu_r A_r + \nu_a A_a)/(A_r + A_a).$$

From the peaks under consideration, we choose one with the largest amplitude A, the dominant oscillation mode [see Nagovitsyna and Nagovitsyn (2001) for the oscillation orientation on the solar surface].

The interpolated oscillation portraits (Fig. 2) allow this procedure to be carried out at $0.1R$ steps.

Figure 3 shows the derived dominant mode frequency $\nu(\rho)$ for all 12 sunspots. The first column in Fig. 3 (except the bottom panel) shows the trailing sunspots of bipolar groups, the second column shows their leading sunspots, and the third column (and the bottom panel in the first column) shows the leading sunspots of unipolar groups, in which no trailing sunspots are observed. The main result of Fig. 3 is that all sunspots with pores exhibit a discontinuity in the radial dependence of frequency $\nu(\rho)$ near the sunspot boundary $\rho = 1$. We called the dominant oscillation mode associated with the sunspot *central* (below denoted by the subscript "c")

and the dominant mode associated with pores *peripheral* (subscript "p"). Columns 9 and 10 give the mean frequencies

$$\overline{\nu}_{\mathrm{c}} = \frac{1}{n} \sum_{i=1}^{n} \nu_{\mathrm{c}}(\rho_i), \quad \overline{\nu}_{\mathrm{p}} = \frac{1}{n} \sum_{i=1}^{n} \nu_{\mathrm{p}}(\rho_i)$$

and dispersions (unbiased standards) of the central and peripheral modes (for sunspot 5559-S, we took a mean of the two modes with close A). The oscillation periods are marked in Fig. 3, and they lie in the range 40−100 min; the mean oscillation frequencies of the central and peripheral modes correspond to periods of 48 and 57 min.

Clearly, the frequency $\nu(\rho)$ for unipolar groups (the third column in Fig. 3) varies more regularly than that for the bipolar groups: according to the table, the frequency dispersions for unipolar and bipolar groups are, on the average, 0.205 and 0.392, respectively. The dispersion probably reflects the oscillation stationarity attributable to the spatial−temporal stability of the active-region structure. It is well known that unipolar groups are evolutionally older and result from a simplification and stabilization of the magnetic configuration in which the trailing sunspot gradually disappears.

The central and peripheral oscillation modes differ not only by their spatial localization and frequency. Consider yet another physical difference. The observed maximum sunspot field strength H (see the table) is the mean for June 23 and 25, because there were no observations on June 24 (Sunday).[1] In Fig. 4a, the mean central-mode frequency $\overline{\nu}_{\mathrm{c}}$ is plotted against the observed strength H. Despite the modest correlation (68%), there is a clear tendency for proportionality. Column 8 in the table gives the maximum strength H^* calculated from an empirical formula of Hautgust and van Sloiters

$$H^* = 37S/(S + 66), \qquad (1)$$

where S is the sunspot area in m.s.h. (see the table). In Fig. 4b, $\overline{\nu}_{\mathrm{c}}$ is plotted against the calculated strength H^*. We see that using H^* increases the correlation (78%). One of the reasons is the center−edge effect, as a result of which the empirical formula $H^*(S)$ holds strictly, i.e., $H = H^*$, only at the center of the solar disk and H systematically decreases toward the edge (Bray and Loughhead 1964). The sunspots under study lie in the range from 0.35 (5549-N) to 0.8 (5563-N) radius of the visible disk and have a deficit of strength $\Delta H = H^* - H$, which actually increases toward the edge (correlation ∼60%). Thus, the frequency of the central oscillation mode is directly proportional to the maximum sunspot

---

[1] The Pulkovo sunspot magnetic field database is accessible at http://www.gao.spb.ru/database/mfbase.
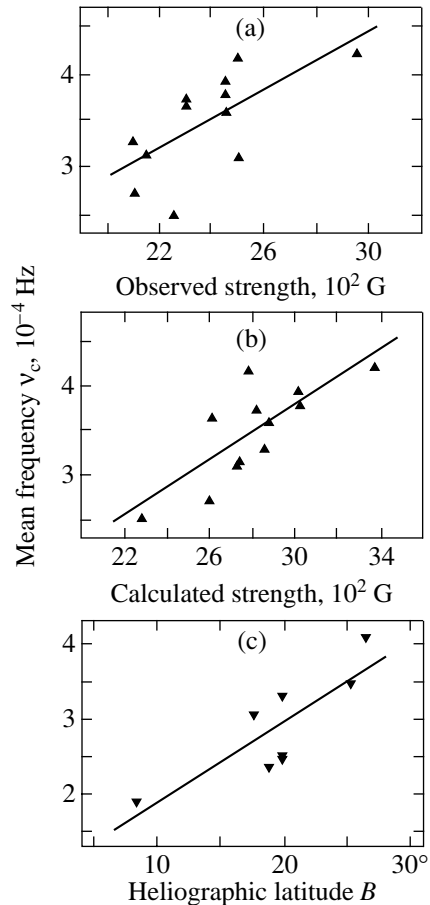
Fig. 4. Correlations of the central-mode frequency with maximum sunspot field strength (a, b) and of the peripheral-mode frequency with heliographic latitude (c).

field strength. The situation with the peripheral mode is different; its frequency $\overline{\nu}_{\mathrm{p}}$, as Fig. 4c shows, is proportional to heliographic latitude B (see the table).

At first glance, the existence of two types of dominant oscillation modes seems strange. It would be more reasonable to expect the dominant-mode frequency to decrease proportionally to the field strength with increasing distance from the sunspot center, reaching a more or less constant minimum value outside the sunspot. However, it is pertinent to recall that, while studying the spatial distribution of magnetic fragments in an active region, we found them to concentrate in two types of horizontal spiral waves, one (four-arm) encloses the sunspot and the other (two-arm) encloses the surrounding pores. In addition, in the velocity field, the central and peripheral structures are associated with the cell and the surrounding roller of supergranulation convection [see Nagovitsyna and Nagovitsyn (1998b, 1999) and the final section in this paper for more details]. In light of this, the difference between the dominant oscillation
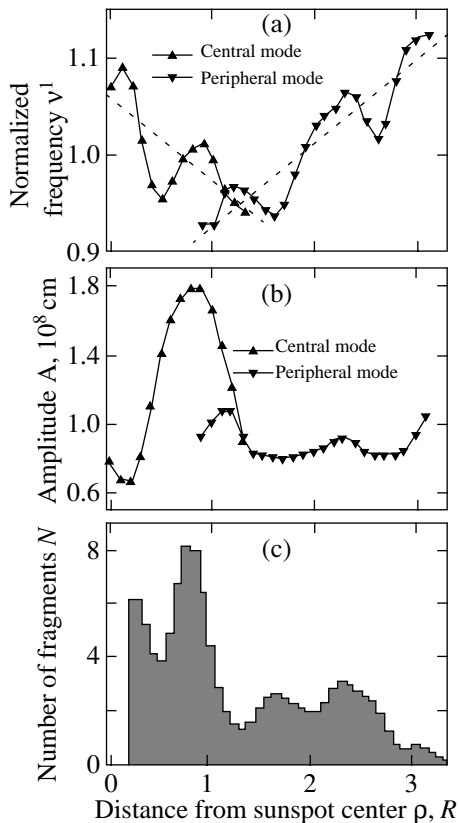
Fig. 5. Radial variations in the oscillation frequency (a) and amplitude (b) and in the number of magnetic fragments (c).

modes for magnetic fragments that belong to different structures is quite natural.

RADIAL VARIATIONS OF OSCILLATION PARAMETERS

The derived dependences $\nu(\rho)$ (Fig. 3) have different domains of definition and variations for different sunspots. Therefore, to calculate the radial dependence of frequency averaged over all sunspots, we must first normalize the frequencies $\nu_c^{(j)}(\rho)$ and $\nu_p^{(j)}(\rho)$ to their means $\overline{\nu_p^{(j)}}$ and $\overline{\nu_p^{(j)}}$ (see the table) for each jth sunspot:

$$\nu_c^1(\rho) = \frac{1}{n(\rho)} \sum_{j=1}^{n(\rho)} \frac{\nu_c^{(j)}(\rho)}{\overline{\nu_c^{(j)}}},$$

$$\nu_p^1(\rho) = \frac{1}{n(\rho)} \sum_{j=1}^{n(\rho)} \frac{\nu_p^{(j)}(\rho)}{\overline{\nu_p^{(j)}}}.$$

Figure 5a shows the normalized frequency $\nu^1(\rho)$ averaged over all sunspots and smoothed over three points (the mean dispersion is 0.09). We can see

that the central-mode frequency decreases from the sunspot center ($\rho = 0$) toward a bright ring ($\rho = 1.35$), while the peripheral-mode frequency decreases from the far periphery ($\rho > 3$) toward the penumbra ($\rho = 0.9$): in the linear approximation (the dashed lines in Fig. 5a),

$$\nu_c^1(\rho) = 1.058 - 0.088\rho, \quad \nu_p^1(\rho) = 0.841 + 0.086\rho;$$

i.e., the rates of change in the central- and peripheral-mode frequencies are equal. The opposite sign of the radial frequency gradient is yet another physical difference between the central and peripheral modes. The harmonic spatial oscillations of $\nu^1(\rho)$ are its principal characteristic feature in Fig. 5a: the oscillation frequency of magnetic fragments $\nu^1(\rho)$ reaches local maxima at $\rho = 0, 0.8$ (central mode), 1.3, 2.3, and 3.1 (peripheral mode). Thus, the frequency $\nu^1(\rho)$ outlines a system of concentric rings separated by a distance of $\sim 0.8R \approx 1.2 \times 10^9$ cm around the sunspot center.

Figure 5b shows the total horizontal oscillation amplitude $A(\rho)$ of the central and peripheral modes averaged over all sunspots and smoothed over three points (the mean dispersion is 4×10^7 cm). The principal feature of the function $A_c(\rho)$ is an intense peak in the penumbra at $\rho = 0.8$, where the oscillation amplitude is enhanced several-fold, reaching, for example, 3.8×10^8 cm in sunspot 5561-N, which corresponds to a maximum instantaneous velocity of 7×10^5 cm s^{-1} for an oscillation period of 54 min (the maximum A_c is given in the last column of the table). This result matches our direct estimates through the dispersions of coordinate residuals Δr, Δa (Nagovitsyna and Nagovitsyn 2001). In addition, Fig. 5b clearly shows small enhancements of $A_p(\rho)$ at $\rho = 1.1, 2.3, 3.1$. A comparison of Figs. 5a and 5b indicates that the spatial frequency and amplitude variations with a $0.8R$ period are synchronous. Together with the absence of a $A_p(\rho)$ peak at $\rho = 0.8$, this proves that the absolute maximum of the central-mode amplitude at $\rho = 0.8$ is not an artifact attributable to the horizontal penumbra field direction.

In view of our conclusion about the radial frequency and amplitude variations with a $0.8R$ period, we recall our result on the system of concentric rings of magnetic fragments (Nagovitsyna and Nagovitsyn 1998b, 1999). This result is reproduced in a simplified form in Fig. 5c, which shows a histogram of the radial fragment distribution $N(\rho)$ smoothed over three points; this histogram exhibits peaks at similar distances $\rho \approx 0.2, 0.8, 1.5, 2.3, 3.1$. Thus, the concentric rings of enhanced magnetic-fragment density separated by a distance of $\sim 0.8R$ reflect the actual concentric magnetic-field waves, which modulate the physical parameters of the quasi-hourly oscillations.
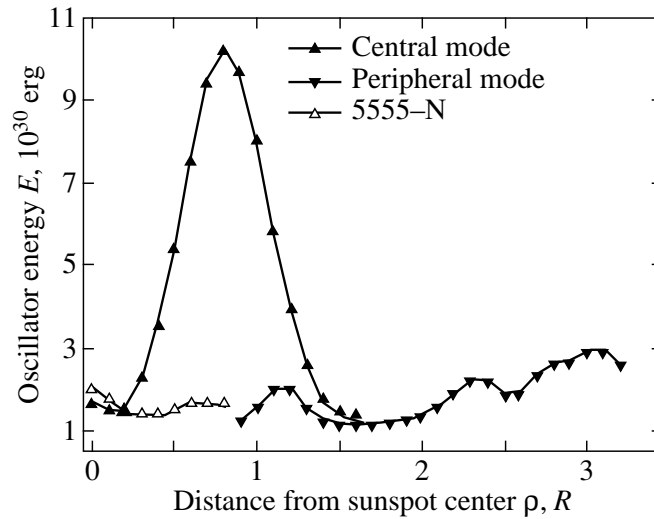
Fig. 6. Radial variations in the energy of spatial magnetic-fragment oscillations.
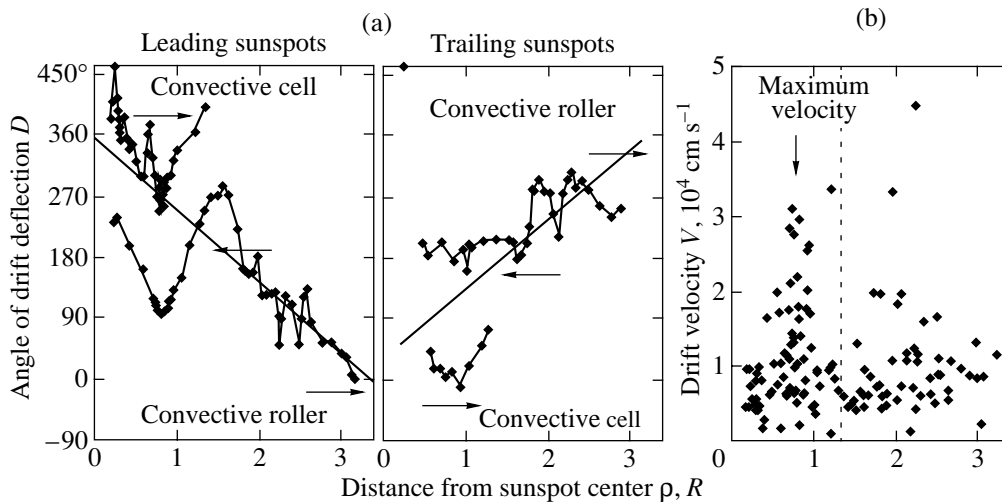

Fig. 7. Radial variations in the drift parameters of magnetic fragments: (a) the angle of drift deflection from the radial direction ($D = 0°, 180°, 90°$, and $270°$ if the fragment moves away from the sunspot center; toward the center; counterclockwise around the center, and clockwise, respectively); (b) the magnitude of the drift velocity. The vertical dashed line marks a bright ring, and the horizontal dotted lines separate the outflowing and inflowing magnetic fluxes.

SINGULAR PENUMBRA OSCILLATOR

Let us consider the radial variations in the oscillation energy of a magnetic fragment by estimating it as the energy of an oscillator of mass m in the harmonic approximation:

$$E(\rho) = m\omega^2(\rho)A^2(\rho)/2 = 2\pi^2 m\nu^2(\rho)A^2(\rho).$$

For each fragment, we have the product of the squares of the frequency and amplitude $\nu^2(\rho)A^2(\rho)$ (its mean is 10^9 cm^2 s^{-2} in order of magnitude), and we must estimate only the factor $2\pi^2 m$. The dynamical sunspot depth estimated by Solov'ev (1984) and Nagovitsyn (1997) does not exceed $(2-3) \times 10^8$ cm.

Let us make use of the total solar mass above depth z determined in the model of the convection zone by Spruit (1974): $M_z = 5.593 \times 10^{25}$ g for $z = 2.127 \times 10^8$ cm. Since the area of a fragment of typical size is $S \approx 4$ m.s.h. $= 2 \times 10^{-6} S_{\mathrm{Sun}}$, the fragment mass is $m = (S/S_{\mathrm{Sun}})M_z = 1.1 \times 10^{20}$ g. Thus, the sought-for factor is $2\pi^2 m = 2.2 \times 10^{21}$ g, and the oscillator energy is $10^9 \times 10^{21}$ cm^2 s^{-2} g $= 10^{30}$ erg in order of magnitude. Figure 6 shows the energy $E(\rho)$ of the central and peripheral fragment oscillation modes averaged over all sunspots and smoothed over three points: the mean oscillation energy is $E \sim 10^{30}$ erg

outside the penumbra and increases to $\sim 10^{31}$ erg inside the penumbra at $\rho = 0.8$. We (arbitrarily) called the quasi-hourly fragment oscillations in the $\rho \approx 0.8$ zone *a singular penumbra oscillator*.

Why does the singular oscillator emerge? It is probably generated by some peculiar feature of the subphotospheric motion of matter in the penumbra, and we can roughly show precisely which feature. In Fig. 7, the drift of magnetic fragments, which we subtracted here to study the oscillations, is represented in terms of the angle of deflection from the radial direction D (smoothed over three points) and the magnitude of velocity V. The fragment drift direction (Fig. 7a) corresponds to the system with a cell at its center and a roller of supergranulation convection on its periphery. The opposite signs of the gradients $\partial D/\partial \rho$ in the leading and trailing sunspots of bipolar groups (the straight lines in Fig. 7a), which is attributable to the opposite winding of spiral waves, are of no importance (Nagovitsyna and Nagovitsyn 1998b, 1999). The only thing that matters is that there are both outflow and inflow running parallel to each other ($\Delta D \approx 80°$) in the region bounded by the bright ring ($\rho \leq 1.35$). At $\rho = 0.8$, the relative velocity of these flows reaches a maximum (Fig. 7b) and, in the leading sunspots, their motion also transforms into rotation ($D = 270°, 90°$). Consequently, the interaction between the outflow and inflow and, accordingly, the resistance to the fragment motion reach a maximum at $\rho = 0.8$, which probably enhances the quasi-hourly fragment oscillations (the central mode in the outflow and in the inflow). Such low frequencies are characteristic of the internal gravity oscillations, in which buoyancy is the main restoring force.

In the 12 sunspots under study, the singular-oscillator energy changes from 6×10^{29} erg (5555-N) to 3×10^{31} erg (5561-N); i.e., it falls within the energy range of solar flares (from $\sim 10^{29}$ erg in subflares to 3×10^{32} erg in the largest events), spanning the energies of flares of importance 1–3. Recall that flares in white light are generally localized near and inside the sunspot penumbrae, their continuum energy is $\sim 10^{30}$ erg, and their mean duration is ~ 10 min. The most important thing is the observation of a series of homological flares with durations from several hours to several days and the recurrence of flares with an hourly period (Zirin 1966). These data correspond to the characteristics of the singular penumbra oscillator we found. In addition, such a source of flare energy is attractive in that it does not require any change in magnetic energy but uses the energy of matter motion beneath the photosphere. We do not discuss the possibility of energy transfer from the spatial oscillations of fragments to the tops of the associated loop systems (through long-period magnetic waves). The

reason is that observations of prominence oscillations with similar periods (Mashnich and Bashkirtsev 1999) suggest that this transfer does take place to one degree or another. The mechanism is actually at work, and it is probably responsible to some extent for the characteristic amplitude–frequency nonstationarity of the quasi-hourly oscillations because of their permanent damping. At the end of our observations (at 12:01 UT), a weak subflare (SF) occurred in the flare-active group 5555; during the observations, this group stood out by the lowest oscillation energy of fragments in the sunspot penumbra (Fig. 6).

CONCLUSIONS

A wavelet analysis has allowed us to make much greater progress in understanding the magnetic-fragment oscillations than has a harmonic analysis. This once again confirms the high efficiency of a local (in time and frequency) analysis when studying nonlinear and nonstationary processes. Our main results are the following:

(i) two types of dominant quasi-hourly oscillation modes associated with sunspots and pores were detected;

(ii) radial (concentric) variations in the oscillation parameters with a spatial radius of 0.8 sunspot radius were detected; and

(iii) a singular penumbra oscillator and the estimation of its mean energy, $\sim 10^{31}$ erg, and the mean pore oscillation energy, $\sim 10^{30}$ erg were detected.

These results are in good agreement with our data obtained from the spatial distribution and drift of magnetic fragments. In general, our study has shown that the view of a sunspot as a single flux tube, through split into separate bundles, is too simplified. Helioseismic data suggest that the depth of supergranulation convection is not $\sim 10^9$ cm, as assumed previously, but $\sim 10^8$ cm (Duvall *et al.* 1999). According to our results, the assumed sunspot depth must be reduced to the same value. The three-dimensional loop system of an active region in the corona is probably transformed beneath the photosphere into a two-dimensional spiral system at a depth of 2–2.5 thousand km. As our study shows, the sunspot field does not suppress the motion of matter beneath the photosphere; on the contrary, it provides its fragments with record energies of motion in the penumbra. Since supergranulation convection produces a drift of magnetic fragments inside the sunspot, the possibility of transporting such a "loose" field from the bottom of the convection zone through denser matter is called into question. Our study indicates that spatial oscillations are an attribute of the magnetic fields of active regions in the photosphere

and that the previously detected coherent field structures in the form of spiral and concentric waves point to a self-organization of the two-dimensional oscillating system. This view on the nature of sunspots seems more promising.

REFERENCES

1. R. J. Bray and R. E. Loughhead, *Sunspots* (Chapman and Hall, London, 1964; Mir, Moscow, 1967).
2. B. I. Demchenko, G. S. Minasyants, N. G. Makarenko, and S. O. Obashev, Astron. Tsirk. **1360**, 3 (1985).
3. T. L. Duvall, A. G. Kosovichev, P. H. Scherrer, *et al.*, Sol. Phys. **170**, 63 (1997).
4. G. B. Gelfreikh, Yu. A. Nagovitsyn, and K. Shibasaki, in *Proceedings of the JENAM-2000* (GEOS, Moscow, 2000), p. 119.
5. Yu. N. Gnedin, Yu. A. Nagovitsyn, and T. M. Natsvlishvili, Astron. Zh. **76**, 532 (1999) [Astron. Rep. **43**, 462 (1999)].
6. S. I. Gopasyuk, Izv. Krym. Astrofiz. Obs. **73**, 9 (1985).
7. A. Grosmann and J. Morlet, SIAM J. Math. Anal. **15**, 723 (1984).
8. R. N. Ikhsanov and E. Yu. Nagovitsyna, Soln. Dannye **4**, 77 (1990).
9. G. P. Mashnich and V. S. Bashkirtsev, Sol. Phys. **185**, 35 (1999).
10. Yu. A. Nagovitsyn, Pis'ma Astron. Zh. **23**, 859 (1997) [Astron. Lett. **23**, 742 (1997)].
11. Yu. A. Nagovitsyn and E. Yu. Nagovitsyna, Kinematika Fiz. Nebesnykh Tel **12**, 55 (1996).
12. Yu. A. Nagovitsyn and G. F. Vyal'shin, Soln. Dannye **9**, 91 (1990).
13. Yu. A. Nagovitsyn and G. F. Vyalshin, Astron. Tsirk., No. 1553 (1992).
14. E. Yu. Nagovitsyna, Soln. Dannye **5**, 79 (1990).
15. E. Yu. Nagovitsyna and Yu. A. Nagovitsyn, in *Proceedings of the Conference on New Cycle of Solar Activity: Observational and Theoretical Aspects* (GAO RAN, St. Petersburg, 1998a), p. 129.
16. E. Yu. Nagovitsyna and Yu. A. Nagovitsyn, Pis'ma Astron. Zh. **24**, 554 (1998b) [Astron. Lett. **24**, 475 (1998b)].
17. E. Yu. Nagovitsyna and Yu. A. Nagovitsyn, Sol. Phys. **186**, 193 (1999).
18. E. Yu. Nagovitsyna and Yu. A. Nagovitsyn, Pis'ma Astron. Zh. **27**, 144 (2001) [Astron. Lett. **27**, 118 (2001)].
19. A. A. Solov'ev, Soln. Dannye **1**, 73 (1984).
20. H. A. Spruit, Sol. Phys. **34**, 277 (1974).
21. H. Zirin, *The Solar Atmosphere* (Blaisdell, Waltham, 1966; Mir, Moscow, 1969).

Translated by V. Astakhov

Sodium Emission from Comet Shoemaker–Levy 9 in the Magnetosphere of Jupiter

V. V. Prokof'eva[*], V. P. Tarashchuk, and Yu. T. Tsap

Crimean Astrophysical Observatory, p/o Nauchnyi, Crimea, 334413 Ukraine
Received July 3, 2001

Abstract—On July 20, 1994, before the Q fragments of Comet Shoemaker–Levy 9 fell to Jupiter, more than 200 spectra of the Jovian features were obtained at the Crimean Astrophysical Observatory in the wavelength range 5700–7600 Å with a 26 s exposure time and a spectral resolution of 20 Å. We found a time-varying Na D line emission in the form of two components with Doppler shifts of about 30 Å. The brightest and most frequent sodium flares were detected when the Q fragments passed through the Jovian inner magnetosphere at a distance of about three the Jovian radii ($3R_J$) from its center, where they crossed the Io–Jupiter current tube. A frequency analysis of our data revealed a flare recurrence time scale of 1 min. We conclude that sodium was released from the cometary dust and from the surfaces of numerous cometary debris and that its amount was enough to produce the observed emission. The observed high-speed clouds of sodium atoms are assumed to have been formed through ionization, ion acceleration by the bidirectional electric fields of Alfvén waves in the Io–Jupiter current tube, and their neutralization. © 2002 MAIK "Nauka/Interperiodica".

Key words: *Comet Shoemaker–Levy 9, Jupiter, sodium*

INTRODUCTION

The fall of Comet Shoemaker–Levy 9 (SL 9) to Jupiter was predicted immediately after its discovery on March 24, 1993, by Carolyn and Eugene Shoemaker and David Levy. The comet consisted of 21 fragments with magnitudes from 19^m to 22^m (Sekanina 1995a, 1995b). They fell to Jupiter from July 16 until July 22, 1994, at a latitude of $\sim 45°$ in its southern hemisphere. The explosion times in the Jovian atmosphere were predicted with an accuracy of several minutes. The duration of the observations at each observatory was limited by the Jovian visibility conditions; it sank below the horizon 1 h after the beginning of an astronomical night. Many observatories worldwide took part in the observations of these unique events.

The spectroscopic observations at the Crimean Astrophysical Observatory (CrAO) aimed at accumulating observational data to investigate the fast processes. The large number of observations obtained on July 20 revealed a completely new phenomenon, the appearance and variability of Na D line emission. Based on preliminary intensity estimates for the sodium emission, Prokof'eva and Tarashchuk (1996a, 1996b) and Prokof'eva *et al.* (1997) noted several peculiarities of this phenomenon. The main

peculiarities include the following: the highest flaring activity was observed for 1 h and ended 40 min before the Q fragments fell to Jupiter, the emission was detected virtually over the entire disk of Jupiter, and the Doppler shift of the D-line emission corresponded to velocities higher than 1000 km s^{-1}. These authors also assumed that the sodium emission took place in the Jovian inner magnetosphere when the Q fragments surrounded by the cometary coma were passing through it. Recall that the complex of cometary fragments called PQ was brightest and most active from the outset (Sekanina 1995a). The Q fragment with the most extended coma was apparently the brightest of all fragments. Its parts Q1 and Q2 diverged in a direction perpendicular to the comet trajectory long before they approached Jupiter, and their subsequent fragmentation took place (Weaver *et al.* 1995). Thus, for example, seven pieces were detected on January 14–25, 1994 (Sekanina 1995b). An analysis of the observations of the light echo from Io and hot clouds on the Jovian limb showed that at least eight explosions occurred on July 20, 1994, when the Q1 and Q2 fragments fell in the planetary atmosphere (Prokof'eva *et al.* 1996).

West (1995) noted the great importance of the works aimed at investigating the various peculiar events observed before the cometary fragments fell to Jupiter. He believes that this may give a key to

---

[*]E-mail: `prok@crao.crimea.ua`

understanding the processes that take place during collisions of small bodies with planets in the Solar system.

These problems are discussed here. We describe our observational data, present the results of their reduction, and analyze the temporal characteristics of the sodium emission. The unusual nature of the recorded event prompted us to consider the following: (1) the properties of the inner cometary coma as a possible source of sodium; (2) the correspondence between the observed emission energy and the amount of sodium in the Q fragments; and (3) the possibility of constructing a qualitative model for the formation of high-speed clouds of sodium atoms during the interaction of the cometary material with the Jovian magnetosphere based on standard physical mechanisms.

OBSERVATIONAL DATA

Observing and Spectrum-Reduction Techniques

The Jovian disk areas were observed at the CrAO using specially assembled spectral instrumentation based on a digital TV system of the MTM-500 telescope, which provided a high time resolution (Abramenko et al. 1996). The spectral range covered was 5700–7600 Å with a spectral resolution of 20 Å. The exposure time of a single spectrum was 26 s. A peculiarity of the observations was the possibility of continuously checking the location of the spectrograph entrance aperture on the Jovian disk. It was sequentially pointed at the disk areas along the $-45°$ parallel where the cometary fragments fell, at the disk center and the region of the central meridian at a latitude of $+45°$, at the western and eastern limbs near the equator, and at the northern polar region. On July 19 and 20, we took 53 and 207 spectra with circular entrance apertures 9 and 6 arcsec in diameter, respectively; on July 20, the Jovian observations began on a light sky, which allowed the duration of the spectral monitoring to be increased to 4 h (UT 17 h 04 min—21 h 10 min). The digital data collection in a computer was carried out in series and started by the operator's command. The time interval between exposures was <1 s, which provided a time resolution that was almost equal to the exposure time. The breaks between series were determined by the spectrograph aperture repointing at various regions of the Jovian disk.

The observations by other authors that revealed the Na D line emission were obtained during and after the explosions of the Q fragments. The results of a preliminary analysis of the sodium emission detected on July 20, 1994, were compared with the data of other observers (Rose-Serot et al. 1995; Fitzsimmons et al. 1995; Catalano et al. 1995) by
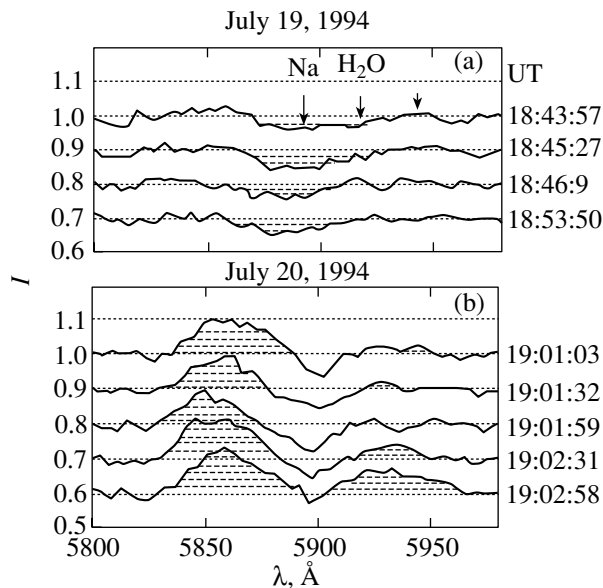

Fig. 1. Reduction of the spectral portions with the sodium line: (a) in absorption on July 19 and (b) in emission on July 20. The times of observations are indicated on the right. Panel (a) shows the positions of the sodium line and water vapor absorption bands (5915, 5918, and 5942 Å), which were probably blended with the sodium emission.

Prokof'eva and Tarashchuk (1996b). This comparison showed good agreement between the occurrence times of the sodium emission in the Jovian atmosphere.

The sodium 5890–5896 Å doublet was near the transmission cutoff of the OS-14 filter used in the grating spectrograph to limit the spectral range. When reducing the spectra, the transformation to wavelengths was made by using the neon spectra taken during our observations. To refine the zero point of the wavelength scale, we used laboratory measurements of the transmission curve for the OS-14 filter. According to these measurements, the 25% filter transmission level corresponds to a wavelength of 5810 Å. The accuracy of the adjusted wavelength scale was ~3 Å. The spectra were reduced with the program written by S. Sergeev from the CrAO. Two portions of the continuum with the boundaries 5790–5830 Å and 5955–5985 Å were separated on both sides of the sodium line. We drew a second- or third-degree polynomial to which the spectral portion under study was normalized over these portions. The data reduction is illustrated in Fig. 1: the upper and lower panels for July 19 and 20, respectively. The portions corresponding to the sodium emission are hatched. Also indicated are the positions of two water absorption bands.

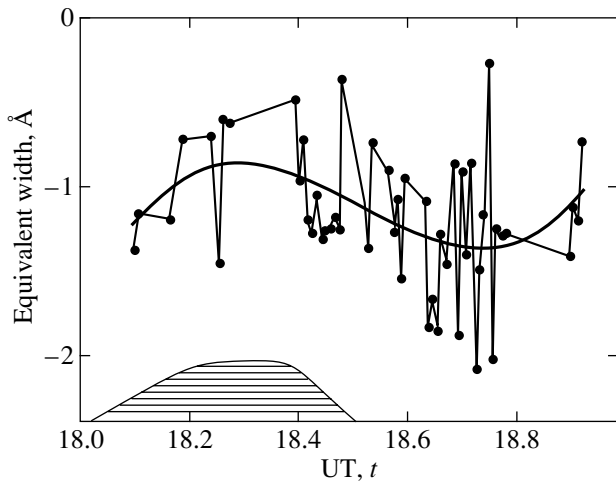The validity of the identification of the observed

Fig. 2. Time dependence of the equivalent width of the sodium doublet observed in the July 19, 1994 spectrum of Jupiter in absorption. The hatching indicates the position of the dusk sodium flare in the Earth's atmosphere.

Fig. 3. Time dependences of the equivalent width of the short-wavelength sodium emission component observed in the July 20, 1994 spectrum of Jupiter. The hatching indicates the period during which the fall of the debris of the Q fragment to Jupiter was recorded (Prokof'eva *et al.* 1996).

emission with the resonance Na D line is beyond question for the following reasons:

(1) In the wavelength range 5850–5940 Å, where the emission under study is located, the solar spectrum commonly exhibits the He I 5876 Å triplet. No traces of this triplet were found in our July 19 spectrum. Helium is known to be contained in the Jovian atmosphere, and small increases in the intensity of the resonance He I 584 Å line in the ultraviolet were detected in the upper atmosphere after the fall of large cometary fragments (Gladstone *et al.* 1995). However, the emission under discussion occurred when the fragments were still far from the Jovian upper atmosphere. In addition, if the observed variability were produced by helium, then the single He I 6678 Å would also be variable. Yet, the emission in this spectral range was virtually constant.

(2) The July 20 spectra also exhibit intensity variability near the sodium 6160.7–6154.2 Å multiplet (5). Since this multiplet lies at the edge of the the variable (in intensity) methane 6190 Å absorption band, it is difficult to measure. At the same time, it was firmly established that an increase in intensity with strengthening Na D line emission and, conversely, a decrease in intensity with weakening Na D line emission was observed in this range.

(3) The detected sodium emission cannot belong to the sodium cloud located near Io (the radius of its orbit is $5.95R_J$), because it was behind Jupiter during our observations. The emission from the sodium cloud near Io is known to exhibit no large Doppler shifts. Moreover, the spectroscopic observations of the Io torus from space in July 1994 revealed no
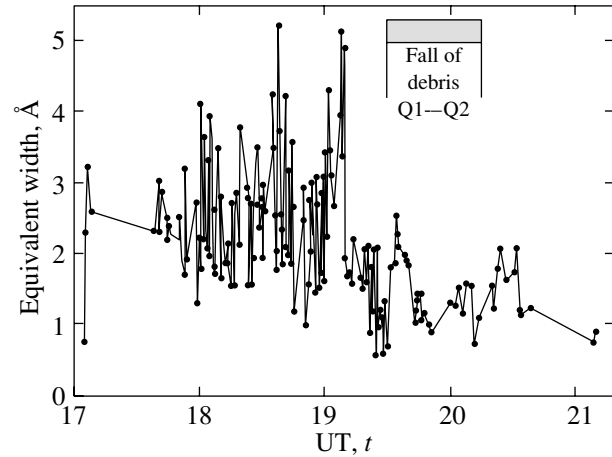
variations in the sodium emission related to the comet fall (McGrath *et al.* 1995).

(4) The observed emission cannot be produced by a dusk sodium flare in the Earth's atmosphere, because the D line of the flare shows no Doppler shift and because its duration is short.

Additional evidence for the identification of the emission with the Na D line is that sodium is widespread, is present in the cometary material, and has a low ionization potential. Thus, the above evidence argues for the identification of the observed emission with the Na D line emission.

Equivalent Widths of the Sodium Emission

We measured the equivalent widths of the Na D doublet in all the spectra of the Jovian disk features taken on July 19 and 20. Note that on July 19, the sodium line was seen only in absorption. This allowed us to estimate the accuracy of measuring its equivalent widths from low-dispersion spectra. The mean equivalent width was 1.2 Å. This value essentially matches the equivalent width of the sodium doublet observed in the solar spectrum (1.3 Å), suggesting that there were no systematic errors in the spectrum reduction. The curve in Fig. 2 indicates a slow variation in the sodium-doublet equivalent width with time on July 19. We estimated the rms deviation of a single measurement to be 0.3 Å by assuming that the scatter of points was attributable to the measurement errors alone. We also estimated the influence of the atmospheric dusk sodium flare on the results of our measurements. On the dates of observations,
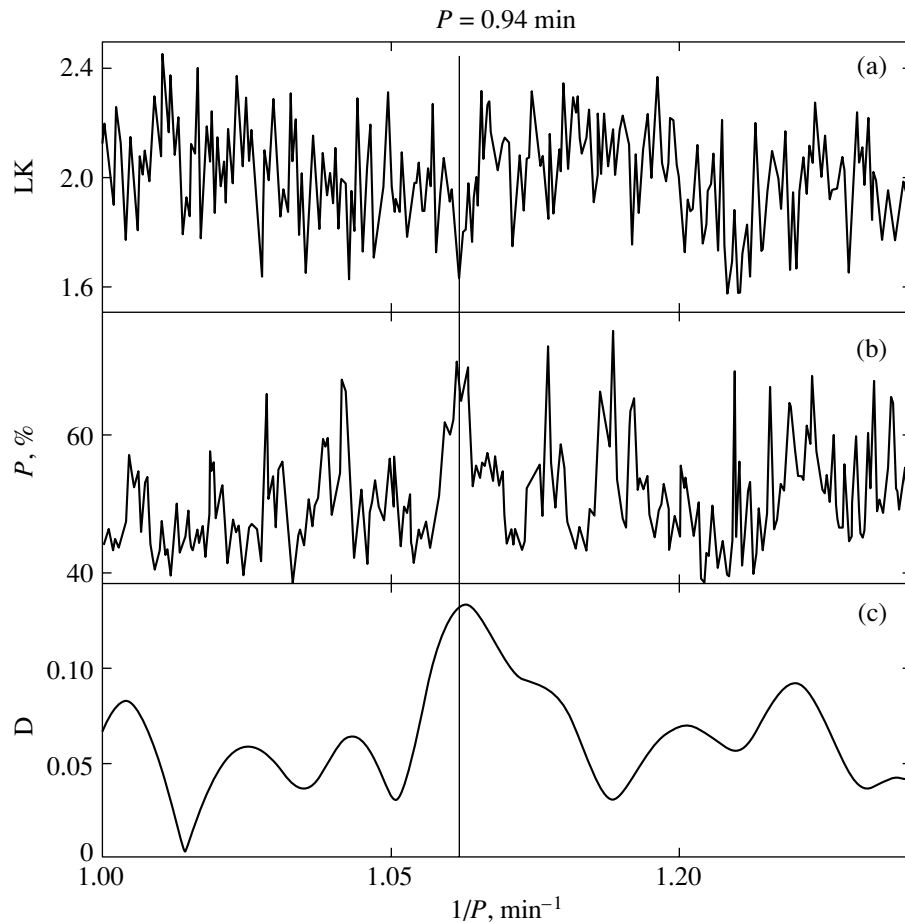
P = 0.94 min

Fig. 4. The periodograms obtained from the equivalent widths of the blue sodium emission component during its highest flaring activity on July 20 in the UT interval 18.00−19.17 h. We used the following period searching methods: (a) Lafler−Kinman, (b) Yurkevich, and (c) Deeming.

it occurred in the UT interval 18.0−18.5 h, which is marked by the hatched region in Fig. 2 (Rozenberg 1963). The duration of its highest intensity was 10−15 min. The variations in the equivalent widths of the sodium absorption line in Fig. 2 show that the dusk flare could change the sodium-line equivalent width by no more than 0.2 Å.

The July 20 spectra exhibited two emission components. The blue component was detected in all spectra. The time dependence of its equivalent width is shown in Fig 3. Its mean wavelength, FWHM, and equivalent width were 5857 ± 5 Å, 27 ± 3 Å, and 2.2 ± 0.1 Å, respectively. The latter changes from 0.6 Å to 5.2 Å, i.e., by almost a factor of 10.

The red emission component was detected only in 74 of the 207 spectra. Its mean wavelength, FWHM, and equivalent width were 5927 ± 5, 20 ± 3, and 0.7 ± 0.1 Å, respectively. The red component was weaker than the blue component by a factor of 3, on average. The latter may have been weakened by the

superposition of atmospheric water absorption bands (see Fig. 1). Several flares of the red component were recorded in the UT interval 18.0−19.1 h, when the blue component was most intense. At the remaining time, its equivalent width was ∼0.5 Å, comparable to the measurement errors.

Since the blue component was present in all spectra and since it was measured more reliably than the red component, all our studies (see below) were carried out using the blue Na D emission component. Given the measurement errors, its Doppler shift was 30 Å.

Variability Time Scale for the Sodium Emission

An analysis of the variability pattern for the blue Na D component, whose equivalent widths are shown in Fig. 3, suggests the existence of several rapid flares in a short UT interval, 18.00−19.17 h. A study of the time behavior of the emission based on a frequency analysis by the Deeming, Lafler−Kinman,
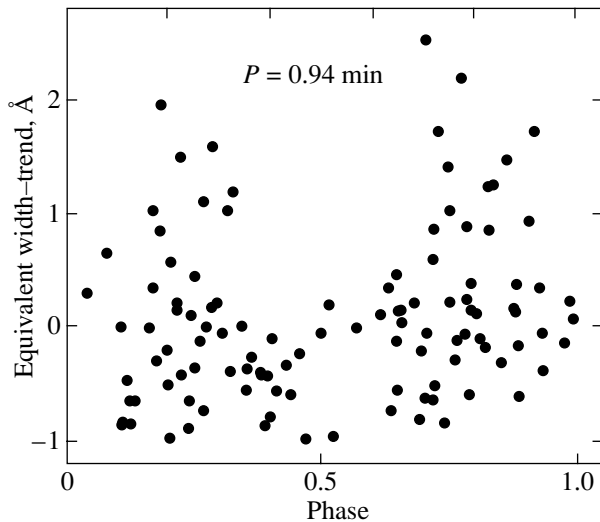
Fig. 5. The equivalent widths of the blue sodium emission component observed in the UT interval 18.00−19.10 h folded with a period of 0.95 min. Phases and equivalent widths are along the horizontal and vertical axes, respectively.

and Yurkevich methods revealed a quasi-periodicity. The analysis was performed after the subtraction of a linear trend. We found periods of 1, 1.3, and 2.7 min with probabilities up to 76% each in the UT interval 18.0−18.75 h and periods of 1, 2, and 3 min with probabilities >80% each in the UT interval 18.85−19.17 h, when the flares were brightest. The results of our analysis in the total UT interval 18.0−19.17 h are shown in Fig. 4. Plot (a) exhibits a period of 0.94 min; plot (b) confirms its presence with a possible frequency splitting, and the Deeming method yields a broad band near the frequency for this period. The data folded with the 0.94-min period (see Fig. 5) show that the flares are grouped at two phases of this quasi-period.

Generalizing our results, we may conclude that the sodium emission varies on a time scale of $\sim$1 min. This value is more than twice the time resolution of our observations, and the presence of multiple periods significantly increases its existence probability. Note that the periods found for different time intervals and for the combined series are virtually equal, which also increases the statistical significance of the inferred variability time scale for the Na D line emission.

Peculiarities of the Na D *Line Emission*

Summarizing the results obtained during the reduction of our observations, we list the main peculiarities of the sodium emission detected on July 20.

(1) The sequence of bright sodium flares (UT 18.0−19.17 h) had a mean UT of 18.6 h, and the brightest flares were detected in the UT interval 18.75−19.17 h.

(2) The strongest sodium emission was observed, on the average, 1.3 h before the Q fragments fell to Jupiter, when they were at a distance of $3R_J$ from its center.

(3) The recurrence time scale of the sodium flares observed during its highest activity (UT 18.0−19.17 h) was $\sim$1 min.

(4) We observed both blueward and redward Doppler shifts ($\sim$ 30 Å), which corresponded to velocities up to 1500 km s^{-1}. Note that when individual flares weakened, there was a clear tendency for the emission to broaden. The mean equivalent widths of the short- and long-wavelength components were 2.2 Å and a factor of 3 smaller (0.7 Å), respectively.

(5) The sodium emission was observed in projection onto Jupiter over its entire disk. Since sodium traveled to distances of $\sim$90000 km in a minute, the size of the emission region is estimated to be larger than the Jovian diameter, 140000 km.

These peculiarities suggest that the sodium emission took place in the Jovian inner magnetosphere at a distance of $3R_J$ from its center, where no sodium emission has ever been observed previously. It would be natural to assume that the cometary coma that surrounded the Q fragments was the source of sodium. Sodium was liberated as the coma was moving through the Jovian inner magnetosphere due to the interaction of the cometary material with magnetospheric plasma.

SODIUM RELEASE
FROM THE COMETARY COMA

The outer comas of the fragments from Comet SL 9 (Chernova *et al.* 1996), which consisted mostly of small particles, were partly detained far from Jupiter in its outer magnetosphere due to the interaction of charged small dust grains with the Jovian magnetic field (Fortov *et al.* 1996). The inner comas of the cometary fragments containing debris and large dust particles, which had long remained gravitationally bound to the cores (Medvedev and Chernetenko 1997), freely passed through the outer magnetosphere. According to various publications (Stüve *et al.* 1995; West 1995; Hahn *et al.* 1996), the medium-sized granules in the inner coma of the fragments from Comet SL 9 were larger than 0.1 mm, while the large granules exceeded 1 cm. It may well be that larger debris were also present. The properties of the dust particles in the coma around the fragments of Comet SL 9 were typical of the comets. The particles had porous mineral cores with a density of 1−2 g cm^{-3} surrounded by ice (Dollfus and Suchai

1987). The content of sodium and its compounds in the cometary coma grains were estimated by various authors to lie within the range from 2 to 0.5% (Kissel *et al.* 1986; Kissel and Kruger 1987). Studies of meteorites (Muller 1987) and spectroscopic studies of meteors (Smirnov 1994) yielded the same values. According to Dobrovol'skiĭ (1966), the coma particle sizes lie within the range $10^{-5}-10$ cm. Currently available measurements from spacecraft (Sagdeev *et al.* 1986; McDonnell *et al.* 1993) extended the range to small sizes, revealing particles with masses down to 10^{-16} g.

We observed the strongest sodium emission when the Q fragments were at distances of $\sim 3R_J$ from the Jovian center. At that time, according to the calculations by Yu.D. Medvedev, the debris of the Q fragments moved relative to the magnetosphere at a velocity of ~ 35 km s^{-1}. The number density of high-energy plasma particles and ions of oxygen, sulfur, and its compounds is known to be at a maximum in this part of the inner magnetosphere. We believe that here, sodium atoms were liberated most actively in the entire volume of the coma that surrounded the Q2 and Q1 fragments. The large coma fraction swept up high-energy protons and other particles from the magnetospheric plasma, much as is done by the Jovian satellites. This process was accompanied by the heating of the debris surfaces and by their subsequent cracking. Thus, as the fragments approached Jupiter, large cometary debris broke up further, fragmented, their surfaces eroded, and the fine dust was swept away and evaporated. These processes caused the number of cometary particles to increase in the magnetospheric plasma.

Sodium can be liberated from the cometary material through various processes. The most efficient process is the sputtering of material, although other interactions, particle desorption from the surface, secondary electron emission, and thermoemission may also play a role. During the sputtering of material, a fast particle that penetrated into the body produces a cascade of displaced atoms, some of which leave the solid body. The main characteristic of this process is the sputtering efficiency. It depends on the atomic number and mass of the ion, its energy, the angle of particle incidence, material, and its physical state (temperature, peculiarities of the surface structure, etc.). A characteristic feature of the sputtering is the dependence of its efficiency on the binding energy of the surface atoms. Therefore, one might expect sodium to be sputtered first.

Matson et al. (1974) first successfully used the sputtering mechanism to account for the formation of a torus and a sodium cloud near the Jovian satellite Io, which moves relative to the inner magnetospheric plasma of the planet at a velocity of 57 km s^{-1}. Given the sodium content on the Io surface (up to 10%), the sodium production rate was found to be 10^6-10^7 atoms cm^{-2} s^{-1}). More recent estimates of the sodium flux from the Io surface obtained from the data of Smith, McElroy, and Brown yielded a factor of 30 larger fluxes (Pilcher and Strobel 1982). These values provide the intensity of the observed emission from the torus and the sodium cloud near Io. It should be noted that these authors described sodium jets with velocities up to 100 km s^{-1}, which led them to conclude that there was an unknown acceleration mechanism.

Weaver *et al.* (1995) supposed that sputtering was also responsible for the Mg$^+$ (2800 Å) flare on July 14, 1994, when the large G fragment from Comet SL 9 interacted with the Jovian magnetosphere at a distance of $50R_J$. The grain sputtering and explosions through the accumulation of static electricity of the grain surfaces produced the emission of magnesium atoms, which lasted 18 min.

ESTIMATING THE NUMBER OF SODIUM ATOMS

A lower limit on the number of sodium atoms can be obtained by using the dust production rate derived by McGrath *et al.* (1995): 30 kg s^{-1} for distances of $\sim 6R_J$ from the Jovian center and more than $4R_J$ from its equatorial plane. Assuming the sodium weight content in this dust to be $\sim 1\%$, we find the production rate of sodium atoms for the above distance from Jupiter to be $\sim 10^{25}$ s^{-1}. During 1 h of the sodium emission, the number of its atoms is $N_p = 4 \times 10^{28}$. It would be natural to assume that this value will be considerably larger at a smaller distance from Jupiter, $\sim 3R_J$.

The sputtering efficiency as inferred from available empirical formulas for sputtering (Martynenko 1983) gives the total number of sodium atoms liberated in the inner magnetosphere in 1 h $N_{sp} \approx 4 \times 10^{29}$. This value is an order of magnitude larger than the estimate obtained from the data of McGrath *et al.* (1995), which is quite natural. Since the latter estimate is apparently closer to the actual value, we use it below.

To estimate the upper limit, we calculated the sodium mass in the Q1 and Q2 fragments, whose diameters were 2.9 and 2.2 km (see Weaver *et al.* (1995). Taking the mean sodium content in comets to be $\sim 1\%$ (Kissel *et al.* 1986; Kissel and Kruger 1987), we found that 4×10^{36} sodium atoms were contained in the two fragments. Since most of the components exploded in the Jovian atmosphere and since sodium was actively liberated from numerous debris of the
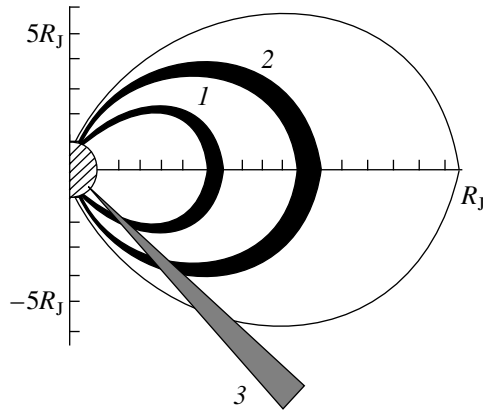
Fig. 6. The arrangement of plasma structures in the Jovian inner magnetosphere in the magnetic-meridian plane as inferred from the *Pioneer-10* data. Distances from the Jovian center in its radii are along the axes; *1* and *2* represent the current tubes of Io and Europa, respectively; *3* indicates the direction in which the Q fragments fell.

inner coma around the fragments during our observations, we may assume that 0.2% of the total amount of sodium could be involved in its observed emission. The upper limit on the number of sodium atoms is then $N_Q \approx 10^{34}$.

Using the equivalent widths of the blue sodium emission component, we can estimate the energy released during its emission by ignoring the contribution the weaker red component. For the energy calibration, we used the standard monochromatic flux produced by the Sun (Makarova *et al.* 1991, 1998). Near the Na D line at the Jovian distance, this flux is $E_J \cong 6.14$ erg cm^{-2} s^{-1} Å^{-1}. To estimate the total flux, we took the mean equivalent width of the blue component to be ~ 3 Å. The mean flux produced by the sodium emission is then $E_{Na} \cong 18.5$ erg cm^{-2} s^{-1}.

The sodium emission was observed almost over the entire planetary disk, which allows us to assume the size of the sodium emission region in the plane of the sky to be equal to the disk area S_J. The total energy radiated in a time $t \cong 3600$ s was estimated to be

$$E_0 = E_{Na} S_J t \cong 10^{25} \text{ erg.}$$

The value of E_0 was obtained under fairly rough assumptions. Nevertheless, it allows the sodium emission energy to be estimated in order of magnitude.

For the number of sodium atoms to be estimated from the emission energy, we must resort to the assumption of local thermodynamic equilibrium (LTE) during the highest sodium flaring activity. It is well known that plasma in LTE can be assumed to consist of elementary small volumes with a sufficiently high density inside which a thermodynamic equilibrium can exist for a short time.

The dust particle density in the atmospheres of comets near their nuclei, where collisions play a significant role (Gnedin and Dolginov 1966), is generally estimated to be 10^9 cm^{-3} (Egibekov 1969). In our case, when the particles of the inner coma actively break up, the local density of elementary particles could be much higher. Consequently, we may assume that it could reach 10^{11} cm^{-3} at some places, which is enough for the LTE hypothesis.

The number of sodium atoms at the second excitation level N_{21} at $h\nu = 3.1 \times 10^{-12}$ erg, the transition probability $A = 10^8$, and $E_0 \cong 10^{25}$ erg can be estimated from the expression (Frish 1963; Lebedeva 1994)

$$N_{21} = E_0/(h\nu A) = 4 \times 10^{28}.$$

It would be natural to assume that only a small fraction of sodium atoms was at the second excitation level. If this fraction is taken to be 1%, then the total number of atoms N_{Na} estimated from the emission energy of the resonance Na D line is $N_{Na} \approx 100 N_{21} \approx 4 \times 10^{30}$.

Comparing all estimates for the number of atoms, we see that the derived $N_{Na} \approx 4 \times 10^{30}$ is larger than the lower limit on the number of atoms estimated from the sputtering efficiency by only an order of magnitude and smaller than the upper limit by almost four orders of magnitude.

Consequently, $N_{sp} < N_{Na} \ll N_Q$.

Thus, even rough estimates show that the cometary sodium contained in the Q fragments was more than enough to provide the observed sodium emission energy.

A POSSIBLE FORMATION MECHANISM FOR THE HIGH-SPEED CLOUDS OF SODIUM ATOMS

In our view, the high-speed clouds of sodium were produced by a collection of several physical processes. These processes led to the ionization of sodium atoms and their acceleration, as well as to the recombination and emission of the resonance sodium line, which is briefly considered below.

Sodium could be ionized primarily by the mechanism of anomalous critical ionization. This mechanism was described by the Swedish scientist Alfvén in 1962. Its essence is that a flow of weakly ionized plasma whose velocity exceeds some critical value collides with a magnetic field to generate plasma turbulence, which accelerates the background plasma quasi-thermal electrons to energies of several tens of keV. The low-energy electrons accelerated in this

way, whose density under the magnetospheric conditions proves to be high enough, collide with neutral atoms to produce an avalanche-like ionization of the latter.

To elucidate the physical conditions for the acceleration of sodium ions, we turn to the geometry of the passage of the Q fragments through the Jovian inner magnetosphere. Figure 6 shows its scheme in the plane of the magnetic meridian (Intriligator and Wolfe 1976); the arrow indicates the path of the Q fragments. Note that the leading Q2 fragment at the beginning of the series of bright flares (UT 18.0 h) was at a distance of $3.2R_J$; when the bright flares ended (UT 19.17 h), the Q1 fragment was at a distance of about $2.7R_J$. Consequently, the occurrence of the brightest sodium flares was determined by the times the fragments crossed the Io–Jupiter current tube (Goertz and Boswell 1979), which intersects with the comet trajectory at a distance of $\sim 3R_J$.

An Alfvén wave with a characteristic period of ~ 1 min is known to emerge and propagate in the current tube. We found the same time scale of flaring activity in the sodium emission. The equality of these values confirms that the sodium emission is related to the passage of the Q fragments through the Io–Jupiter current tube. Thus, we may conclude that the sodium ions were accelerated by the large-scale bidirectional electric fields generated in the current tube by the Io motion.

The sodium ions were neutralized during nonresonant charge exchange, and the observed resonance line of atomic sodium was emitted during recombinations. Note that according to our scenario, the D line emission must also be accompanied by the emission of sodium ion lines. Since these lie in the far ultraviolet where no observations were carried out at that time, there is no information on their emission.

CONCLUSIONS

The CrAO spectroscopic observations of the Jovian disk features on July 20, 1994, have allowed the interaction of the cometary material with its magnetosphere to be recorded for the first time. This interaction manifested itself in the Na D line emission. An analysis of this emission showed that it was observed in the form of two components with Doppler shifts of ~ 30 Å, which corresponded to velocities of sodium atoms ~ 1500 km s^{-1}. The sodium emission was observed when the Q fragments passed through the current tube of the Jovian satellite Io at a distance of $3R_J$ from its center. The size of the sodium emission region (larger than 140000 km) may provide evidence for the appearance of sodium atoms in large quantities, suggesting their association with the cometary coma. An analysis of the mechanisms

that could supply sodium from the cometary material in the Jovian inner magnetosphere confirmed the previous assumption that the cometary sodium emission was observed. Assuming the sputtering to be the most efficient process, we obtained rough estimates for the number of sodium atoms liberated from the cometary material, on the one hand, and from the D-line emission energy, on the other. There was good agreement in our estimates.

We proposed a scenario for the formation of high-speed clouds of sodium atoms, which appear because of sodium ionization, ion acceleration, and D-line recombination and emission. In our view, these physical mechanisms can account for the observed emergence of high-speed clouds of sodium atoms when the cometary material interacts with the magnetospheric plasma.

Note that high-speed (up to 300 km s^{-1}) clouds of ionized calcium were detected by Gulyaev and Shcheglov (1999) during a solar eclipse in the dust component of the solar corona. This phenomenon may have a similar physical nature.

In conclusion, we note that theorists did not predict the emergence of rapidly moving sodium clouds in the Jovian magnetosphere when the cometary coma passed through it. No observations similar to ours were carried out, and attention was entirely focused on investigating the fragment explosions in the Jovian atmosphere and on their effects.

ACKNOWLEDGMENTS

REFERENCES

1. A. N. Abramenko, V. V. Bochkov, L. G. Karachkina, *et al.*, Astron. Vestnik **30**, 112 (1996).
2. S. Catalano, M. Rodono, M. Ventuta, and A. Cacciani, in *Proceedings of the European Shoemaker-Levy 9th Conference: ESO Conference and Workshop Proceedings No. 52, Garting bei Munchen, 1995,* Ed. by R. West and H. Bohnhardt, p. 209.
3. G. P. Chernova, K. Jockers, and N. N. Kiselev, Icarus **121**, 38 (1996).
4. O. V. Dobrovol'skiĭ, *Comets* (Nauka, Moscow, 1966).
5. A. Dollfus and J.-L. Suchai, ESO Messenger **47**, 39 (1987).
6. P. Egibekov, Probl. Kosm. Fiz. **4**, 78 (1969).

7. A. Fitzsimmons, J. E. Little, N. Walton, *et al.*, in *Proceedings of the European Shoemaker–Levy 9th Conference: ESO Conference and Workshop Proceedings No. 52, Garting bei Munchen, 1995,* Ed. by R. West and H. Bohnhardt, p. 197.

8. V. E. Fortov, Yu. N. Gnedin, M. F. Ivanov, *et al.*, Usp. Fiz. Nauk **166**, 390 (1996) [Phys. Usp. **39**, 363 (1996)].

9. S. Ě. Frish, *Optical Spectra of Atoms* (Fizmatgiz, Moscow, 1963).

10. G. R. Gladstone, D. T. Hall, and J. H. Waite, Jr., Science **286**, 1595 (1995).

11. Yu. N. Gnedin and A. Z. Dolginov, Astron. Zh. **43**, 161 (1966) [Sov. Astron. **10**, 143 (1966)].

12. C. K. Goertz and R. W. Boswell, J. Geophys. Res. **84**, 7239 (1979).

13. R. A. Gulyaev and P. V. Shcheglov, Dokl. Akad. Nauk **366**, 199 (1999) [Dokl. Phys. **44**, 309 (1999)].

14. J. M. Hahn, T. W. Rettig, and M. J. Mumma, Icarus **121**, 291 (1996).

15. D. S. Intriligator and J. H. Wolfe, in *Jupiter,* Ed. by T. Gerels (Univ. of Arizona Press, Tuscon, 1976; Mir, Moscow, 1979).

16. J. Kissel, D. E. Brownlee, K. Buchler, *et al.*, Nature **321**, 336 (1986).

17. J. Kissel and F. R. Kruger, Nature **326**, 755 (1987).

18. V. V. Lebedeva, *Experimental Optics* (Mosk. Gos. Univ., Moscow, 1994).

19. E. A. Makarova, A. V. Kharitonov, and T. V. Kazachevskaya, *Solar Flux* (Nauka, Moscow, 1991).

20. E. A. Makarova, A. V. Kharitonov, T. V. Kazachevskaya, *et al.*, Baltic Astron. **7**, 467 (1998).

21. Yu. V. Martynenko, Itogi Nauki Tekh., Ser. Fiz. Plazmy **3**, 119 (1983).

22. D. L. Matson, T. V. Johnson, and F. P. Fanale, Astrophys. J. Lett. **192**, L43 (1974).

23. J. A. M. McDonnell, N. McBride, R. Beard, *et al.*, Nature **362**, 732 (1993).

24. M. A. McGrath, D. T. Hall, P. L. Matheson, *et al.*, Science **267**, 1313 (1995).

25. Yu. D. Medvedev and Yu. A. Chernetenko, in *Proceedings of the All-Russia Conference with International Participation "Problems of Celestial Mechanics,"* Ed. by A. G. Sokol'skiĭ and A. S. Baranov (ITA, MIPAO, St. Petersburg, 1997), p. 121.

26. O. Müller, Earth Sci. **27**, 35 (1987).

27. C. B. Pilcher and D. F. Strobel, in *Satellites of Jupiter,* Ed. by D. Morrison (Univ. of Arozona Press, Tucson, 1982; Mir, Moscow, 1986), Vol. 3.

28. V. V. Prokof'eva and V. P. Tarashchuk, Astron. Vestnik **30**, 140 (1996a).

29. V. V. Prokof'eva and V. P. Tarashchuk, Kinematika Fiz. Nebesnykh Tel **12**, 82 (1996b).

30. V. V. Prokof'eva, V. P. Tarashchuk, V. M. Lyutyĭ, and V. G. Metlov, Pis'ma Astron. Zh. **22**, 858 (1996) [Astron. Lett. **22**, 771 (1996)].

31. V. V. Prokof'eva, V. P. Tarashchuk, and K. I. Churyumov, Astron. Astrophys. Trans. **13**, 199 (1997).

32. M. Rose-Serot, A. Barucci, J. Crovisier, *et al.*, in *Proceedings of the European Shoemaker–Levy 9th Conference: ESO Conference and Workshop Proceedings No. 52, Garting bei Munchen, 1995,* Ed. by R. West and H. Bohnhardt, p. 203.

33. G. V. Rozenberg, in *Twilight* (Fizmatgiz, Moscow, 1963), p. 380.

34. R. Z. Sagdeev, J. Blamont, A. A. Galeev, *et al.*, Nature **321**, 259 (1986).

35. Z. Sekanina, in *Proceedings of the European Shoemaker–Levy 9th Conference: ESO Conference and Workshop Proceedings No. 52, Garting bei Munchen, 1995a,* Ed. by R. West and H. Bohnhardt, p. 29.

36. Z. Sekanina, in *Proceedings of the European Shoemaker–Levy 9th Conference: ESO Conference and Workshop Proceedings No. 52, Garting bei Munchen, 1995b,* Ed. by R. West and H. Bohnhardt, p. 43.

37. V. A. Smirnov, *Spectra of Momentary Atmospheric Light Phenomena: Meteors* (Fizmatgiz, Moscow, 1994).

38. J. A. Stüve, R. Schulz, and F. M. A'Hearn, in *Proceedings of the European Shoemaker–Levy 9th Conference: ESO Conference and Workshop Proceedings No. 52, Garting bei Munchen, 1995,* Ed. by R. West and H. Bohnhardt, p. 17.

39. H. A. Weaver, M. F. A'Hearn, C. Arpigny, *et al.*, Science **267**, 1282 (1995).

40. R. M. West, in *Proceedings of the European Shoemaker–Levy 9th Conference: ESO Conference and Workshop Proceedings No. 52, Garting bei Munchen, 1995,* Ed. by R. West and H. Bohnhardt, p. 407.

Translated by V. Astakhov

An Upper Limit on the X-ray Luminosity of the Microlensing Black Hole OGLE-1999-BUL-32

M. G. Revnivtsev[1, 2, *] and R. A. Sunyaev[1, 2]

[1]*Space Research Institute, Russian Academy of Sciences, Profsoyuznaya ul. 84/32, Moscow, 117810 Russia*
[2]*Max-Planck Institut für Astrophysik, Karl Schwarzschild Strasse 1, 86740 Garching bei München, Germany*
Received September 7, 2001

Abstract—Having analyzed the 1999 scanning observations of the Galactic-center region with the PCA spectrometer onboard the RXTE observatory, we obtained upper limits on the flux from the microlensing black hole OGLE-1999-BUL-32 in 1999−2000. We show that the X-ray luminosity of this black hole did not exceed $L_X \lesssim 3 \times 10^{33}(d/1\text{kpc})^2$ erg s^{-1}. Near the maximum amplification of the background star (on June 6, 1999), the upper limit was $L_X \lesssim 7 \times 10^{33}(d/1\text{kpc})^2$ erg s^{-1}. © *2002 MAIK "Nauka/Interperiodica".*

Key words: *RXTE/PCA, black holes, X-ray binaries, gravitational microlenses, interstellar medium*

INTRODUCTION

The possibility of observing gravitational microlensing, an apparent brightening of a background object through ray bending in the field of a gravitating object (lens) that crosses the observer's line of sight, was noted back in 1970−1980 [see Paczynski (1996) for a review]. However, because of the severe technical difficulties involved in observing and selecting such events, only in recent years have two instrumental groups (MACHO and OGLE) made great progress. More than a thousand Galactic microlensing events are known to date (Alcock *et al.* 2000; Wozniak *et al.* 2001).

When a lensing object passes between the observer and a background star, the observed flux from the latter varies in a certain fashion (Paczynski 1986). The variation time scale for the observed stellar flux is determined by the lens mass and by the distances to the lens and the background star. Theoretical and practical studies of the probability densities for microlensing time scales have shown that the probability of events with time scales of ∼100 days is highest (Paczynski 1996; Alcock *et al.* 2000), indicating that the mass of the lensing objects is of the order of the solar mass.

Recent, more detailed studies of the longest detected microlensing event OGLE-1999-BUL-32 (Mao *et al.* 2001; the MACHO group designated this event as MACHO-99-BLG-22) strongly suggest that in this case, the lens is a black hole. Mao *et al.*

(2001) have shown that the mass of the object is $M \sim 200 M_\odot$ if the lens is ∼500 pc away and $M \sim 4.4 M_\odot$ if its distance is ∼6 kpc (assuming the background star to be in the bulge and its distance to be $d_{\text{st}} \sim 7$ kpc). In any case, the mass of the lensing object exceeds the mass limit for a neutron star. Thus, the observation of the microlensing event OGLE-1999-BUL-32 suggests that there is a black hole with the mass $> 4 M_\odot$ in the direction with the coordinates $l = 2.46$ and $b = -3.505$ or $\alpha = 18^\text{h}05^\text{m}05\overset{\text{s}}{.}35$ and $\delta = -28°34'42''\!.5$. The amplification of the flux from the background star was at a maximum on July 6, 1999 (∼TJD 11365).

Here, we publish upper limits on the X-ray luminosity of this black hole based on RXTE/PCA scanning data for the Galactic center.

OBSERVATIONS

There are three instruments onboard the RXTE orbiting observatory: two coaligned spectrometers with a common 1° field of view (PCA and HEXTE) and an all-sky monitor (ASM). The ASM monitors the long-period variability of sources in the energy range 1−12 keV with a sensitivity ∼6−10 mCrab per day. The PCA spectrometer has a large effective area (∼6500 cm^2), with its field of view being relatively small (1°). This spectrometer has regularly (approximately twice a weak) scanned the Galactic-center region since 1999; the errors in the source fluxes for each scan are ∼1−2 mCrab per scan. Thus, the PCA scanning data for the Galactic center effectively supplement the ASM data. Note that even in
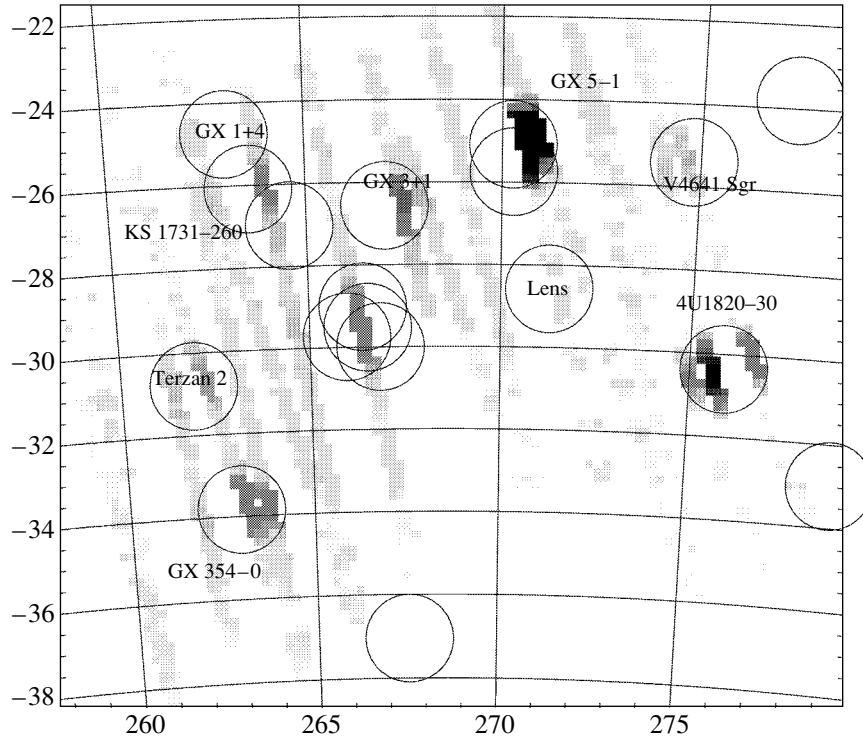
*E-mail: `revnivtsev@hea.iki.rssi.ru`

Fig. 1. The X-ray image of the Galactic-center region as obtained from the RXTE/PCA scanning observations on July 7, 1999. The exposed regions of bright X-ray sources are indicated by circles (see the text).

the scanning mode, the PCA sensitivity exceeds the ASM sensitivity by an order of magnitude. This gain in sensitivity is particularly important if the event of

Fig. 2. PCA scans across weak X-ray sources and the lens OGLE-1999-BUL-32 on July 7, 1999.

interest is too short to be recorded by the ASM with a sufficient accuracy.

The PCA spectrometer has regularly scanned the Galactic-center region (approximately twice a weak) since 1999. We reduced ~100 available scanning observations. One of these observations was carried out on July 7, 1999, i.e., virtually during the maximum amplification of the background star by the lens OGLE-1999-BUL-32.

The PCA data were reduced with the LHEASOFT software package. The $L7/240$ model was used to estimate the PCA background.

The map of the Galactic-center region obtained by analyzing the PCA scanning observations on July 7, 1999, is shown in Fig. 1 (the energy band is ~3–20 keV). When constructing the map, we ascribed the PCA flux detected over a period of 1 s to the point that corresponded to the center of the PCA field of view. For this method of imaging the sky, regions of the sky within 1° of the sources will be "exposed" in accordance with the radial dependence of the collimator transmission function. Such exposed areas (circles) from the well-known bright sources 4U 1820−30, GX 5−1, GX 3+1, and GX 354−0 are clearly seen on the map in Fig. 1. Even relatively weak sources, such as Terzan 2 and the accreting black hole in the high-mass X-ray binary V4641 Sgr (the flux from these sources was ~15−25 mCrab), are seen in this map.
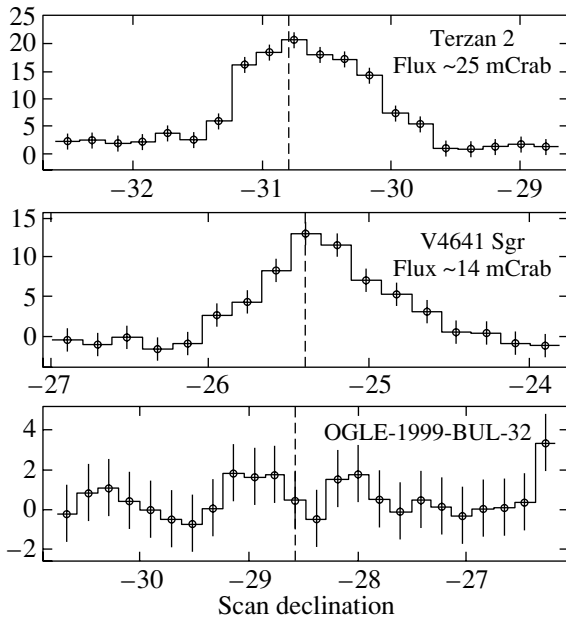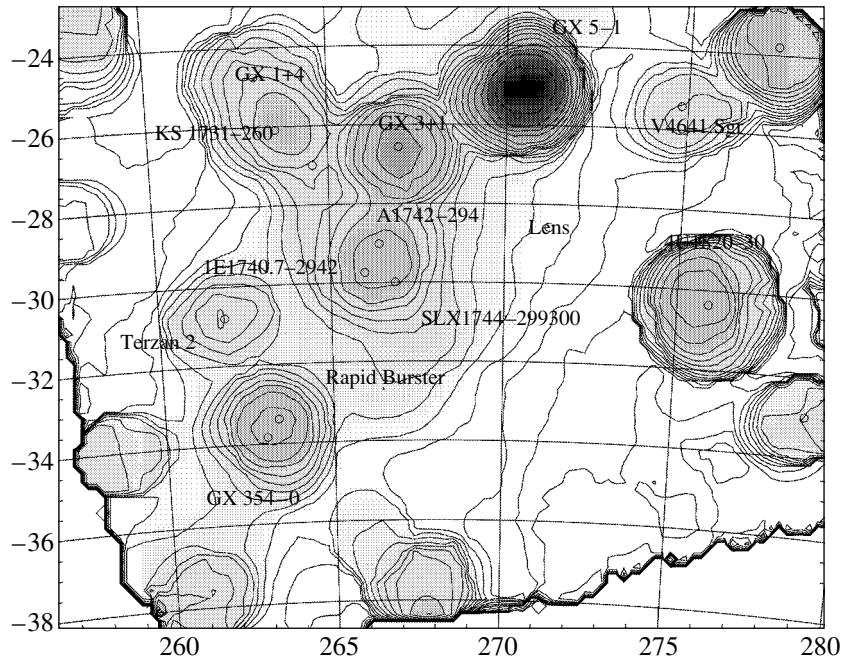
Fig. 3. The X-ray image of the Galactic-center region as obtained from the RXTE/PCA scanning observations between February 1999 and March 2000.

For comparison, Fig. 2 shows individual PCA scans across the weak sources Terzan 2 and V4641 Sgr and the presumed black hole (lens). The X-ray flux from OGLE-1999-BUL-32 in the energy range $\sim 3-20$ keV during this specific observation was no higher than $1-2$ mCrab.

Figure 3 also shows the map of the Galactic-center region as constructed from all PCA scanning data (from February 1999 until March 2000). Note that, despite a significant improvement in statistics (~ 100 PCA scanning observations were used), systematic uncertainties in the background subtraction and a contribution of the diffuse Galactic background to the PCA flux detected near the Galactic plane prevent a great improvement in the upper limit on the flux from OGLE-1999-BUL-32, $F_X \lesssim 1$ mCrab.

DISCUSSION

In the preceding section, we showed that the upper limit on the flux from the presumed black hole OGLE-1999-BUL-32 is $\lesssim 1$ mCrab, which corresponds to the X-ray luminosity $L_{3-20\,\mathrm{keV}} \lesssim 3 \times 10^{33}\,(d/1\mathrm{kpc})^2$ erg s^{-1}, where d is the distance to the source.

Our constraints on the X-ray luminosity of the black hole OGLE-1999-BUL-32 can be useful in models where a black hole is a member of a binary.

Observations of X-ray novae, low-mass binaries with black holes, have shown that there are thousands of recurrent transient X-ray sources in the

Galaxy, which actively manifest themselves only for several months every $50-70$ years [see Tanaka and Shibazaki (1996) for a review]. The discovery of an X-ray outburst in the high-mass binary V4641 Sgr indicates that black holes, which are virtually unobservable in X rays, also exist in high-mass X-ray binaries (Orosz *et al.* 2001). However, it is clear that a bright massive optical component of the binary would be detected during microlensing observations. Thus, the hypothesis of a black hole in a high-mass X-ray binary seems implausible, while the question of whether the detected black hole is a member of a low-mass binary is still an open question only if the black hole is far away ($d \gtrsim 3-4$ kpc). For a nearby ($d \sim 500$ pc), massive ($M \sim 200 M_\odot$) black hole in the binary, microlensing observations would inevitably reveal an optical component with a mass of $M \gtrsim 0.2 M_\odot$. Thus, we conclude that such a massive black hole must be single.

Observations show that the molecular-hydrogen column density toward OGLE-1999-BUL-32 is not very large, $NHL \sim 5 \times 10^{18}$ cm^{-2} (Dame *et al.* 1987), while the neutral-hydrogen column density is much larger, $NHL \sim 3 \times 10^{21}$ cm^{-2} (Dickey and Lockman 1990). This implies that the possible ultraviolet or soft ($h\nu \lesssim 0.5$ keV) X-ray radiation from the source would be strongly absorbed.

According to McKee and Ostriker (1977), most of the Galactic disk is occupied by a rarefied gas.

The relatively low molecular-hydrogen column density suggests that the black hole OGLE-1999-BUL-32 is unlikely to be located in a molecular cloud. However, it may be in a cloud of neutral hydrogen. In that case, it can accrete a substantial amount of material to be detectable in X rays.

Gas turbulence and rotation in any interstellar cloud during accretion onto a black hole must give rise to an accretion disk. If no advection-dominated accretion flow (ADAF) is formed in the inner parts of the accretion disk, then the disk radiation can be roughly described by the spectrum of a multicolor disk (Shakura and Sunyaev 1973). At modest accretion rates, which most likely take place in our case, the maximum temperature in the accretion disk does not exceed 0.5 keV. Thus, the bulk of the energy release from such an accretion disk virtually falls outside our energy range $\sim$3−20 keV. This makes it very difficult to estimate an upper limit on the bolometric luminosity of the black hole from the RXTE measurements. Chandra and XMM-Newton (the operating energy range is 0.1−10 keV) X-ray observations of OGLE-1999-BUL-32 could yield a more accurate estimate of its bolometric luminosity. Unfortunately, if most of the radiation is emitted in the ultraviolet, then the source will be very difficult to detect because of interstellar extinction.

In the preceding section, we showed that one of the PCA scanning observations was carried out a day after the background star underwent the maximum amplification by the microlens (cf. the lens passage time scale of $\sim$640 days). The upper limit on the flux from the sky region near the background star/microlens during this observation is $F_X \lesssim 2.5$ mCrab (2σ). Given that the maximum amplification of the flux from the background star is $\sim$12.5 times, we can also put an upper limit on the X-ray luminosity of the background star (by assuming that it lies in the Galactic bulge at a distance of $d \sim 7$ kpc): $L_X \lesssim 2 \times 10^{34}$ erg s^{-1}. This upper limit is not very stringent either, and its value exceeds the luminosity of even the strongest X-ray solar flares.

The detection of a massive, invisible (in X rays) object suggests that black holes are by no means exotic objects in the interstellar medium. Clearly, some of them can occasionally pass through dense molecular clouds and clouds of interstellar gas. In this case, these objects can become X-ray sources detectable at the RXTE sensitivity level.

Unfortunately, a source with a luminosity $L_X > 10^{37}$ erg s^{-1} can heat the surrounding gas up to temperatures of 10^7 K in a short time, which will lead to its rapid outflow and to the formation of a low-density cavity. A consequence of this pattern will be a turnoff of the accretion onto a compact object even in a fairly dense medium (Sunyaev 1978).

REFERENCES

1. C. Alcock, R. Allsman, D. Alves, *et al.*, Astrophys. J. **541**, 734 (2000).
2. T. Dame, H. Ungerechts, R. Cohen, *et al.*, Astrophys. J. **322**, 706 (1987).
3. J. Dickey and F. Lockman, Annu. Rev. Astron. Astrophys. **28**, 215 (1990).
4. C. McKee and J. Ostriker, Astrophys. J. **218**, 148 (1977).
5. S. Mao, M. Smith, P. Wozniak, *et al.*, Mon. Not. R. Astron. Soc. (2001) (in press); astro-ph/0108312.
6. J. Orosz, E. Kuulkers, M. van der Klis, *et al.*, Astrophys. J. **555**, 489 (2001).
7. B. Paczynski, Astrophys. J. **304**, 1 (1986).
8. B. Paczynski, Astrophys. J. Lett. **371**, L63 (1991).
9. B. Paczynski, Annu. Rev. Aston. Astrophys. **34**, 419 (1996).
10. N. Shakura and R. Sunyaev, Astron. Astrophys. **24**, 337 (1973).
11. R. A. Sunyaev, Pis'ma Astron. Zh. **4**, 75 (1978) [Sov. Astron. Lett. **4**, 39 (1978)].
12. Y. Tanaka and N. Shibazaki, Annu. Rev. Astron. Astrophys. **34**, 607 (1996).
13. P. Wozniak, A. Udalski, M. Szymanskiet, *et al.*, Acta Astron. (2001) (in press); astro-ph/0106474.

Translated by V. Astakhov

Quasi-Periodic X-ray Oscillations in the Source Cygnus X-2

S. I. Kuznetsov[1,2,*]

[1]*Space Research Institute, Russian Academy of Sciences, Profsoyuznaya ul. 84/32, Moscow, 117810 Russia*
[2]*Service d'Astrophysique, Centre d'Etudes Nucleaires de Saclay, 91191 Gif-sur-Yvette Cedex, France*
Received September 21, 2001

Abstract—The RXTE observations of Cyg X-2 during 1996–1999 are presented. The properties of quasi-periodic oscillations (QPOs) are analyzed in detail. A new method of averaging the power-density spectra obtained during various observations is used to search for kHz QPOs. Its distinctive feature is the grouping of observations not only by spectral characteristics of the source's X-ray radiation but also by its temporal characteristics. The results obtained are used for an analysis in terms of the transition-layer model (TLM) and the relativistic-precession model (RPM) for a slowly rotating neutron star. Theoretical predictions of the two models are compared, and their self-consistency is verified. The tilt of the magnetosphere to the accretion-disk plane and the neutron-star mass and angular momentum are determined using these models. The distance to the source is estimated from observational data.
© 2002 MAIK "Nauka/Interperiodica".

Key words: *neutron stars, Cygnus X-2, X-ray sources, quasi-periodic oscillations*

1. INTRODUCTION

Cygnus X-2 belongs to low-mass X-ray binaries with accreting neutron stars. It is one of the brightest X-ray sources. By its spectral properties, Cyg X-2 belongs to Z-type sources (Hasinger and van der Klis 1989) whose characteristic feature is a Z-shaped track in the color–color diagram. In this interpretation, the spectral properties are presented in the hard–soft color indices, each of which is the harder-to-softer flux ratio in the corresponding energy band. The Z-shaped track is commonly divided into three parts called branches: the horizontal (HB, the upper part of the diagram), normal (NB, the intermediate part), and flaring (FB, the lower part) branches. The position on the Z track is generally believed to be associated with the rate of accretion in the direction from HB to FB. Six sources are currently known to exhibit Z tracks in the color–color diagram: Scorpius X-1, Cygnus X-2, GX 17+2, GX 5–1, GX 340+0, and GX 349+2.

Significant variations in the branch positions in the color–color diagram on time scales of the order of several days (Kuulkers *et al.* 1996) are a peculiarity of the Z track for Cyg X-2. In addition, EXOSAT observations revealed at least three intensity levels (the so-called low-, intermediate-, and high-state episodes; Kuulkers *et al.* 1996); the Z-track profiles in the color–color and color–intensity diagrams differed in each of these episodes. These peculiarities

make it difficult to analyze the temporal properties of the source based on the data grouping according to the position on the Z track. However, the above method was successfully applied to Z type and Atoll sources (Homan *et al.* 2001; Di Salvo *et al.* 2001). It allowed the properties of quasi-periodic oscillations (QPOs) in low-mass X-ray binaries to be studied in more detail.

The power-density spectra (Fourier transforms of the flux) of Z-type sources exhibit low-frequency (5–100 Hz) X-ray QPO peaks. The names of the QPOs correspond to the branch with which their origin is identified: horizontal- (HBO), normal- (NBO), and flaring-branch (FBO) oscillations. HBOs (15–100 Hz) can also be detected in the NB spectral state. However, as one recedes from HB, the statistical significance of the QPO peaks decreases, and they become undetectable. When moving along the Z track (from HB to FB) in its NB–FB segment, a QPO peak detectable in the range 5–20 Hz (HBO/FBO) emerges in the power-density spectra. For all the currently known Z-type sources, QPOs were also found in the range 200–1100 kHz (van der Klis 2000). Two kHz QPO peaks (ν_1 and ν_2 are the lower and upper peaks, respectively) can be simultaneously observed with a frequency difference of ~200–400 Hz. An increase in the flux is accompanied by an increase in the frequencies of the two peaks, but their difference ($\Delta\nu = \nu_2 - \nu_1$) is not preserved. Only one of the two peaks, the upper kHz QPO peak ν_2, can often be found in the power-density spectra; the significance of its detection is higher in most cases. For low-mass

*E-mail: sik@hea.iki.rssi.ru

X-ray binaries, direct observations cannot always reveal the second, generally lower, kHz QPO peak ν_1. The Atoll source 4U 1608−52 was observed by using the shift and add method (Mendez *et al.* 1998), which allowed the statistical significance of one of the QPO peaks to be increased if the other was reliably determined. In this case, it will suffice to linearly shift the frequencies for several initial power-density spectra in such a way that the frequency of one (observed) peak (for example, ν_2) is the same in all spectra. By this means, the statistical significance of kHz QPO detection could be increased in the average spectrum among all the individual spectra modified in such a way. Unfortunately, the application of this method is limited by the necessity of having at least one of the two QPO peaks.

The observations of Cyg X-2 revealed all the QPO types characteristic of the low-frequency range (<100 Hz) in the power-density spectrum. At high frequencies, two QPO peaks (ν_1 and ν_2) were found in the RXTE/PCA data for July 2, 1997 [first detected by Wijnands *et al.* (1998)]. Here, we analyze the QPO properties in detail. In searching for kHz QPO peaks, we used a new method of averaging the power-density spectra. This method is based on the grouping of observations not according to the position on the Z track but according to the temporal properties of the source's X-ray radiation. The results obtained are used for an analysis in terms of the transition-layer model (TLM) and the relativistic-precession model (RPM). We compare theoretical predictions of the two models and verify their self-consistency.

2. DATA AND OBSERVATIONS

For our time analysis, we used the data of the PCA (Proportional Counter Array) instrument (Jahoda *et al.* 1996) onboard the RXTE observatory (Bradt *et al.* 1993) retrieved from the Goddard Space Flight Center Electronic Archive.

The X-ray source Cyg X-2 was observed from the RXTE observatory during nine series of directed observations (10063, 10065, 10066, 10067, 20053, 20057, 30046, 30418, 40017): in March, August, and October 1996; in June, July, and September 1997; in July 1998; and in separate sessions from July until October 1998 and from January until August 1999. The observations of Cyg X-2 over this period correspond to three different observational epochs of RXTE/PCA (2, 3, and 4 in the adopted classification), for which the boundaries of the PCA energy channels were changed.

To construct the power-density spectra, we used observational data with a resolution of $\sim$122 μs (2^{-13} s) from the 14th to 249th PCA energy channels.

This range corresponds to a detectable photon flux up to $\sim$60 keV, whose lower limit begins from $\sim$4.3 keV, $\sim$5.0−5.3 keV, and $\sim$5.8 keV for epochs 2, 3, and 4, respectively. In this energy band, the detection of the QPOs that correspond to the horizontal branch of the Z track is most significant.

We combined some of the observational data that were not presented in a single format for all channels from the 14th to 249th but that were broken down into several ranges. Of all the observations, we used only those during which the angle between the source direction and the Earth's horizon was $>10°$ and the PCA axis was offset from the target by no more than $0°.02$. Among the observations of Cyg X-2, all five proportional counters were not always switched on to record events. If the operating condition of one of the counters changed during a continuous observation (whose duration did not exceed the duration of one orbit and was, on the average, 3−3.5×10^3 s), then the time interval during which the total count rate changed abruptly was excluded from our analysis. As a result of this filtering, the total usable observational time for Cyg X-2 was more than 4×10^5 s.

We constructed the power-density spectra (van der Klis 1989) in the range $0.03125 − 128$ Hz to analyze the low-frequency (<100 Hz) variability of Cyg X-2 and in the band 128−2048 Hz to search for kHz QPO peaks. No corrections were made for the background radiation and dead time (attributable to the inability of the instrument to record the next event during a very short interval).

We analyzed individual observations with a duration up to $\sim 3.5 \times 10^3$ s. Fitting the power-density spectra by a constant and by a power law at frequencies below and above the break frequency did not yield acceptable results (according to the χ^2 test). The main reason was the absence of a sharp break and the resulting uncertainty in its measurement. A model in which at frequencies much higher ($\nu/\nu_{\mathrm{break}} \gg 1$) and much lower ($\nu/\nu_{\mathrm{break}} \ll 1$) than the break, each part of the spectrum could be fitted by its own power law and the transition between them was not jumplike proved to be more suitable

$$P(\nu) = A\nu^{-\alpha}[1 + (\nu/\nu_b)^{\beta}]^{-1}. \qquad (1)$$

The power-density spectra were fitted in the 0.1−128-Hz band by using this model with the additional introduction of one or two Lorenz lines to allow for the QPO peaks and harmonics. To take into account the PCA dead-time effect, which causes the overall level to be shifted to the negative region [because of this effect, the Poissonian noise level subtracted from all spectra differs from 2.0, in Lehi normalization units; see van der Klis (1989) and Vikhlinin *et al.* (1994) for more details], we added a constant to the general model.

Table 1. Best-fit parameters for the average power-density spectra

Parameter	1	2	3	4	5	6	7	8
$\nu_{\frac{1}{2}\text{HBO}}$	8.60 ± 0.19	14.26 ± 0.38	14.19 ± 0.32	17.59 ± 0.82	20.01 ± 2.42	$-$	22.37 ± 1.45	$-$
FWHM	3.1 ± 0.7	6.0 ± 1.3	5.0 ± 1.3	13.4 ± 3.8	16.0 ± 7.1	$-$	19.5 ± 4.2	$-$
ν_{HBO}	17.13 ± 0.03	27.61 ± 0.06	28.40 ± 0.07	35.63 ± 0.31	43.80 ± 0.29	44.70 ± 0.35	49.96 ± 0.34	53.86 ± 0.19
FWHM	4.30 ± 0.07	4.40 ± 0.15	6.05 ± 0.21	8.79 ± 0.85	8.94 ± 0.79	7.89 ± 1.16	13.87 ± 1.04	10.66 ± 0.73
$\nu_{2\text{HBO}}$	32.68 ± 0.15	54.61 ± 0.47	55.04 ± 0.52	72.17 ± 1.29	76.82 ± 1.78	88.88 ± 1.19	85.76 ± 2.79	$-$
FWHM	13.4 ± 0.6	12.1 ± 1.8	16.0 ± 1.9	16.2 ± 4.6	26.9 ± 6.1	8.0 ± 6.4	23.3 ± 5.5	$-$
ν_1	$-$	$-$	$-$	$-$	$-$	464.9 ± 13.4	544.75 ± 12.15	$-$
FWHM	$-$	$-$	$-$	$-$	$-$	138.8 ± 87.7	44.7 ± 19.3	$-$
ν_2	465.5 ± 17.5	665.6 ± 13.4	652.3 ± 17.3	767.6 ± 16.7	854.1 ± 13.5	830.7 ± 12.7	$-$	962.60 ± 7.00
FWHM	178.0 ± 71.9	127.4 ± 39.2	145.1 ± 69.4	127.8 ± 58.1	75.1 ± 42.4	124.1 ± 57.0	$-$	43.4 ± 26.7
ν_b	3.49 ± 0.23	5.20 ± 0.40	5.30 ± 0.41	7.52 ± 0.74	11.20 ± 0.83	12.78 ± 1.09	12.68 ± 0.59	10.66 ± 0.59
α	0.020 ± 0.028	0.017 ± 0.025	0.013 ± 0.034	0.083 ± 0.071	0.290 ± 0.011	0.181 ± 0.026	0.327 ± 0.008	0.366 ± 0.028
β	1.73 ± 0.04	1.64 ± 0.06	1.88 ± 0.09	2.45 ± 0.40	2.17 ± 0.21	1.71 ± 0.10	2.47 ± 0.17	3.16 ± 0.40
χ^2/dof	1.62	1.28	1.03	1.02	1.88	0.91	1.34	1.07

Note. The data were grouped by the HBO frequency (see the text for more details).

In searching for kHz QPO peaks, we analyzed the power-density spectra at high frequencies. A constant with the addition of a Lorenz line was used as the model. We analyzed all individual observations (with a duration up to 3.5×10^3 s) but found no statistically significant QPO peaks (above the 3σ confidence level).

A time analysis of the low-frequency flux variability in Cyg X-2 revealed QPOs at a high confidence level in all the individual observations that corresponded to the HB or NB spectral states. Note that the HBO frequency is one of the main frequencies in most models, including TLM and RPM. The two models (see below) unequivocally establish a correspondence between the three QPO peaks: the HBO, lower, and upper ones. According to this assumption, we grouped all data by the HBO frequency.

To obtain the most accurate model parameters (the angle δ for TLM and the neutron-star mass M_{NS} and angular momentum a in RPM), which are invariants in each of the theories under consideration, it was necessary to calculate the three simultaneously observed main QPO frequencies as accurately as possible. Since there were HBOs in all the preselected data, the problem was to find a double QPO peak at a maximum confidence level in the average spectra.

The two peaks were detected only in the July 2, 1997 observational data for the source, which were analyzed by Wijnands *et al.* (1998). However, the detected QPOs were more significant. In contrast to the method proposed by Wijnands *et al.* (1998), we averaged the power-density spectra over the HBO frequency rather than over the observing time. The confidence levels of the upper and lower peaks proved to be 5.8σ and 3.4σ [4.4σ and 3.4σ in Wijnands *et al.* (1998)], respectively. The remaining July 2, 1997 observations revealed only one (upper) of the two QPO peaks.

In the subsequent search for high-frequency QPOs, we averaged the data (except those for July 2, 1997) in each group. The QPO peaks were detected at a confidence level lower than or equal to $\sim 3\sigma$. Assuming that each average spectrum could also contain the power-density spectra without any QPO peaks and representing the Poissonian noise alone, we sequentially sampled individual observations. To this end, the peak significance was calculated twice: we determined the detection confidence level for all data and without one of the individual observations that was excluded from our analysis when the confidence level exceeded an arbitrary threshold. This method was applied to each group. Such an approach is not perfect and has drawbacks. However, those data that definitely contained the Poissonian noise

alone were not included in each group power-density spectrum.

In the average data, we found the kHz QPOs ν_1 and ν_2, as well as the HBOs ν_{HBO} and their harmonics (see Table 1) at low frequencies (<100 Hz). In contrast to individual observations (with a duration up to ~ 3.5 ks) for Cyg X-2, the harmonic at half the frequency of the main QPO peak was found for the first time. It is characterized by an unusually large full width at half maximum (FWHM) of the corresponding Lorenz line ($\nu_{\frac{1}{2}HBO}$ in Table 1). In several cases, the Q factor of some peaks was close to unity.

Figure 1 shows two different power-density spectra for Cyg X-2. Notice the following common property of the QPOs: the frequency increases at all QPO peaks. For comparison, Fig. 1 shows the power-density spectrum of Sco X-1 (taken from Titarchuk *et al.* 1999), the brightest known Z-type source. There are clear similarities between Cyg X-2 and Sco X-1: both sources exhibit kHz QPO peaks, ν_1 and ν_2, in the range $300-1000$ Hz, HBOs and the corresponding harmonics, ν_{HBO}, and a change of the power-law slope in the power-density spectrum at the break frequency ν_b.

3. THEORETICAL MODELS

For our analysis in terms of the two models in question, we used the average spectra and the main frequencies: ν_{HBO}, ν_1, ν_2. The following approximate asymptotic relations between the frequencies are known from the observations of low-mass X-ray binaries (Stella *et al.* 1999): (1) $\Delta\nu = \nu_2 - \nu_1 \propto \nu_2^2$; and (2) $\nu_{HBO} \propto \nu_1$. These observed peculiarities are consistent with each of the theories under consideration.

3.1. The Transition-Layer Model (TLM)

We consider the motion of a clump of matter, the QPO source on the accretion-disk surface, in a Keplerian orbit around a neutron star (NS) in terms of this model. The magnetospheric axis is assumed to be not aligned with the normal to the disk surface but make an angle δ. After multiple passages through a slightly tilted magnetosphere, the clump comes under the effect of Coriolis forces. These forces cause the main Keplerian oscillation frequency, ν_K, to split up into two oscillation modes: radial (ν_h) and perpendicular to the disk plane (ν_L). Both modes are the solution of the equation for the rotation of a body in a noninertial frame of reference [see Osherovich and Titarchuk (1999) for more details on its derivation and solution]. In this model, the lower and upper kHz QPO peaks correspond to the Keplerian ($\nu_K \equiv \nu_1$)
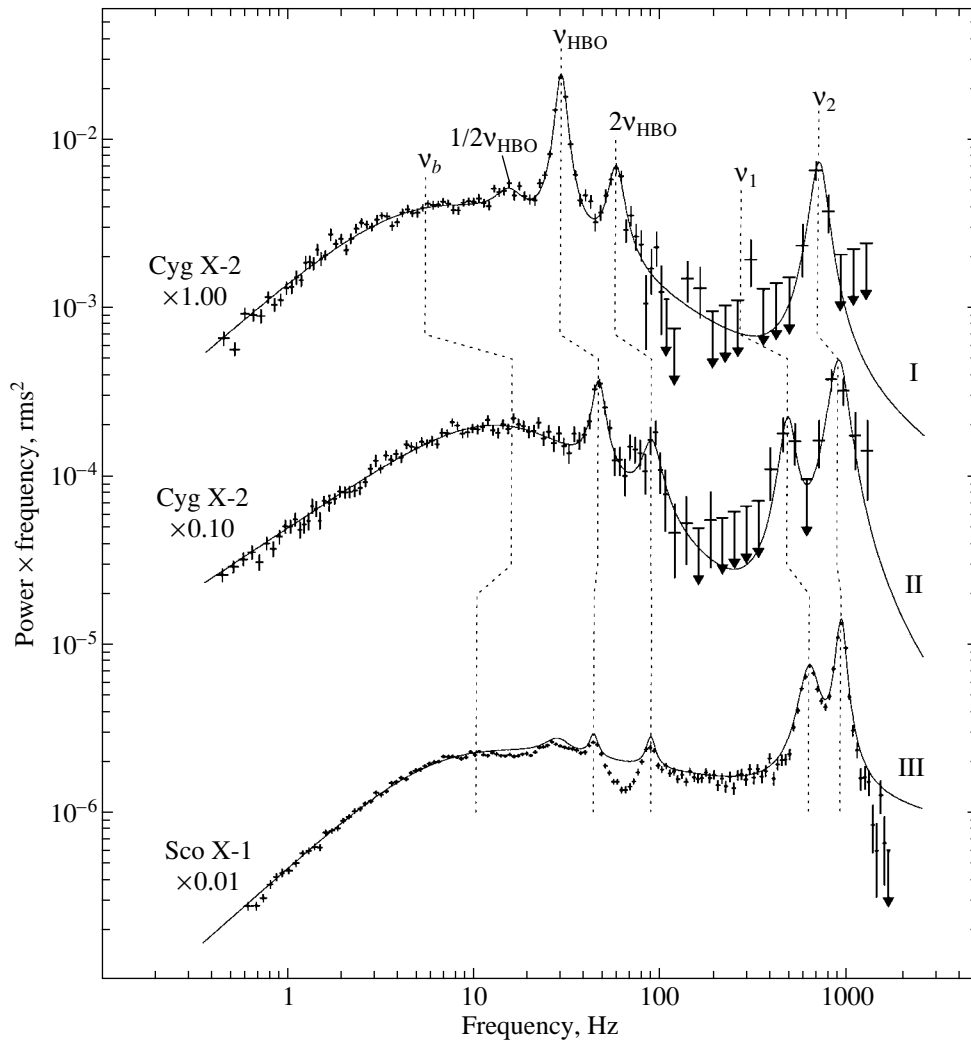
Fig. 1. Power-density spectra for the Z-type sources Cyg X-2 (I, II) and Sco X-1 (III) in units of $F \times P(F)$, $(rms/mean)^2$. The break frequency (ν_b), HBOs and their harmonics (ν_{HBO}), and the lower (ν_1) and upper (ν_2) kHz QPOs are marked. Similar features in the power-density spectra are indicated by the dotted lines. A theoretical lower QPO peak is shown for the upper power-density spectrum. The upper limits correspond to a 1σ confidence level. For clarity, the power-density spectra are shown on different scales along the Y axis; the corresponding coefficients are given. The power-density spectrum for Sco X-1 was taken from Titarchuk $et\ al.$ (1999).

and hybrid ($\nu_h \equiv \nu_2$) frequencies, respectively. The relation between the kHz QPO peaks is given by

$$\nu_h = [\nu_K^2 + (\Omega/\pi)^2]^{1/2}, \qquad (2)$$

where Ω is the rotation frequency of the magnetosphere. The oscillation mode perpendicular to the disk plane is defined as

$$\nu_L = (\Omega/\pi)(\nu_K/\nu_h)\sin\delta. \qquad (3)$$

To a first approximation, the angular velocity of the magnetosphere Ω is constant. A more accurate equation that describes the dependence of Ω on radius can be derived in the multipole magnetic-field approximation (see Osherovich $et\ al.$ 1984). Assuming the contribution of the quadrupole component to the magnetic-field strength in the equatorial plane to be

negligible and taking into account the dipole and octupole components, the final equation for the angular velocity can be reduced to the form (Osherovich and Titarchuk 1999)

$$\Omega/2\pi = C_0 + C_1\nu_K^{4/3} + C_2\nu_K^{8/3} + C_3\nu_K^4, \qquad (4)$$

with $C_2 = -2(C_1C_3)^{1/2}$.

To reconstruct the magnetospheric profile for Cyg X-2 according to Eq. (2) requires at least four pairs of frequencies ν_K and ν_h. Unfortunately, only in one of the eight average power-density spectra have we detected a double QPO peak (see Table 1). In the remaining cases, only the frequencies of one of these are known. Using Eqs. (2) and (3), the magnitude of the second peak can be calculated analytically.
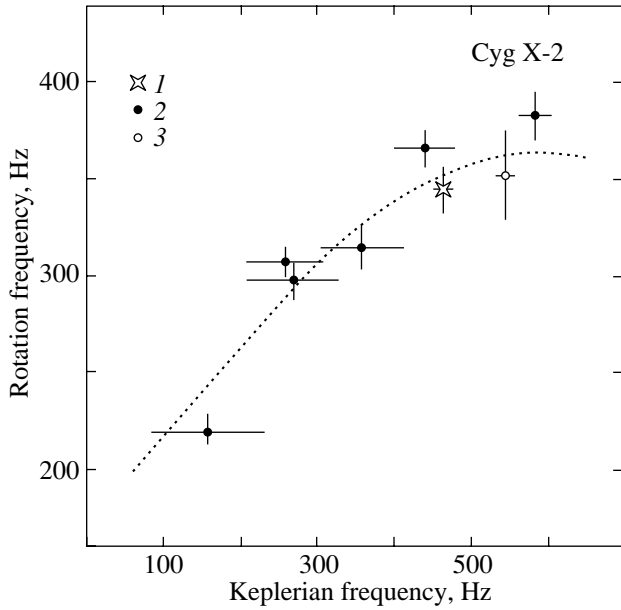
Fig. 2. Rotation frequency of the magnetosphere in TLM, in units of $\Omega/2\pi$, versus Keplerian frequency ($\nu_K = \nu_1$). The data were averaged over the HBO frequency; $1-3$—the data in which one or both kHz QPO peaks were detected, 2—the upper QPO peak (ν_h) is indicated by circles, 3—the lower QPO peak.

Since the angle δ is an invariant in TLM and can be determined, only two unknown parameters appear in Eqs. (2) and (3). The inferred main frequencies ν_L, ν_K, ν_h, which are more accurate than those in Wijnands *et al.* (1998), allowed the tilt angle to be calculated with a smaller uncertainty. Thus, rewriting Eq. (3), we derive an expression for the sought-for angle:

$$\delta = \arcsin[(\nu_h^2 - \nu_K^2)^{-1/2}(\nu_L \nu_h/\nu_K)]; \qquad (5)$$

substituting the values from Table 1 yields $\delta = 6°66 \pm 0°13$. Equations (2) and (3) at fixed ν_h reduce to a quadratic equation whose roots are the angular velocity of the magnetosphere and the Keplerian oscillation frequency:

$$\Omega/\pi, \nu_K = \frac{\nu_h}{\sqrt{2}}\left[1 \pm \left(1 - \left(\frac{2\nu_L}{\nu_h \sin \delta}\right)^2\right)^{1/2}\right]^{1/2}. \qquad (6)$$

At fixed ν_K, the hybrid frequency can be defined as

$$\nu_h = \nu_K \left[1 - \left(\frac{\nu_L}{\nu_K \sin \delta}\right)^2\right]^{-1}. \qquad (7)$$

Thus, for each of the eight average power-density spectra, we obtained Ω/π and ν_K, which are required to reconstruct the magnetospheric profile according to Eq. (4). A plot of angular velocity against Keplerian frequency is shown in Fig. 2. Note that the error

in ν_K exceeds the error in Ω/π. Thus, the problem of determining the best-fit parameters becomes two-dimensional and particularly complex when the fitting function (in our case, Ω as a function of ν_K) is nonlinear. We sought C_i ($C_0, \ldots, C_3$) in Eq. (4) with the Monte Carlo method. Instead of one initial series of data (composed of eight $\nu_K, \Omega/2\pi, \sigma_{\Omega/2\pi}$; see Fig. 2), we generated 1000 series. In each of these series, all angular frequencies $\Omega/2\pi$ and the corresponding errors $\sigma_{\Omega/2\pi}$ were preserved, while ν_K were modeled by a Gaussian distribution with allowance for the mean and error of ν_K. We fitted each series of points by assuming (4) and averaged the derived C_i. Thus, we were able to calculate the best-fit parameters by taking into account the errors in $\Omega/2\pi$ and ν_K. Figure 2 shows the magnetospheric profile with the following parameters: $C_0 = 180$ Hz, $C_1 = 8.35 \times 10^{-2}$ Hz$^{-1/3}$, $C_3 = 3.81 \times 10^{-10}$ Hz^{-3}, $C_2 = -1.13 \times 10^{-5}$ Hz$^{-5/3}$.

The inferred relationship between the Keplerian frequency and the presumed angular velocity of the magnetosphere together with Eqs. (2) and (3) allows a correspondence between the three main frequencies (ν_L, ν_K, ν_h) to be unequivocally established if only one of them is known. This makes it possible to determine the corresponding values of ν_K and ν_h for the individual observations of Cyg X-2 in which no kHz QPOs were detected. Figure 3 shows the classification of QPOs and all the observed and model frequencies. For individual observations (Fig. 3b), the QPOs were calculated with ν_L. The theoretically predicted QPO peaks lie within the frequency range typical of their detection (van der Klis 1999).

3.2. The Relativistic Precession Model (RPM)

The high-velocity motion of matter in a strong gravitational field can generate oscillations attributable to general-relativity effects. The relativistic precession model (Morsink *et al.* 1998) considers the motion of a point mass around a gravitating center. A sufficient condition for oscillations to emerge is that the orbit lay not exactly in the equatorial plane of the compact object but was inclined at an infinitesimal angle. For a nonrotating gravitating center (i.e., in the Schwarzschild approximation), the expression for the particle angular velocity matches the classical formula for Keplerian motion. However, for a neutron star or a black hole with an intrinsic angular momentum, the azimuthal frequency can be expressed (Bardeen *et al.* 1972; Stella *et al.* 1999) in a system of units with $G = 1$ and $c = 1$ as

$$\nu_\phi = \sqrt{\frac{M}{r^3}}\left[2\pi\left(1 + a\sqrt{\frac{M}{r^3}}\right)\right]^{-1}. \qquad (8)$$

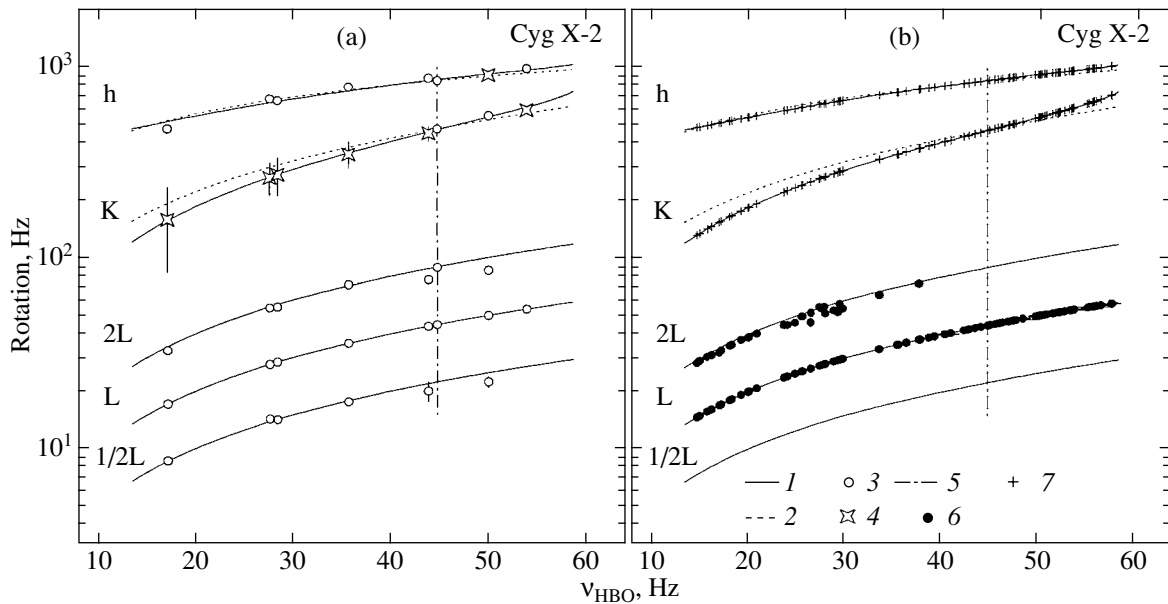**Fig. 3.** The classification of QPOs in the Z-type source Cyg X-2. *1*—TLM, *2*—RPM; (a) the data were averaged over the frequency of the HBO peak for each individual observation ∼1−3.5 ks in duration [see panel (b)]; *3*—observed frequencies, *4*—frequencies predicted by the model. The QPO frequencies along line *5* were used to determine the angle δ (see the text for more details). (b) Individual observations; *6*—detectable frequencies, *7*—the corresponding model frequencies.

Below, we consider only the corotation of a compact object and a test particle: $\nu_\phi > 0, a > 0$ (a is the relative angular momentum). The epicyclic frequency ν_r together with the azimuthal frequency ν_ϕ determine the orbital periastron rotation, $\nu_{per} \equiv \nu_\phi - \nu_r$, while the frequency in the direction perpendicular to the disk plane ν_θ determines the nodal precession, $\nu_{nod} \equiv |\nu_\phi - \nu_\theta|$. The corresponding equations were derived by Okazaki *et al.* (1987) and Kato (1990)

$$\nu_r = \nu_\phi \left[1 - 6\frac{M}{r} + 8a\sqrt{\frac{M}{r^3}} - 3\frac{a^2}{r^2} \right]^{1/2}, \quad (9)$$

$$\nu_\theta = \nu_\phi \left[1 - 4a\sqrt{\frac{M}{r^3}} + 3\frac{a^2}{r^2} \right]^{1/2}. \quad (10)$$

In contrast to TLM, the Keplerian rotation frequency in RPM corresponds to the upper QPO peak, $\nu_2 = \nu_\phi$, while the observed periastron precession frequency corresponds to the lower QPO peak, $\nu_1 = \nu_{per} \equiv \nu_\phi - \nu_r$. In the Kerr approximation, $\nu_\phi \neq \nu_\theta$ (for the Schwarzschild case with $a = 0$, the frequencies are equal: $\nu_\phi = \nu_\theta$), the HBOs are identified with nodal precession: $\nu_{nod} \equiv |\nu_\phi - \nu_\theta|$. Some authors (Stella *et al.* 1999) believe that ν_{HBO} is an even harmonic of ν_{nod}. In contrast to $\nu_{HBO} = \nu_{nod}$, this relation causes the mass of the compact source in Eqs. (8)−(10) required by the RPM to decrease.

In the RPM approximation under consideration, the neutron-star mass and relative angular momen-

tum are invariants and do not depend on the Keplerian frequency. This allows us to determine M_{NS} and a using Eqs. (8)−(10) from the three observed main frequencies (see Table 1) and to use them for the subsequent calculations. Table 2 gives the mass and Keplerian orbital radius. Apart from the main relation in question, which assumes $\nu_{HBO} = \nu_{nod}$, we also obtained M_{NS} and r in the Schwarzschild case by assuming that the HBOs are an even harmonic of the nodal precession.

For the average power-density spectra with known values of only one of the two QPO peaks, the frequency of the second peak can be calculated from Eqs. (8) and (9). It should be noted that, irrespective of which M_{NS} and a are used for a rotating neutron

Table 2. The neutron-star mass and Keplerian orbital radius

Condition	$M_{NS}, M_\odot$	r, km
$\nu_{nod} = \nu_{HBO}$	2.69 ± 0.10	23.12 ± 0.49
$\nu_{nod} = \frac{1}{2}\nu_{HBO}$	2.29 ± 0.09	22.13 ± 0.48
$\nu_{nod} = 0$	1.91 ± 0.08	21.05 ± 0.47

Note. The neutron-star mass and the Keplerian orbital radius determined by RPM in the Kerr ($a > 0, \nu_{nod} \neq 0, \nu_\phi \neq \nu_\theta$) and Schwarzschild ($a = 0, \nu_{nod} = 0, \nu_\phi = \nu_\theta$) approximations. For our calculations, we used the data from column 6 of Table 1, which correspond to the three simultaneously observed frequencies (ν_{HBO}, ν_1, ν_2) in the power-density spectrum of the source.
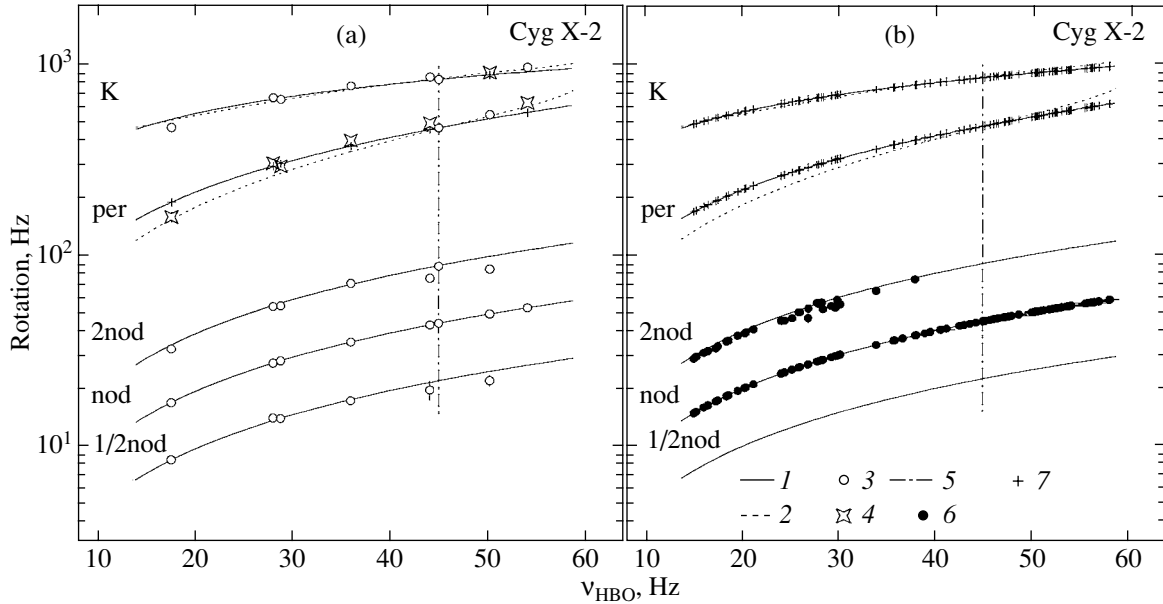
Fig. 4. The classification of QPOs in the Z-type source Cyg X-2. In contrast to Fig. 3, here, *1*—RPM; *2*—TLM; (a) the data were averaged over the frequency of the HBO peak [see panel (b)]. The QPO frequencies along line *5* were used to determine the neutron-star mass M_{NS} and angular momentum *a*; *3*—observed QPO frequencies. The inferred mass and angular momentum were used to calculate the kHz QPO frequencies: *4*—frequencies determined by periastron precession (using ν_ϕ, ν_r), *7*—frequencies determined by nodal precession (using ν_ϕ, ν_θ). (b) Individual observations; *6*—detectable frequencies, *7*—the corresponding model frequencies (crosses).

star ($\nu_{HBO} = \nu_{nod}$ or $\nu_{HBO} = 2\nu_{nod}$), the frequency difference between the model QPOs did not exceed 0.5%. The individual observations in which the HBOs alone were detected revealed both kHz QPO peaks. The results are shown in Fig. 4.

The theoretical profile of epicyclic frequency ν_r is shown in Fig. 5. In RPM, its value is identically equal to the difference between the QPO peaks. In contrast to RPM, here, we simultaneously have two invariants at our disposal, the mass and angular momentum. These invariants allow the self-consistency of the model to be evaluated. The third frequency, which was not found in the observations, can be determined from the other two both from (8) and (9) and from (8) and (10). Figure 5 shows the two variants: $\Delta\nu$ was calculated as a function of ν_1 or ν_2 and with allowance for ν_{HBO} alone.

The relativistic precession model makes it possible to estimate the mass of a compact object and to determine the Keplerian orbital radius. For comparison, Fig. 6 shows the mass–radius relation for various states of neutron stars taken from Miller *et al.* (1998).

The inferred NS mass allows the distance to the binary to be estimated. Smale (1998) obtained such an estimate by analyzing the detected X-ray burst from the source. Assuming that the luminosity reaches the Eddington limit and that the spectral shape is close to a blackbody one, we can derive the

temperature and the relation between the neutron-star mass and the expanding-shell radius. For $M_{NS} = 1.9M_\odot$ (the mass matches that predicted by RPM for a nonrotating NS), the distance is ~ 11.6 kpc (Smale 1998). Assuming that $M_{NS} = 2.69M_\odot$, $M_{NS} = 2.29M_\odot$ ($\nu_{HBO} = \nu_{nod}$ and $\nu_{HBO} = 2\nu_{nod}$), the distance to the source is ~ 13.8 and ~ 12.7 kpc, respectively. The previous distance estimates for Cyg X-2 are based on optical observations: the data of Cowley *et al.* (1979) differ from the above results, $d = 8.7^{+2.2}_{-1.8}$, by $\sim 30-60\%$.

4. DISCUSSION AND RESULTS

The use of our new method for averaging the power-density spectra of various observations in searching for kHz oscillations of the X-ray flux from Cyg X-2 proved to be successful. At least one of the two QPO peaks in each of the eight power-density spectra was reliably detected. Figure 1 shows characteristic features of the source's flux variability. The assumption of a relationship between the three main QPO peaks was correct. Figure 1 shows the spectra with $\nu_{HBO} \approx 28$ Hz (I) and $\nu_{HBO} \approx 45$ Hz (II). The second spectrum exhibits a clear increase in the frequencies of all the observed peaks, both the HBOs together with the second harmonic and the kHz QPOs. Although the confidence level of
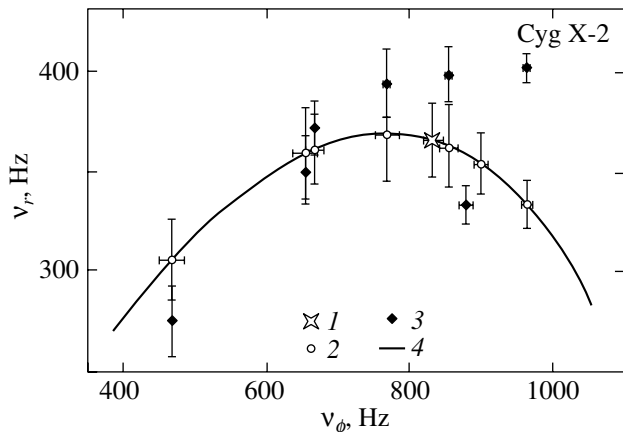
Fig. 5. Relationship between the epicyclic ($\nu_r \equiv \Delta\nu = \nu_2 - \nu_1$) and Keplerian ($\nu_\phi \equiv \nu_2$) frequencies in RPM: *1*—the data in which both kHz QPO peaks were detected. The theoretical values of the second kHz QPO peak were determined by two methods: *2*—by periastron precession, *3*—by nodal precession (see Fig. 4a); *4*—Epicyclic frequency versus Keplerian frequency in the Kerr approximation.
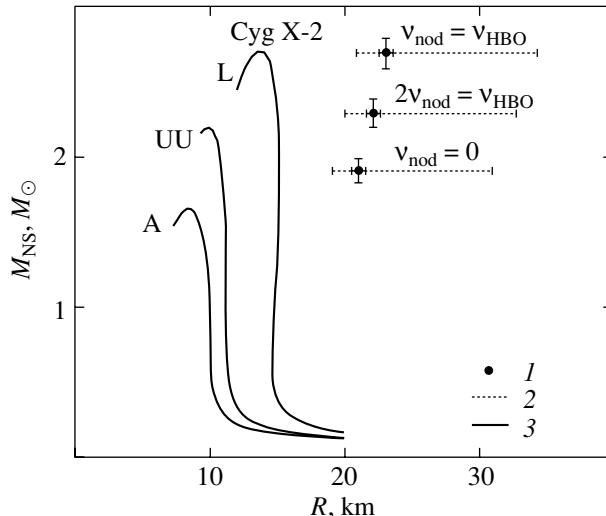

Fig. 6. Relationship of the neutron-star mass to the nodal precession frequency and Keplerian orbital radius: *1* corresponds to the mass and radius for a neutron star with ($a > 0$) and without ($a = 0, \nu_\theta = \nu_\phi$) angular momentum; *2*—Keplerian radii of the observed kHz QPOs; *3*—the mass−radius relation for several equations of state for neutron stars (taken from Miller *et al.* 1998).

the lower QPO peak in spectrum I of Fig. 1 turned out to be below 3σ, its position (the characteristic rise in the figure) in the power-density spectrum corresponds to the observed tendency. By using our new method, we found yet another QPO peak with a frequency close to $1/2$ of ν_{HBO}. Figure 1 shows its position in the spectrum, while Figs. 3 and 4 show its position according to the general classification (see also Table 1). The harmonic at half the frequency of the main HBO peak has been recently found in the observations of other Z-type sources (e.g., GX17+2; Homan *et al.* 2001). The presence of its peak in the power-density spectra is probably a common peculiarity of all Z-type sources.

The theoretical models under consideration yielded acceptable results. Moreover, in Fig. 4, some of the QPO peaks (*4*) obtained in terms of the relativistic precession model virtually coincide with the theoretical curve for the transition-layer model (*2*). This may be a result of the inconsistency of the RPM itself, for which Fig. 5 shows two possible values of $\Delta\nu$ at fixed NS mass and angular momentum [Eqs. (8)−(10)]. The frequency of the second peak can be determined by using the equation for the periastron precession frequency ν_{per} (with ν_1 or ν_2) and the expression for the nodal precession frequency ν_{nod} (with ν_{HBO}). This inconsistency may result from the model simplification, in which the orbital inclination of a test particle is assumed to be infinitesimal. Sibgatullin (2001) provides an exact solution with an arbitrary angle. It turns out that in this treatment, the frequency ν_{HBO} at fixed mass and angular momentum can change

by a factor of ~ 3 when the angle changes from 0 to $\pi/2$ (for the marginally stable orbit at $M_{NS} = 2M_\odot$ and $\nu_\phi = 1200$ Hz). This dispenses with the need to assume the nodal precession frequency ν_{nod} to be equal to $1/2$ of ν_{HBO} to obtain more acceptable NS masses.

The two theoretical models assume the existence of invariants. The invariants in TLM and RPM are, respectively, the tilt angle of the magnetosphere to the disk normal δ and, in the Kerr approximation, the NS mass M_{NS} and angular momentum a. Since the RPM disregards the intrinsic quadrupole moment of the compact object and its oblateness (which can contribute to the nodal precession frequency at a $\sim 10-15\%$ level), we were able to avoid including various theoretical NS equations of state in our analysis. However, it was of interest to compare our results with the constraints imposed by the equations of state. Figure 6 shows some of these taken from Miller *et al.* (1998). The curves correspond to the mass−radius relation for nonrotating neutron stars. Although the rotation velocity for Cyg X-2 is nonzero, the correction for the spin ($\nu_s \approx 200-400$ Hz) may be ignored. Note that only L suggests the possible existence of a massive NS (in our case, $\sim 2.7 M_\odot$) and agrees with the derived M_{NS} in all three cases. The other two equations of state (A and UU) are incompatible with the RPM results in the Kerr approximation (with NS rotation) under consideration. Future observations of Cyg X-2 may probably shed

light on which of the two models in question could predict the frequencies of quasi-periodic oscillations of the X-ray flux from the source more accurately.

ACKNOWLEDGMENTS

REFERENCES

1. J. M. Berdeen, W. H. Press, and S. A. Teukolski, Astrophys. J. **178**, 374 (1972).
2. H. Bradt, R. Rotschild, and J. Swank, Astron. Astrophys., Suppl. Ser. **97**, 335 (1993).
3. A. P. Cowley, D. Crampton, and J. B. Hutchings, Astrophys. J. **231**, 539 (1979).
4. T. Di Salvo, M. Mendez, M. van der Klis, *et al.*, Astrophys. J. **546**, 1107 (2001).
5. G. Hasinger and M. van der Klis, Astron. Astrophys. **225**, 79 (1989).
6. J. Homan, M. van der Klis, P. Jonker, *et al.*, submitted to Astrophys. J.; astro-ph/0104323 (2001).
7. K. Jahoda, J. Swank, A. Giles, *et al.*, Proc. SPIE **2808**, 59 (1996).
8. S. Kato, Publ. Astron. Soc. Jpn. **42**, 99 (1990).
9. L. Titarchuk, V. Osherovich, and S. Kuznetsov, Astrophys. J. Lett. **525**, L129 (1999).
10. M. van der Klis, Annu. Rev. Astron. Astrophys. **38**, 717 (2000).
11. M. van der Klis, in *Timing Neutron Stars,* Ed. by H. Ögelman and E. P. J. van der Heuvel (Kluwer, Dordrecht, 1989), NATO ASI Ser., Vol. 360, p. 27.
12. E. Kuulkers, M. van der Klis, and B. A. Vaughan, Astron. Astrophys. **311**, 197 (1996).
13. M. Mendez, M. van der Klis, J. van Paradijs, *et al.*, Astrophys. J. Lett. **494**, L65 (1998).
14. M. C. Miller, F. K. Lamb, and D. Psaltis, Astrophys. J. **508**, 791 (1998).
15. S. Morsink and L. Stella, Astrophys. J. **513**, 827 (1999).
16. T. Okazaki, S. Kato, and J. Fukue, Publ. Astron. Soc. Jpn. **39**, 457 (1987).
17. V. Osherivich and L. Titarchuk, Astrophys. J. Lett. **522**, L113 (1999).
18. V. Osherovich, I. Tzur, and E. Gliner, Astrophys. J. **284**, 412 (1984).
19. N. R. Sibgatullin, Pis'ma Astron. Zh. **27**, 929 (2001) [Astron. Lett. **27**, 799 (2001)].
20. A. Smale, Astrophys. J. Lett. **498**, L141 (1998).
21. G. Stella, M. Vietry, and S. M. Morsink, Astrophys. J. Lett. **524**, L63 (1999).
22. A. Vikhlinin, E. Churazov, and M. Gilfanov, Astron. Astrophys. **287**, 73 (1994).
23. R. Wijnands, J. Homan, M. van der Klis, *et al.*, Astrophys. J. Lett. **493**, L87 (1998).

Translated by V. Astakhov

Nodal and Periastron Precession of Inclined Orbits in the Field of a Rapidly Rotating Neutron Star

N. R. Sibgatullin[1,2,*]

[1]Moscow State University, Vorob'evy gory, Moscow, 119899 Russia
[2]Max-Planck-Institut für Astrophysik, Karl Schwarzschild Strasse 1, 86740 Garching bei München, Germany
Received August 20, 2001

Abstract—We derive a formula for the nodal precession frequency and the Keplerian period of a particle at an arbitrary orbital inclination (with a minimum latitudinal angle reached at the orbit) in the post-Newtonian approximation in the external field of an oblate rotating neutron star (NS). We also derive formulas for the nodal precession and periastron rotation frequencies of slightly inclined low-eccentricity orbits in the field of a rapidly rotating NS in the form of asymptotic expansions whose first terms are given by the Okazaki–Kato formulas. The NS gravitational field is described by the exact solution of the Einstein equation that includes the NS quadrupole moment induced by rapid rotation. Convenient asymptotic formulas are given for the metric coefficients of the corresponding space–time in the form of Kerr metric perturbations in Boyer–Lindquist coordinates. © 2002 MAIK "Nauka/Interperiodica".

Key words: *neutron stars, luminosity, disk accretion, X-ray radiation*

INTRODUCTION

The X-ray flux from low-mass X-ray binaries (LMXBs) commonly exhibits two peaks in the power spectrum at frequencies ∼1 kHz and one peak in the range 10–100 Hz (van der Klis 2000). Stella and Vietri (1998) proposed to interpret the frequency difference between the kHz peaks as the periastron rotation frequency of low-eccentricity orbits: the observed decrease in this difference for some LMXBs was explained by a radiating clump approaching the marginally stable orbit at which the periastron rotation frequency becomes zero. The low-frequency peak was interpreted as the precession frequency of circular Keplerian orbits inclined to the equator (Merloni *et al.* 1999; Morsink and Stella 1999; Stella and Vietri 1998; Stella *et al.* 1999; Stella 2000; Psaltis *et al.* 1999). The formulas of Okazaki *et al.* (1987) derived in terms of the Kerr solution for orbits slightly inclined to the equatorial plane are commonly used to compare models with observations. The importance of the precession of inclined orbits in the fields of rotating black holes in interpreting the quasi-periodic oscillations (QPOs) of the X-ray flux from pulsars and black-hole candidates was first pointed out by Cui *et al.* (1998). Inclined orbits in Kerr and Kerr–Newman fields were first considered by Wilkins (1972) (uncharged case) and Johnston and Ruffini (1974) (for a charged rotating black hole).

Van Kerkwijk *et al.* (1998) explained the puzzling spindown and spinup of some X-ray pulsars by the fact that the accretion-disk tilt to the equatorial plane in inner regions can become larger than 90°! Previously (Sibgatullin 2001), we derived analytic expressions for the nodal precession and periastron rotation frequencies for orbits *arbitrarily inclined* to the equatorial plane.[1] The nodal precession of the *marginally stable orbits* was described as a function of the corresponding Keplerian frequency for various inclinations of these orbits. For a Keplerian frequency of 1200 Hz and an NS mass of 2.2 $M_\odot$, the nodal frequency in the marginally stable orbit was shown to change from 41 Hz to 123 Hz as the inclination to the equator changes from 0 to 90°, i.e., by a factor of 3!

However, the results for black holes need to be significantly corrected for neutron stars, because a rapidly rotating NS becomes oblate and a quadrupole moment appears. For orbits with low inclinations to the equatorial plane, Markovic (2000) derived formulas for the nodal and periastron precession frequencies in the post-Newtonian approximation by taking into account the NS quadrupole moment. Morsink and Stella (1999) *numerically* calculated ν_r and $\nu_{\rm nod}$ as functions of ν_ϕ for low inclinations and low eccentricities for various NS equations of state.

---

*E-mail: `sibgat@mech.math.msu.su`

[1]To be more precise, with an arbitrary minimum angle θ, which can be reached in a bound trajectory.

Here, our goal is to derive *analytic* formulas for ν_r and $\nu_{\rm nod}$ for *low* inclinations and low eccentricities in the form of asymptotic expansions, which transform to the formulas of Okazaki *et al.* (1987) and Kato (1990) at a zero quadrupole moment. The exact quadrupole solution extracted from the more general solution found by Man'ko *et al.* (1994) formed the basis for our study. This solution was reduced to the simplest form in Weyl coordinates. For clarity, the exact quadrupole solution is also given asymptotically as a Kerr metric perturbation in Boyer–Lindquist coordinates.

Sibgatullin and Sunyaev (1998, 2000a, 2000b) (below referred to as SS 98, SS 00a, and SS 00b) provided formulas for the luminosity and spindown rate for various NS equations of state. These authors proposed a method of analytically constructing the quadrupole moment b as a function of the Kerr parameter j and NS rest mass m, $b = b(j,m)$, based on the main NS thermodynamic function — its gravitational mass M as a function of the Kerr parameter and rest mass $M = M(j,m)$. In this case, the space–time geometry for the exact quadrupole solution plays a crucial role in finding the marginally stable orbit. The dependence $b(j,m)$ was constructed using numerical data from Cook *et al.* (1994) and the numerical code by Stergioulas (1998) for the marginally stable orbit. Laarakkers and Poisson (1998) found a parabolic dependence of the quadrupole moment on the Kerr parameter at $j \ll 1$ by using direct calculations from the formula of Ryan (1995, 1997) for several equations of state. The physical parameters of the marginally stable orbit were studied by Shibata and Sasaki (1998) using expansions at large radii.

An important outstanding question (which is not considered here) is the passage from a viscous accretion disk (Shakura and Sunyaev 1973, 1976) to free particles near the marginally stable orbit. Another complicated question is the behavior of bound trajectories at the marginally stable orbit for their finite inclination to the equatorial plane.

THE EXTERNAL GRAVITATIONAL FIELDS OF ROTATING NEUTRON STARS

The efficiency of the exact quadrupole solution in describing the external fields of rapidly rotating neutron stars with masses larger than $1\,M_\odot$ was demonstrated in SS 98, SS 00a, and SS 00b. In contrast to the Kerr solution, this solution contains an additional constant, which has the meaning of an intrinsic (non-Kerr) NS quadrupole moment, and is symmetric relative to the equatorial plane. The solution under discussion is contained as a special case in the five-parameter (mass, angular momentum, quadrupole moment, electric charge, and magnetic dipole) solutions obtained by Man'ko *et al.* (1994) using the method developed in our book (Sibgatullin 1984).[2] However, the expressions for the metric coefficients and the 4-potential of the electromagnetic field are cumbersome. To solve problems with disk accretion in the equatorial plane, we used simple expressions for the metric of the quadrupole solution in the equatorial plane (SS 98, SS 00a). Since the importance of the quadrupole solution in describing the fields of rotating NS gravitational fields is beyond question, we give here the corresponding exact solution of the Einstein equations *in the entire space*.[3] Thus, the metric coefficients in the square of the interval in vacuum,[4]

$$ds^2 = -f(dt - \omega d\phi)^2 + \frac{\rho^2}{f}d\phi^2 \qquad (1)$$
$$+ \frac{\exp 2\gamma}{f}(d\rho^2 + dz^2)$$

in the exact quadrupole solution are[5]

$$f = {\rm Re}\left(\frac{A-B}{A+B}\right), \qquad (2)$$
$$f\omega = 2{\rm Re}\left(\frac{j(A-B)+iC}{A+B}\right),$$
$$e^{2\gamma} = \frac{A\bar{A} - B\bar{B}}{16k_+^4 k_-^4 R_+ R_- r_+ r_-}.$$

In formulas (2), we use the following notation
$$A = k_-^2(R_- + r_+)(R_+ + r_-) \qquad (3)$$
$$- k_+^2(R_- - r_-)(R_+ - r_+),$$
$$B = k_+ k_-((k_+ + k_-)(r_+ + r_-)$$
$$+ (k_- - k_+)(R_- + R_+)),$$
$$C = zB + k_+ k_-(k_-(R_+ r_+ - R_- r_-)$$
$$+ k_+(R_+ r_- - R_- r_+) + 2b(R_+ - R_- + r_- - r_+)),$$
$$R_\pm = \sqrt{\rho^2 + (z \pm (k_+ + k_-)/2)^2}(\sqrt{1-j^2} \pm ij), \quad (4)$$
$$r_\pm = \sqrt{\rho^2 + (z \pm (k_+ - k_-)/2)^2}(\sqrt{1-j^2} \pm ij),$$
$$k_- = \sqrt{1 - j^2 - 4b}, \quad k_+ = \sqrt{1-j^2}.$$

[2]For the relationship of this method to the soliton solutions of Kramer and Neugebauer (1980), see Ernst (1994) and Man'ko and Ruiz (1998).

[3]The metric of the exact solutions for the Einstein equations with a finite set of multipole moments is given in general form in SS 00a. The method of constructing exact asymptotic flat solutions for the Einstein–Maxwell equations from the data specified on the symmetry axis was developed in our book (Sibgatullin 1984). The entire problem reduces to solving the only homogeneous singular equation with the Cauchy kernel on a segment with an additional normalization condition.

[4]In Papapetru form.

[5]Here, we use a system of units with $M = c = G = 1$.

The metric coefficient ω becomes zero on the symmetry axis at $|z| > (k_+ + k_-)/2$. We assume that ω on the symmetry axis becomes zero everywhere outside the rotating NS (the condition for the absence of conical points). Solution (2)−(4) was obtained for the Ernst potential on the symmetry axis:

$$\mathbf{E} = \frac{A - B}{A + B}\bigg|_{\rho=0} = \frac{z^2 + (ij - 1)z + b^2}{z^2 + (ij + 1)z + b^2}.$$

Note that $(j(A - B) + iC)/(A + B) = i$ on the symmetry axis.

In the special case where $b = (1 - j^2)/4$, the constant k_- becomes zero. In this case, it is convenient to pass to the coordinates $\rho = \sin\theta \times \sqrt{(r-1)^2 - (1-j^2)/4}$, $z = (r-1)\cos\theta$. Passing to the limit $k_- \to 0$, the metric coefficients in the square of the interval

$$ds^2 = -f(dt - \omega d\phi)^2 + \frac{\rho^2}{f}d\phi^2 \qquad (5)$$

$$+ \frac{g}{f}\left(\frac{dr^2}{(r-1)^2 - (1-j^2)/4} + d\theta^2\right)$$

may be represented as

$$f = \mathrm{Re}\left(\frac{a}{b}\right), \quad f\omega = 2\mathrm{Re}\left(\frac{c}{b}\right), \qquad (6)$$

$$g = \frac{\mathrm{Re}(ab^*)}{4(4(r-1)^2 - (1-j^2)m^2)^3}.$$

Here, the asterisk denotes a complex conjugate and the following notation is used with $m \equiv \cos\theta$:

$$a = -27 - 5j^2 + 18ijm - 2ij^3m - 6ijm^3$$
$$+ 6ij^3m^3 - j^2m^4 + j^4m^4 + 108r + 4j^2r$$
$$- 48ijmr + 4ijm^3r - 4ij^3m^3r - 144r^2$$
$$+ 48ijmr^2 + 80r^3 - 16ijmr^3 - 16r^4,$$
$$b = -3 + 3j^2 + 14ijm + 2ij^3m - 2ijm^3$$
$$+ 2ijm^3 - j^2m^4 + j^4m^4 + 20r - 4j^2r$$
$$- 48ijmr + 4ijm^3r - 4ij^3m^3r - 48r^2$$
$$+ 48ijmr^2 + 48r^3 - 16ijmr^3 - 16r^4,$$
$$c = ij^4m(-1 + 2m^2) - im(-3 + 2r)(-1 + 2r)^3$$
$$- 2ij^2m(-2 + m^2 + 2r) + j(-13 + m^4(1 - 2r)$$
$$+ 46r - 48r^2 + 16r^3) + j^3(3 + 2r + m^4(-1 + 2r)).$$

Let us again turn back to the general exact quadrupole solution (2)−(4) and pass to the Boyer−Lindquist coordinates $\rho = \sin\theta \times \sqrt{(r-1)^2 - (1-j^2)}$, $z = (r-1)\cos\theta$.

Let us represent the square of the interval as

$$ds^2 = -fdt^2 + 2f\omega dt d\phi \qquad (7)$$

$$+ \sin^2\theta\left(\frac{r^2 - 2r + j^2}{f} - f\omega^2\right)d\phi^2$$

$$+ \frac{\Gamma}{f}\left(\frac{dr^2}{r^2 - 2r + j^2} + d\theta^2\right),$$

where

$$f = \frac{F}{r^2 + j^2\cos^2\theta}, \quad \omega = \frac{W}{r^2 + j^2\cos^2\theta}. \qquad (8)$$

We will seek the functions F, Γ, and W using the exact solution (2)−(4) in the form of series in inverse powers of the radius. At $b = 0$, the series for F, Γ, and W break off on the second or third term, giving the exact Kerr solution

$$F_k = \Gamma_k = r^2 - 2r + j^2\cos^2\theta, \quad W_k = -2jr\sin^2\theta.$$

At $b \neq 0$, the series for F, Γ, and W contain an infinite number of terms and diverge on the event horizon. This fact is related to the so-called *no hair theorem*[6] [see Misner *et al.* (1973) and Sibgatullin (1984) for a more detailed discussion of the black-hole theory]. A collapsing star loses its magnetic and quadrupole moment and its field asymptotically approaches the field of a rotating black hole (Ginzburg and Ozernoi 1964; Doroshkevich *et al.* 1965).

Cumbersome transformations (in these formulas, $m \equiv \cos\theta$) yielded

$$F = r^2 - 2r + j^2m^2 + b\left(\frac{3m^2 - 1}{r^2}(r + 1)\right. \qquad (9)$$

$$\frac{1}{r^3}\left(\frac{3}{4}(1 + j^2 + b) - \frac{1}{2}(3 + 25j^2 + 15b)m^2\right.$$

$$\left.\left. + \frac{1}{4}(-5 + 63j^2 + 35b)m^4\right) + 0\left[\frac{1}{r^4}\right]\right);$$

$$\Gamma = r^2 - 2r + j^2m^2 + b(1 - m^2)$$

$$\times \left(\frac{3}{2r^3}(5m^2 - 1)(r + 2) + \frac{1}{4r^4}(-17 - j^2\right.$$

$$+ 8b + 2(35 + 10j^2 + 56b)m^2 + (35$$

$$\left. - 35j^2 - 180b)m^4) + o\left[\frac{1}{r^5}\right]\right);$$

$$W = 2j(1 - m^2)\left(-r + b\left(\frac{1}{4r^3}(5m^2 - 1)\right.\right.$$

$$\times (4r + 7) + \frac{1}{8r^4}(-24 - b + 2(54 + 20j^2 + 63b)m^2$$

$$\left.\left. + (12 - 72j^2 - 189b)m^4) + o\left[\frac{1}{r^5}\right]\right)\right).$$

---

[6]According to Wheeler's figurative expression, "a black hole has no hair." The stability of black holes was shown in the pioneering papers by Reggie-Wheeler and Zerilli.

PERIASTRON AND NODAL PRECESSION OF ORBITS WITH LOW INCLINATIONS TO THE EQUATORIAL PLANE AND WITH LOW ECCENTRICITIES

The eikonal equation $g^{ij}S_{,i}S_{,j} = -1$ in stationary spaces with axial symmetry and with the square of the interval (1) have solutions of the form $S = -Et + L\phi + \tilde{S}(\rho, z)$, where $\tilde{S}$ satisfies the equation

$$(\tilde{S}_{,\rho}^2 + \tilde{S}_{,z}^2)fe^{-2\gamma} = V(\rho, z) \equiv \frac{E^2}{f} \qquad (10)$$

$$- \frac{f}{\rho^2}(L - \omega E)^2 - 1.$$

Consider nearly circular orbits in the equatorial plane. For the latter, $V = V_{,z} = V_{,\rho} = 0$ at $z = 0$. Consequently, expanding the right-hand part of Eq. (10) for perturbations in a Taylor series to within quadratic terms, we have

$$(\tilde{S}_{,\rho}^2 + \tilde{S}_{,z}^2)fe^{-2\gamma} = \frac{1}{2}(V_{,\rho\rho}(\Delta\rho)^2 + V_{,zz}z^2) + \text{const.} \qquad (11)$$

The constant in Eq. (11) is related to the perturbation of V when the constants E and L are perturbed for nonequatorial, noncircular orbits. Equation (11) can be solved by the separation of variables, $\tilde{S} = S_1(\Delta\rho) + S_2(z)$. Consider the Hamiltonian system associated with Eq. (11). We will seek $\Delta\rho$ and z in the form $\Delta\rho = \epsilon_1 \sin\xi$, $z = \epsilon_2 \sin\zeta$. We then obtain

$$\frac{d\zeta}{ds} = \sqrt{-fe^{-2\gamma}V_{zz}/2}, \quad \frac{d\xi}{ds} = \sqrt{-fe^{-2\gamma}V_{\rho\rho}/2}, \qquad (12)$$

$$\frac{d\phi}{ds} = \frac{f}{\rho^2}(L - \omega E), \quad \frac{dt}{ds} = \frac{E}{f} + \frac{f\omega}{\rho^2}(L - \omega E).$$

Note that the right-hand parts of Eqs. (12) are constant.

Let us now make use of the expression for the energy and angular momentum of particles in equatorial circular orbits (SS 98, SS 00a):

$$E = \frac{\sqrt{f}}{\sqrt{1 - f^2p^2/r}}, \quad L - \omega E = pE, \qquad (13)$$

$$p \equiv \rho^2(-\lambda + \sqrt{\lambda^2 + \mu - \mu^2 r})/n,$$

$$\lambda \equiv f\dot{\omega}, \mu \equiv \dot{f}/f, n \equiv f - r\dot{f}.$$

Here, the dot denotes a derivative with respect to ρ^2.

For the frequency of a particle in a Keplerian equatorial circular orbit, the following formula can be derived from Eqs. (13):

$$\omega_\phi = \frac{p}{(\rho^2/f^2 + \omega p)}.$$

Below, it is convenient to introduce a new quantity instead of p: $\tau \equiv \rho^2/(fp)$. The formula for the frequency can then be rewritten as

$$\omega_\phi = \frac{1}{T}, \quad T = 2\pi(\omega + \tau/f), \qquad (14)$$

$$\tau \equiv (\lambda + \sqrt{\lambda^2 + \mu - \mu^2 r})/\mu.$$

For the rotation frequency from periastron to periastron, $2\pi\nu_r = d\xi/dt$, we obtain from Eqs. (12)

$$\nu_r^2 = \nu_\phi^2 M, \qquad (15)$$

where we use the notation

$$M \equiv 2e^{-2\gamma}\left(-gf\left(\frac{1}{f}\right)_{,qq}\tau^2 + \frac{q^3}{f}\left(\frac{f}{q}\right)_{,qq}\right.$$

$$\left. -4q^2\left(\frac{f}{q}\right)_{,q}\tau\omega_{,q} - 2q\tau f\omega_{qq} + 2\tau^2 f^2(\omega_{,q})^2\right)|_{z=0},$$

$q \equiv \rho^2$. In exactly the same way, for the rotation frequency of the maximum rise in z, $2\pi\nu_\theta = d\zeta/dt$, we obtain from Eqs. (12) using the explicit expression (10) for V

$$\nu_\theta^2 = \nu_\phi^2 N, \qquad (16)$$

$$N = \frac{e^{-2\gamma}}{f}(f_{,zz}(\rho^2 + \tau^2) - 2f\omega_{zz}\tau)|_{z=0}.$$

For the periastron and nodal precession frequencies, we have

$$\nu_{\text{per}} = \nu_\phi(1 - \sqrt{M}), \quad \nu_{\text{nod}} = \nu_\phi(1 - \sqrt{N}). \quad (17)$$

We will seek the functions $T(r)$, $N(r)$, and $M(r)$ in coordinates (7) in the form of expansions in terms of inverse powers of r. At $b = 0$, the series break off to give the exact formulas of Okazaki et al. (1987) and Kato (1990) for the Kerr metric

$$M = 1 - \frac{6}{r} + \frac{8j}{r^{3/2}} - \frac{3j^2}{r^2}, \quad N = 1 - \frac{4j}{r^{3/2}} + \frac{3j^2}{r^2},$$

$$T = j + r^{3/2}.$$

Let $b \neq 0$; using coordinates (7), we obtain

$$M = 1 - \frac{6}{r} + \frac{8j}{r^{3/2}} - \frac{3(j^2 + b)}{r^2} + 3b\left(-\frac{5}{r^3}\right. \qquad (18)$$

$$\left. + \frac{8j}{r^{7/2}} - \frac{1}{2r^4}(16 + 7j^2 + 2b) + \frac{12j}{r^{9/2}}\right.$$

$$\left. -\frac{1}{4r^5}(51 + 3j^2 + 31b) + \text{o}\left[\frac{1}{r^{11/2}}\right]\right);$$

$$N = 1 - \frac{4j}{r^{3/2}} + \frac{3(j^2 + b)}{r^2} + 3b\left(\frac{2}{r^3}\right. \qquad (19)$$

$$\left. -\frac{5j}{r^{7/2}} + \frac{1}{2r^4}(8 + 7j^2 + 2b) - \frac{9j}{r^{9/2}} + \text{o}\left[\frac{1}{r^5}\right]\right);$$

$$T/2\pi = r^{3/2} + j + b\left(-\frac{3}{4r^{1/2}} - \frac{5}{4r^{3/2}}\right. \qquad (20)$$

$$+ \frac{3j}{2r^2} - \frac{3}{32r^{5/2}}(10 + 10j^2 + b) + \frac{5j}{r^3}$$

$$- \frac{3}{16r^{7/2}}(29 + 13j^2 + 4b) + o\left[\frac{1}{r^4}\right]\right).$$

Using Eqs. (19) and (20) for the nodal angular velocity of slightly inclined orbits, we derive a Taylor series in inverse powers of the radius:

$$\omega_{\mathrm{nod}} = \frac{2j}{r^3} - \frac{3(b + j^2)}{2r^{7/2}} - \frac{3b}{r^{9/2}} + \frac{3j}{2r^5}(-j^2 + 5b)$$

$$\tag{21}$$

$$- \frac{3}{8r^{11/2}}(16b - 3j^4 + 11j^2 b + 4b^2) + o\left[\frac{1}{r^6}\right].$$

At $b = 0$, we obtain a Taylor expansion of the formula by Okazaki *et al.* (1987) and Kato (1990) from Eq. (21).

For orbits with low inclinations to the equatorial plane, Markovic (2000) derived formulas for the periastron and nodal precession frequencies in the *post-Newtonian approximation*. His formulas for the nodal precession frequency is equivalent to Eq. (21) if the first two terms are retained in it. The latter are the sum of the Newtonian precession of a slightly inclined orbit in a gravitational field with a quadrupole moment and the precession of Lense and Thirring (1918).

Thus, for orbits with low inclinations to the equatorial plane and with low eccentricities, allowance for NS oblateness in Eqs. (17) for the nodal and periastron precession of orbits with rapid rotation gives a *large contribution for the hard equations of state*. The method for constructing the dependence of the quadrupole moment on the NS rest mass and Kerr parameter is described in SS 00a; for the equations of state A and FPS, the specific functions $b(j, m)$ were constructed at rest masses larger than the solar mass and smaller than the critical mass according to the static stability criterion. Laarakkers and Poisson (1998) found an almost quadratic dependence of the quadrupole moment on the Kerr parameter at small j. In SS 98, the dependence $b(j)$ was studied for normal sequences with $1.4M_\odot$ in the static limit and for normal sequences unstable in the static limit *over the entire range of Kerr parameters* in which the equatorial rotation velocity on the stellar surface is lower than the equatorial Keplerian velocity.

NODAL PRECESSION OF ORBITS WITH ARBITRARY INCLINATIONS TO THE EQUATORIAL PLANE IN THE POST-NEWTONIAN APPROXIMATION

Consider the non-Kerr terms in Eqs. (9) as small Kerr metric perturbations: $F = F_k(1 + v)$; $\Gamma = \Gamma_k(1 + z)$; $W = W_k(1 + w)$. The eikonal equation

(10) in Boyer–Lindquist coordinates can be written as

$$(\tilde{S}_{,r}^2 \Delta + \tilde{S}_{,\theta}^2)(1 + v - z) = (E(r^2 + j^2) - L_j)^2/\Delta \tag{22}$$

$$- (L - jE)^2 + \cos^2\theta\left((E^2 - 1)j^2 - \frac{L^2}{\sin^2\theta}\right)$$

$$- v\left(\left(\frac{(r^2 + j^2)^2}{\Delta} - j^2\sin^2\theta\right)E^2 + \frac{L^2}{\sin^2\theta}\right.$$

$$\left. - \frac{L^2 j^2}{\Delta}\right) - \frac{4w(2j^2 r^2 \sin^2\theta + ELjr)}{\Delta}.$$

The asymptotic result for the nodal precession frequency that follows from Eq. (22) can also be obtained as follows.

Consider the energy integral for a particle moving in the gravitational field of a point mass with a quadrupole moment in the Newtonian approximation:

$$\frac{1}{2}\left(r^2\left(\frac{d\theta}{dt}\right)^2 + \frac{L^2}{r\sin^2\theta} + \left(\frac{dr}{dt}\right)^2\right) - \frac{1}{r} \tag{23}$$

$$+ \frac{b}{2r^3}(3\cos^2\theta - 1) = H, \quad H = \mathrm{const}.$$

In the absence of a quadrupole moment for circular orbits, we have

$$H = -1/(2r); \quad p_r = 0; \quad L^2 = r\sin^2 s; \tag{24}$$

$$\cos\theta = \cos s \cos(t/r^{3/2}).$$

We restrict our analysis to the case $b/r^2 \ll 1$ and denote $\tau \equiv t/r^{3/2}$. The energy integral, to within quantities of the second order of smallness in b/r^2, can be written as

$$\left(\frac{d\theta}{d\tau}\right)^2 = \left(1 - \frac{L^2}{r\sin^2\theta}\right)\left(1 - 4\frac{\delta r}{r}\right) \tag{25}$$

$$+ 2r\delta H - \frac{b}{r^2}(3\cos^2\theta - 1).$$

We write the constant H via its value at the turning point $d\theta/d\tau = 0$:

$$1 + rH = \frac{L^2}{2r\sin^2 s} + \frac{b}{2r^2}(3\cos^2 s - 1). \tag{26}$$

With (26), the energy integral (25) takes the form

$$\left(\frac{d\theta}{d\tau}\right)^2 = \frac{\sin^2\theta - \sin^2 s}{\sin^2\theta} \tag{27}$$

$$\times \left(\frac{L^2}{r\sin^2 s} - 4\frac{\delta r}{r} + \frac{3b}{r}\sin^2\theta\right).$$

An analog of circular orbits in a quadrupole field are perturbed orbits with a zero mean deviation $= \delta r$ from a sphere of constant radius:

$$\int \delta r \, d\varphi(t) = 0. \tag{28}$$

In Eq. (28), the integral is taken over the meridional period T_θ in which the particle again returns to the minimum angle s. Given (28), the azimuthal angle ϕ changes in time $T_\theta/4$ by

$$\Delta\phi = \int_s^{\pi/2} \sqrt{\frac{L^2}{r\sin^2 s}} \frac{d\theta}{\sin^2\theta} \left((\cot_s^2 - \cot^2\theta)\right) \quad (29)$$

$$\times \left(\frac{L^2}{r\sin^2 s} + \frac{3b}{r^2}\sin^2\theta\right)\Bigg)^{1/2} \approx \frac{\pi}{2}\left(1 - \frac{3b}{2r^2}\sin s\right).$$

Consequently, the nodal precession because of the NS oblateness (the presence of a quadrupole moment) is

$$\nu_{\rm nod} = -\frac{3}{2r^{7/2}} b\sin s.$$

Combining this result with the formula for the precession frequency of inclined circular orbits in a Kerr field [see Eq. (52) in Sibgatullin (2001)], we **derive the sought-for formula for the nodal precession frequency in the post-Newtonian approximation**:

$$2\pi\nu_{\rm nod} = \frac{2j}{r^3} - \frac{3}{2r^{7/2}}(b + j^2)\sin s. \quad (30)$$

Formula (30) at $s = \pi/2$ transforms to the formula of Markovic (2000). In exactly the same way, for the azimuthal (Keplerian) period at an inclined orbit in the field of an oblate star in the post-Newtonian approximation, we obtain using (28)

$$T = r^{3/2} + j(3\sin s - 2) - \frac{3}{4}\frac{b}{r^{1/2}}(2 - \sin s) \quad (31)$$

$$+ \frac{9}{4r^{1/2}}\cos^2 s(j^2 + b).$$

At $s = -\pi/2$, Eq. (31) matches Eq. (20) in the principal terms.

ACKNOWLEDGMENTS

REFERENCES

1. G. B. Cook, S. L. Shapiro, and S. A. Teukolsky, Astrophys. J. **424**, 823 (1994).
2. W. Cui, S. N. Zhang, and W. Chen, Astrophys. J. Lett. **492**, L53 (1998); astro-ph/9811023.
3. A. G. Doroshkevich, Ya. B. Zel'dovich, and I. D. Novikov, Zh. Éksp. Teor. Fiz. **49**, 170 (1965) [Sov. Phys. JETP **22**, 122 (1966)].
4. F. Ernst, Phys. Rev. D **50**, 4993 (1994).
5. V. L. Ginzburg and L. M. Ozernoi, Zh. Éksp. Teor. Fiz. **47**, 1030 (1964) [Sov. Phys. JETP **20**, 689 (1964)].
6. M. Johnston and R. Ruffini, Phys. Rev. D **10**, 2324 (1974).
7. S. Kato, Publ. Astron. Soc. Jpn. **42**, 99 (1990).
8. M. van der Klis, astro-ph/0001167.
9. M. H. van Kerkwijk, Deepto Chakrabarty, J. E. Pringle, and R. A. M. Wijers, Astrophys. J. Lett. **499**, L27 (1998); astro-ph/9802162.
10. D. Kramer and G. Neugebauer, Phys. Lett. A **75A**, 259 (1980).
11. W. Laarakkers and E. Poisson, Astrophys. J. **512**, 282 (1999); gr-qc/9709033 (1998).
12. J. Lense and H. Thirring, Phys. Z. **19**, 156 (1918).
13. V. S. Man'ko and E. Ruis, Class. Quantum Grav. **15**, 2007 (1998).
14. V. C. Man'ko, N. R. Sibgatullin, *et al.*, Phys. Rev. D **49**, 5144 (1994).
15. D. Markovic, astro-ph/0009450.
16. A. Merloni, M. Vietri, L. Stella, and D. Bini, Mon. Not. R. Astron. Soc. **304**, 155 (1999); astro-ph/9811198.
17. Ch. W. Misner, K. S. Thorne, and J. A. Wheeler, *Gravitation* (Freeman, New York, 1973).
18. Sh. M. Morsink and L. Stella, Astrophys. J. **513**, 827 (1999); astro-ph/9808227.
19. I. D. Novikov and V. P. Frolov, *The Physics of Black Holes* (Nauka, Moscow, 1986).
20. A. T. Okazaki, S. Kato, and J. Fukue, Publ. Astron. Soc. Jpn. **39**, 457 (1987).
21. D. Psaltis, R. Wijnands, J. Homan, *et al.*, Astrophys. J. **520**, 763 (1999); astro-ph/9903105.
22. F. D. Ryan, Phys. Rev. D **52**, 5707 (1995).
23. F. D. Ryan, Phys. Rev. D **55**, 6081 (1997).
24. N. I. Shakura and R. A. Sunyaev, Astron. Astrophys. **24**, 337 (1973).
25. N. I. Shakura and R. A. Sunyaev, Mon. Not. R. Astron. Soc. **175**, 613 (1976).
26. M. Shibata and M. Sasaki, Phys. Rev. D **58**, 10401 (1998).
27. N. R. Sibgatullin, *Oscillation and Waves in Strong Gravitational and Electromagnetic Fields* (Nauka, Moscow, 1984; Springer, Heidelberg, 1991).
28. N. R. Sibgatullin, Pis'ma Astron. Zh. **27**, 929 (2001) [Astron. Lett. **27**, 799 (2001)].
29. N. R. Sibgatullin and R. A. Sunyaev, Pis'ma Astron. Zh. **24**, 894 (1998) [Astron. Lett. **24**, 774 (1998)].
30. N. R. Sibgatullin and R. A. Sunyaev, Pis'ma Astron. Zh. **26**, 813 (2000a) [Astron. Lett. **26**, 699 (2000a)].
31. N. R. Sibgatullin and R. A. Sunyaev, Pis'ma Astron. Zh. **26**, 899 (2000b) [Astron. Lett. **26**, 772 (2000b)].
32. L. Stella, astro-ph/0011395.
33. L. Stella and M. Vietri, Astrophys. J. Lett. **492**, L59 (1998); astro-ph/9709085.
34. L. Stella, M. Vietri, and Sh. M. Morsink, Astrophys. J. Lett. **524**, L63 (1999); astro-ph/9907346.
35. N. Stergioulas, http://pauli.phys.uwm.edu/Code/rns; www.livingre-views.org/Articles/Volume1/1998−8stergio.

Translated by V. Astakhov

An Analysis of the Line Shape for H_2O Maser Emission Peaks in Star-Forming Regions

E. E. Lekht[1,2,*], N. A. Silant'ev[1,3], J. E. Mendoza-Torres[1], and A. M. Tolmachev[4]

[1]*Instituto Nacional de Astrofísica, Óptica y Electrónica,*
Luis Enrique Erro No. 1, Apdo Postal 51 y 216, 72840 Tonantzintla, Puebla, México
[2]*Sternberg Astronomical Institute, Universitetskii pr. 13, Moscow, 119899 Russia*
[3]*Pulkovo Astronomical Observatory, Russian Academy of Sciences,*
Pulkovskoe sh. 65, St. Petersburg, 196140 Russia
[4]*Pushchino Radio Astronomy Observatory, Astrospace Center, Lebedev Physical Institute,*
Russian Academy of Sciences, Pushchino, Moscow oblast, 142292 Russia
Received September 17, 2001

Abstract—We analyze the line shape for emission peaks of H_2O maser sources associated with star-forming regions by using the spectra obtained with the RT-22 radio telescope at the Pushchino Radio Astronomy Observatory. For five sources, we found the line profile of emission peaks to be asymmetric. In all cases, the left (high-frequency) line wing is higher than the right wing. Our analysis of the line shape yielded additional information on the structure and evolution of the maser sources under study. In G43.8−0.1, the emission feature was found to split up into two components. To explain the evolution of the 16.8 km s^{-1} line in NGC 2071, we propose a model in which the line-of-sight velocity gradient changes under the effect of a (non-shock) wave. The observed short-duration flares of individual emission features in W75N can emerge due to a chance projection of the numerous clumps of matter involved in Keplerian motion onto each other. © *2002 MAIK "Nauka/Interperiodica".*

Key words: *radio sources, star formation*

INTRODUCTION

The spectra of H_2O masers have a complex structure and are highly variable in time. Such spectra are attributable to the presence of both regular and turbulent motions with various scales and lifetimes in the source. A long-term monitoring reveals long-lived emission features (spots) and yields the characteristic parameters of the relatively small-scale (<1 AU) turbulence (Lekht *et al.* 1999). In addition, studies of such features provide information on the comparatively regular physical processes both in the spot itself and in the possible amplification corridor along the propagation path of the maser emission (Matveenko *et al.* 2000).

At present, there are several studies aimed at searching for flux and line-FWHM variability of single features and for a correlation between the variations of these parameters. The line shape was first analyzed for an intense flare of the feature at +8 km s^{-1} of the H_2O maser source in Orion in 1979 (Matveenko 1981; Strel'nitskii 1982). The existence of asymmetry was pointed out: the left,

high-frequency wing was higher. The asymmetry in the profile was explained by the possible superposition of two components (Matveenko *et al.* 1980; Matveenko, 1981).

Apart from the natural quantum broadening, the line FWHM is determined by the thermal scatter of velocities of the emitting molecules. In addition, the line can be broadened by small-scale chaotic turbulent motions. In a medium with an inverse level population, the line significantly narrows by a factor of $\sim(\tau + 1)^{1/2}$ (for an unsaturated maser). Here, τ is the optical depth of the amplification path at the line center. In this case, estimates of the mean thermal velocity and the velocity of small-scale turbulent motions depend on τ. Goldreich and Kwan (1974) showed that under certain conditions, the line can also narrow with the same dependence on τ for a saturated maser. The line FWHM and the flux will then be related by

$$\Delta V \propto (\ln F_0)^{-1/2} \qquad (1)$$

for an unsaturated maser and

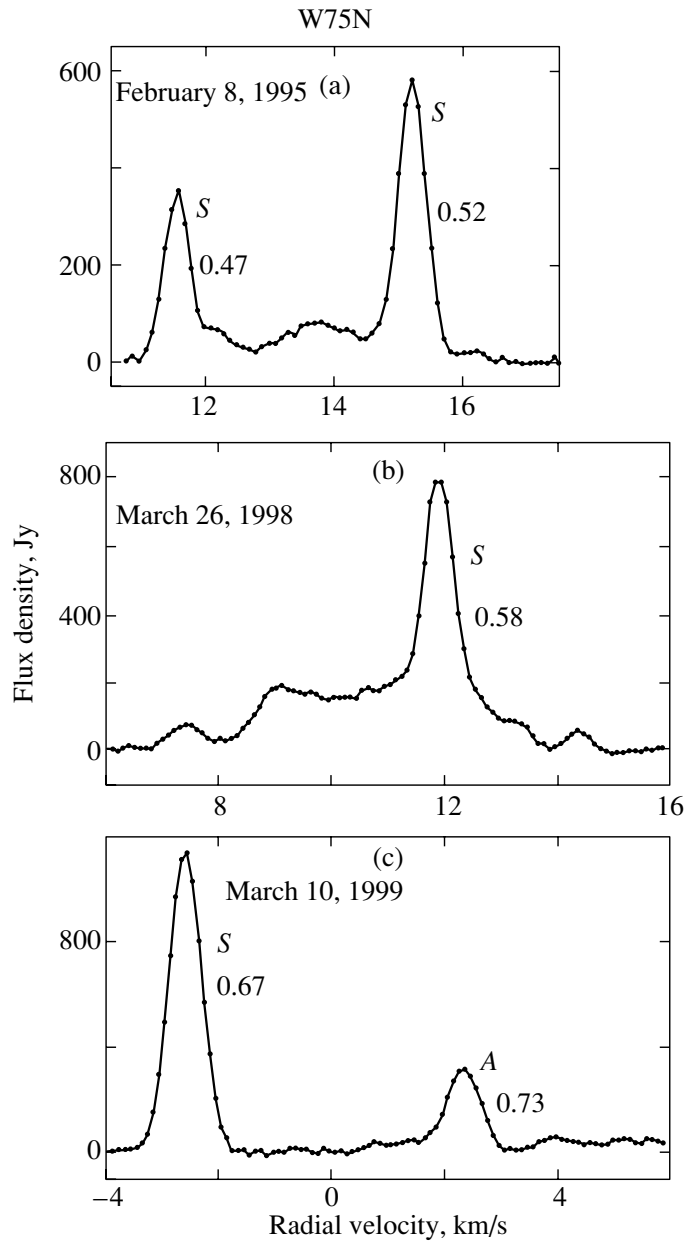$$\Delta V \propto F_0^{-1/2} \qquad (2)$$

W75N

Fig. 1. Three spectra of W75N during flares of individual spectral features. The number denotes the line FWHM, in km s^{-1}.

for a saturated maser (Mattila *et al.* 1985). Here, F_0 is the flux at the line center. The formation of the line profile for various masing modes was considered by Strel'nitskii (1974).

The passage and amplification of the background emission or the spontaneous emission (at $\tau \gg 1$) in a medium at rest and in a rigidly rotating medium (e.g., a rotating homogeneous maser spot) gives a symmetric line at the output of an unsaturated maser. In our case, a Gaussian fit satisfactorily describes the shape of the observed line. For a more complex spot structure, the line can be asymmetric (Matveenko *et al.* 1980, 2000).

Here, we investigate the shapes of the emission lines in some H_2O maser sources. By the line shape, we mean the following: the line FWHM, whether it coincides with or differs from a Gaussian, and the line asymmetry (the difference between the right and left line wings).

DATA PRESENTATION

We analyzed the spectra of the H_2O maser sources NGC 2071, S269, G43.8−0.1, ON1, W75N, and S128, which are associated with star-forming regions. All spectra were obtained with the RT-22

radio telescope at the Pushchino Radio Astronomy Observatory. The spectral resolution at $\lambda = 1.35$ cm was 0.101 km s^{-1}. The radio telescope, equipment, and observing techniques were described in detail, for example, by Sorochenko *et al.* (1985).

We selected individual emission components during flares and long-lived components. The emission peaks during flares are most frequently single. Their blending with other features can be insignificant and can take place mainly in the wings. In addition, it is highly probable that the main characteristics of the single line (flux, radial velocity, line FWHM, and shape) will vary. There may also be a functional relationship between the flux and line-FWHM variations. The H_2O spectra of the long-lived features were taken for the periods when these features were single or weakly blended. We selected lines that were no broader than 0.7 km s^{-1} and lines for which there was a correlation between the flux and FWHM variations. Of course, this did not completely guarantee that the lines were definitely single.

Our selection presents sources of three different types: a Keplerian disk (W75N and S269), an expanding envelope (G43.8−0.1, ON1, and S128), and a jet (NGC 2071). The maser S128 has two groups of spots located at the boundary between interacting (probably colliding) clouds. The maser W75N is also a double source. One of the sources is associated with an ultracompact H II region (VLA 2), while the other is associated with a jet (VLA 1) (Torrelles *et al.* 1997). The RT-22 radio telescope receives the emission from both sources. NGC 2071 has a similar structure (Torrelles *et al.* 1998).

Figure 1 shows the H_2O spectra of the maser W75N when strong emission flares took place. The spectra of this source are rather complex and contain a large number of emission features, which overlap in radial velocity. Nevertheless, the flaring features are fairly strong and may be considered as single features. The letters S and A denote the symmetric and asymmetric lines, respectively.

Figure 2 shows the H_2O spectra of some sources at the epochs of their study here. The arrow in the spectrum of G43.8−0.1 indicates the possible velocity of the central star taken from Lekht and Sorochenko (1999).

Some emission peaks were very narrow. For example, during the 1982 flare in G43.8−0.1, the line FWHM at the flare maximum was a mere 0.35 km s^{-1}. In such cases, the bandwidth of the filter-bank analyzer (0.1 km s^{-1}) was not considerably narrower than the line FWHM. For this reason, the observed lines proved to be slightly distorted; i.e., the fluxes in the line peak were underestimated. Such narrow lines were corrected.
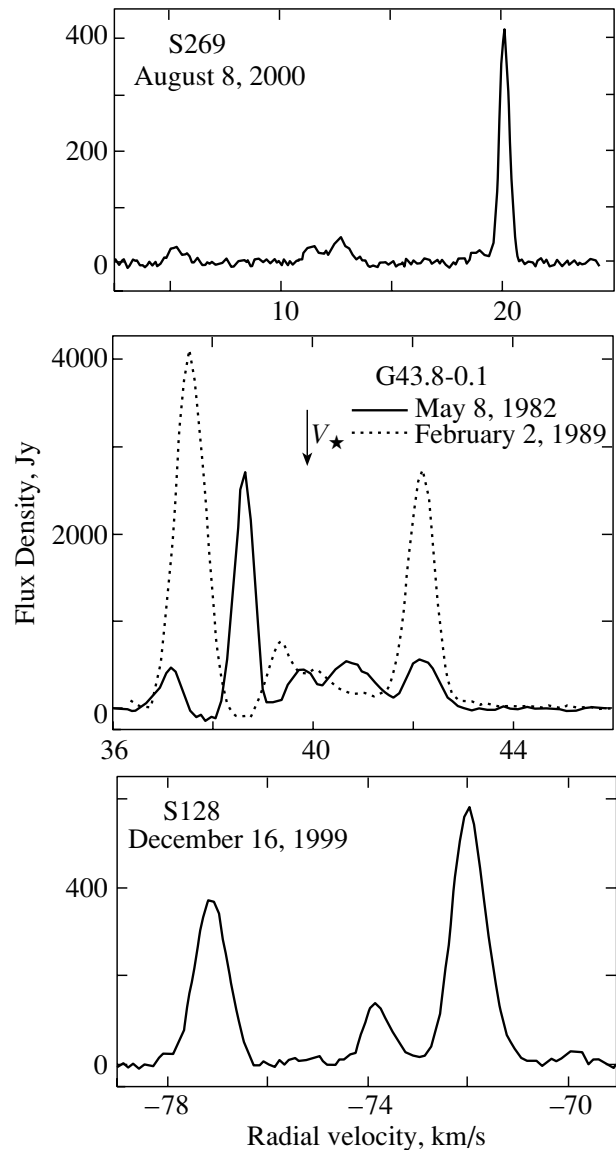
Fig. 2. H_2O spectra.

Since the maser emission is highly variable in time, to compare the line profiles at different epochs, they were normalized in amplitude and centered in velocity. The centering stems from the fact that a radial-velocity drift of the emission features was observed in some cases. In addition, the random errors and the errors in the radial velocity were eliminated. This procedure was carried out for all line profiles.

For the source G43.8−0.1, which is identified with an expanding envelope, we chose two strong flares. One of them occurred in 1982 at $V_{LSR} = 38.6$ km s^{-1}. The flare lasted for about 8 months. The mean line FWHM was 0.4 km s^{-1}. Figure 3 shows five line profiles at epochs when the line intensities were high enough to study their shapes. The superposition of all
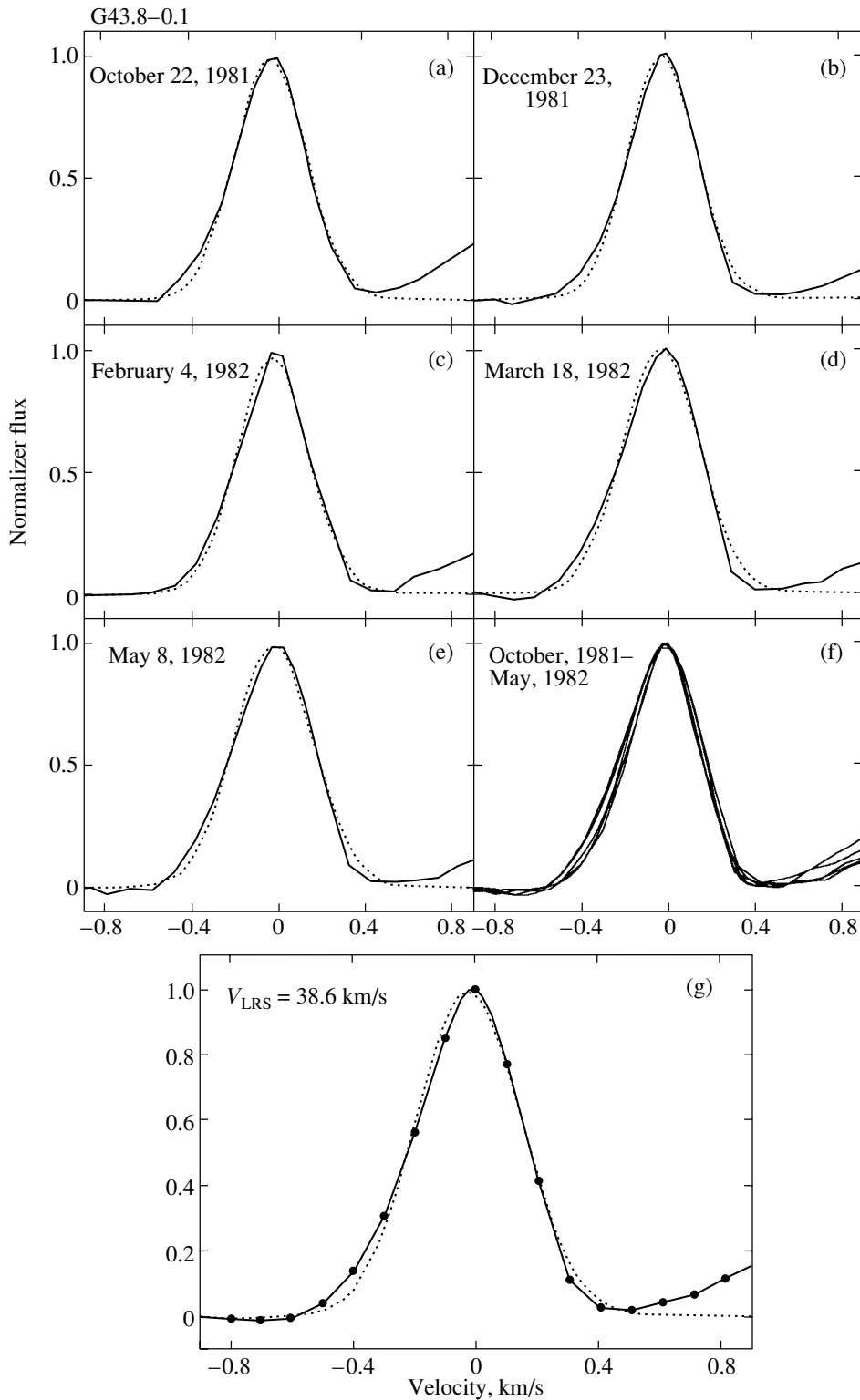
G43.8−0.1

Fig. 3. The 1981 flare at a radial velocity of 38.6 km s^{-1} in G43.8−0.1. The line profiles for five consecutive epochs with fitted Gaussians (a−e), the superposition of five lines (f), and the average line with a fitted Gaussian (g) are shown. The Gaussians are indicated by the dotted lines.

five line profiles is presented in Fig. 3f. The average line and the fitted Gaussian are shown in Fig. 3g.

During a different flare (1988−1990), the line at a radial velocity of 37.6 km s^{-1} was broader (Fig. 4a), of the order of 0.7 km s^{-1}. The line splitting into two components (Fig. 4b) was observed. The spectrum
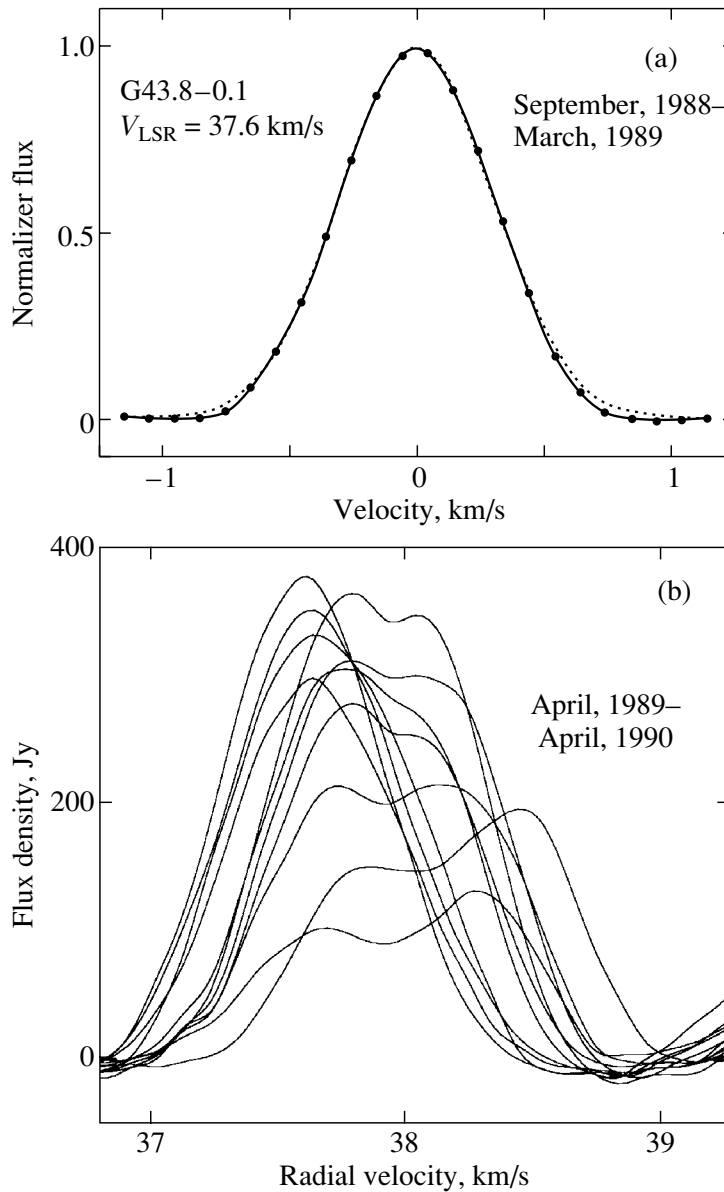
Fig. 4. The 1988−1990 flare in G43.8−0.1 at $V_{LSR} = 37.6$ km s^{-1}: (a) the average profile of 12 lines for the period September 1988−April 1989 and a fitted Gaussian (dotted line), (b) the line superposition when the line became asymmetric and then double (May 1989−April 1990).

of G43.8−0.1 exhibits a long-lived component at a radial velocity of 42.2 km s^{-1} (see Fig. 2), whose velocity was fairly stable. To study the radial-velocity drift of the 37.6-km s^{-1} feature, its velocity was measured relative to the 42.2-km s^{-1} feature. The results are presented in Fig. 5a. The flux and line-FWHM variations in the $\ln F - \Delta V^{-2}$ coordinates are shown in Fig. 5b.

In the H$_2$O spectrum of NGC 2071, we chose the component at $V_{LSR} \approx 17$ km s^{-1} and monitored its variability from October through December 1988. Figure 6a shows five spectra obtained on October

6; November 11, 12, 24; and December 21, 1988. The spectra are numbered 1 through 5, respectively. During this entire period, the line was asymmetric. We observed a small regular drift of the emission peak in radial velocity within 0.2 km s^{-1} and a rise in flux from 1740 to 2100 Jy with a simultaneous line narrowing from 0.82 to 0.61 km s^{-1}.

To compare the line shapes, all five profiles were reduced to the same minimum FWHM, which was observed on December 24, 1988. The lines were then centered to a zero velocity (Fig. 6b). The normalized lines closely coincide. Figure 6c shows the average line (*1*), which was fitted by two Gaussians (*2*). Their
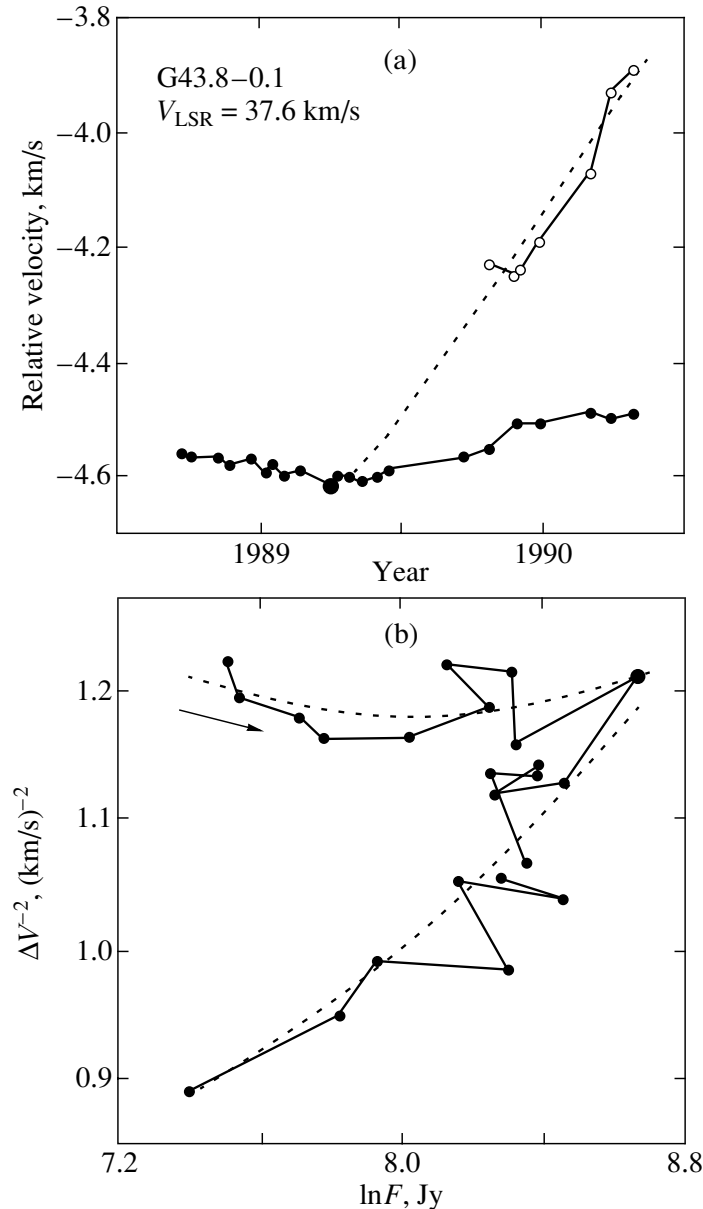
Fig. 5. (a) Radial-velocity variations of the emission feature at 37.6 km s^{-1} (of two components, *A* and *B*) in G43.8−0.1 relative to the 42.2-km s^{-1} feature and (b) the relationship between the flux and line FWHM for the same feature. The points were joined by straight lines to show their temporal sequence. The arrow indicates the direction of evolution. The large circle marks the flare maximum. The dashed line represents an extrapolation of the drift curve for component *B*.

sum is indicated in Fig. 6c by line *3*, which virtually coincides with the average line.

The results of our study of the asymmetry in the observed lines are presented in Fig. 7. For the left plot, distances from the line center and deviation of the observed line from the average line are along the horizontal and vertical axes, respectively. The average line was obtained as the ordinary mean of the left and right wings in the observed line, $\overline{F}(U) = (F_L(U) + F_R(U))/2$, where $F(U)$ is the emission flux. In this case, the deviation from the mean (along the horizon-

tal axis) can be written as $\overline{U} - |U_L|$ for the left wing of the line and as $\overline{U} - |U_R|$ for its right wing. In five cases, the line was asymmetric: S269, G43.8−0.1 (flare 1982), ON1 (the 15-km s^{-1} emission feature for two time intervals), and NGC 2071.

The difference in the patterns of the line FWHM variability for the symmetric and asymmetric lines is shown in the right-hand part of Fig. 7. Here, ΔU is the range within which the line FWHM varies as a function of the distance from its center. The letters L
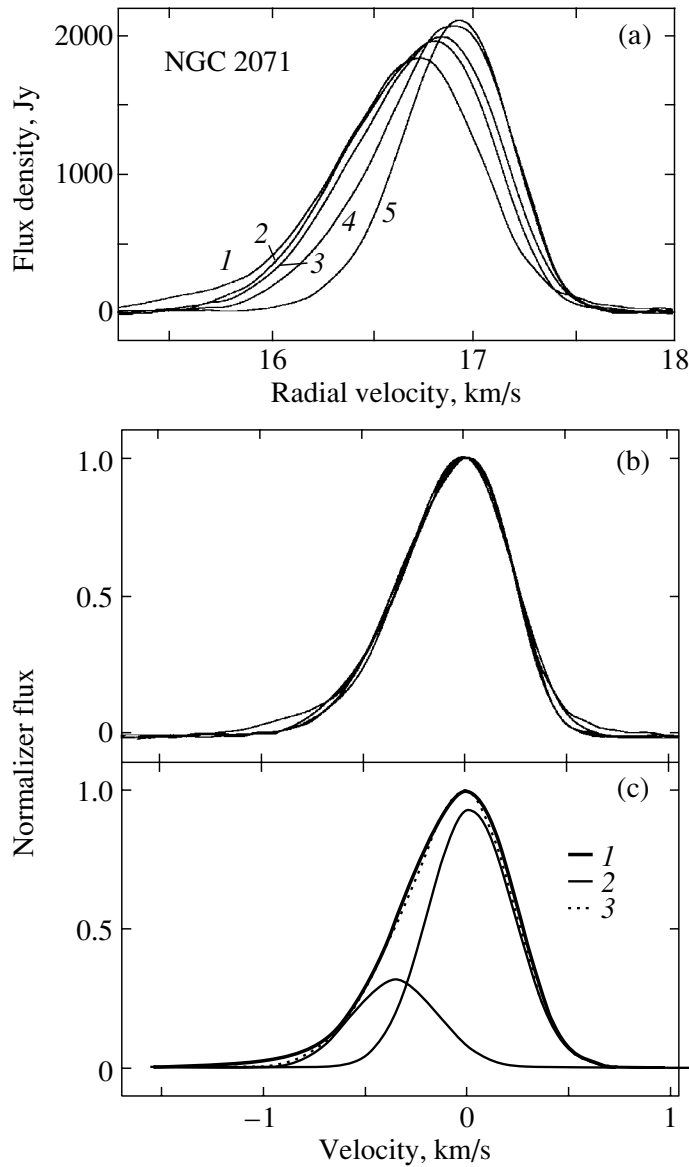
Fig. 6. (a) H_2O line profiles of the 16.9-km s^{-1} emission feature in NGC 2071 obtained during October−December 1998; (b) the superposition of lines normalized in the flux and line FWHM; (c) the average line and fitted Gaussians.

and R denote the curves for the left and right line wings, respectively.

DISCUSSION

The Source W75N

According to Torrelles *et al.* (1997), there are two main groups of maser spots in this region. One of them, W75N (Ba), that coincides with the ultracompact continuum source VLA 1 is elongated roughly in the direction of the bipolar molecular outflow. The group of spots W75N (Bb) that coincides with the the ultracompact continuum source VLA 2, forms a rotating protoplanetary disk. The separation between

the groups of maser spots does not exceed 1″. In single-dish observations, we receive the emission simultaneously from both H_2O masers.

The H_2O spectrum of the maser W75N (Ba) has a smaller velocity dispersion than W75N (Bb) (Torrelles *et al.* 1997). Therefore, the strong flare of 1999 at −2.6 km s^{-1} (Fig. 1c) may be assumed to have occurred in the maser W75N (Bb) identified with a Keplerian disk. The flare lasted no longer than 3−4 months. The line had a symmetric shape. Despite the significant flux variations, the line FWHM did not vary (0.67 km s^{-1}). Given that the line was broad and that there was no correlation between the flux and line FWHM variations, the maser may be assumed to
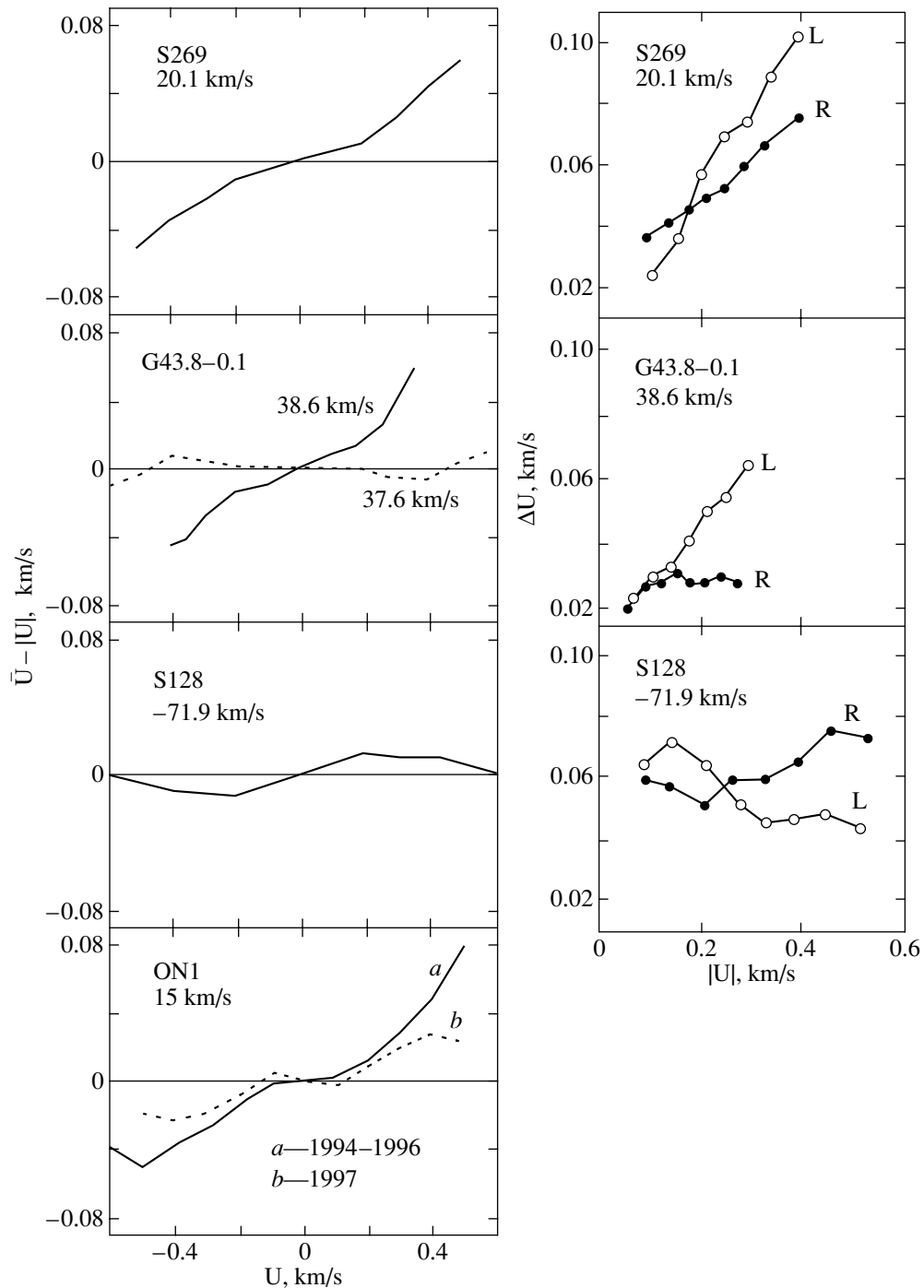
Fig. 7. Line asymmetry of individual H_2O maser emission components.

be saturated in this case. The flare was apparently local, because there were no significant variations in the H_2O spectrum as a whole during this period.

The maser W75N (Bb) has a complex spatial structure and contains a large number of maser spots (clumps of matter), which individually do not produce noticeable maser emission because of the insufficient optical depth. Since all these structures are involved in Keplerian motion, we cannot rule out a chance line-of-sight projection of two maser spots with similar velocities onto one another. In this case, a strong short flare can be observed, as in 1999.

Such short flares in W75N were observed in 1995–1997 (see Figs. 1a and 1b). The line shape of these emission peaks at the flare maximum was symmetric, and the line FWHM was 0.5–0.7 km s^{-1}.

Outside the peaks, there was no significant excess of emission of these short-lived components over the others. Therefore, for these periods, we cannot obtain the actual estimate of their line shape.

The Source G43.8−0.1

During the 1982 flare, the line was narrowest: the minimum FWHM was 0.35, and the mean was 0.4 km s^{-1}. The line had an asymmetry of ~11% (Figs. 3 and 7). The flare duration was estimated to be 6−7 months. Despite the significant flux and line FWHM variations, the asymmetry was preserved. There was a correlation between the flux and line FWHM variations, which is typical of an unsaturated maser (Mattila *et al.* 1985). No radial-velocity drift of the line was observed, which argues for the absence of any appreciable radial-velocity gradient in the line generation region.

If the Doppler line width is taken to be 2 km s^{-1}, then the observed line at maximum will be narrower than the Doppler one by almost a factor of 6, which corresponds to an amplification increment at the line center of $\tau \sim 35$. This is enough to account for the high brightness temperature in maser spots ($T_B \approx 10^{15}$ K) that requires an amplification of at least $\sim 10^{10}$ (Strel'nitskii 1982). The observed line was so narrow that even the assumption of simultaneous emission from the two closest hyperfine-structure components of the $6_{16}-5_{23}$ transition cannot explain its considerable (11%) asymmetry. Indeed, at a separation between the two closest components of 33 kHz (0.44 km s^{-1}), the observed line cannot be fitted by the superposition of two Gaussians. Therefore, we may assume that in this source (in a maser spot), only one hyperfine-structure component is amplified.

In contrast to the left wing, the right line wing (Fig. 3g) is satisfactorily fitted by a Gaussian. At a distance larger than 1.5 FWHM from the line center, the left line wing is greatly raised with respect to the Gaussian. The deviations from the Gaussian are much larger than those that can be for an unsaturated maser (Strel'nitskii 1982). The observed line asymmetry may be related to the spot geometry, i.e., the spot may have a more complex spatial structure than simply a homogeneous clump of matter.

The 1988−1990 flare differed significantly from the 1982 flare. The line was broader and initially symmetric (Fig. 4a). As the flare developed until its maximum (September 1988−March 1999), the velocity of the emission feature decreased. The change in velocity was 0.05 km s^{-1} (Fig. 5a). Such an accuracy was achieved because the velocity was measured relative to the fairly stable component at 42.2 km s^{-1}. The

line FWHM varied within a narrow range of radial velocities (0.67−0.80 km s^{-1}), and no correlation with the flux variations was observed. The observed line FWHM variations were most likely erratic (Fig. 5b). The absence of a correlation between the line FWHM and flux variations, its relatively large FWHM, and the symmetry are a possible argument for a saturated maser.

After the flare maximum, the drift direction reversed. The drift in this direction continued for 1 year. In addition, the line broadened immediately after the flare maximum and half a year after the maximum, the second component B appeared in the spectrum (Fig. 4b), which receded from the main component A. The velocity of the latter (A) increased in this time by 0.1 km s^{-1}; the velocity of component B increased by 0.7 km s^{-1}, if it is assumed to have appeared immediately after the maximum. Indeed, extrapolation indicates that component B emerged at the flare maximum (Fig. 5a), as confirmed by Fig. 5b. In addition, an analysis of the line shape showed that the line was slightly asymmetric at the emission maximum (the March 31, 1989 spectrum): the right line wing was higher than the left one. The asymmetry was ≈4%. Thus, our study of the line shape allowed us to refine the occurrence time of the second component.

The radial velocity of the central star in G43.8−0.1 is estimated to be ≈40 km s^{-1} (Lekht and Sorochenko 1999). Thus, we can explain the observed variations in the line radial velocity and shape as follows. The motion of the maser condensation at $V_{LSR} = 37.6$ km s^{-1} was initially accelerated relative to the central star. At the time corresponding to the emission maximum, the deceleration in a dense medium (or collisions) resulted in a breakup of the condensation into two parts. That is why there was no further rise in flux and its decline began. During the interaction with a dense medium, the motion of both components slowed down, which accounts for the reversal of the drift direction. The deceleration of component B was larger than that of component A.

The variety of the flares that occurred in G43.8−0.1 is not limited to the cases considered. As an example, we can note the 1997 flare (Lekht 2000), which occurred at a radial velocity of 38.2 km s^{-1}. The flare lasted ~1 year. The line was narrow and symmetric; its minimum and maximum FWHMs were 0.43 and 0.6 km s^{-1}, respectively. We observed the flux-correlated line FWHN variations that are well described by relation (1). In addition, there was a radial-velocity drift of the feature during the flux rise.

The Source NGC 2071

According to Torrelles *et al.* (1998), there are two groups of maser spots in this region, which are associated with compact H II regions and the IR sources

IRS 1 and IRS 3. One of them located near IRS 1 is extended along a jet. The other group of spots associated with IRS 3 forms a rotating protoplanetary disk whose plane is perpendicular to the jet axis.

For the component at $V_{LSR} \approx 17$ km s^{-1}, we observed a small, regular velocity drift of the emission peak from 16.7 to 16.9 km s^{-1}. The high rate of change in the radial velocity of the maser in a protoplanetary disk seems unlikely. In addition, the component at ≈ 17 km s^{-1} must be on the periphery of the Keplerian disk in the red amplification corridor (Torrelles *et al.* 1998). As was noted previously, the rate of change in the radial velocity here is at a minimum. This maser spot is most likely located near IRS 3 and is, thus, associated with the jet.

We were able to closely fit the normalized profile by two Gaussians of the same width (0.46 km s^{-1}) and with an amplitude ratio of 3 : 1. The equality of the line FWHMs is apparently not accidental and can be evidence that the emission originates from a single spot with a nonuniform density. The flux difference between the two components by a factor of 3 (unsaturated maser) requires a difference between τ no more than 5% ($\tau \approx 20-25$ at the line center), which essentially does not result in a line FWHM difference.

The coincidence of the line shapes for the normalized profiles also rejects the model of the approach of two maser spots in radial velocity, i.e., when they move toward each other along the line of sight. It is unlikely that for such an approach of the features during a short period (2.5 months), both features simultaneously narrowed. In addition, to preserve the shape of the normalized lines, only small flux variations are admitted.

The line asymmetry may be assumed to be caused by a radial-velocity gradient at a nonuniform density of the matter. Previously, we assumed this emission feature to be associated with a molecular jet. The radial-velocity gradient may have changed, which caused a change in the profile of the amplification factor of the medium. A wave (not a shock) probably passed through the jet, which changed the radial-velocity gradient of the medium whose H_2O molecules were involved in the maser line formation. Initially, the gradient decreased, resulting in a line narrowing and in a displacement of the emission peak in the H_2O spectrum. Subsequently, the gradient again increased, resulting in a line broadening and in a reverse radial-velocity displacement of the line peak.

Other Sources

Our monitoring of the source ON1 allowed us to trace the evolution of the emission at $V_{LSR} =$ 15.5 km s^{-1} over more than 15 years. We chose two time intervals (1994−1996 and the entire 1997), when this emission feature was not blended with others. Within each interval, the line FWHM changed only slightly and the line itself was asymmetric (its profiles are not given here). Between these intervals, the line broadened from 0.58 to 0.69 km s^{-1}, while the line asymmetry decreased from 12 to 7%. These facts indicate that the maser spot must have a more complex structure than a homogeneous clump of matter. In addition, there may be small-scale turbulent motions both in the maser spot and in its surroundings.

The line shape of the 20-km s^{-1} component in the source S269 was studied previously (Lekht *et al.* 2001). It was shown that the line had an asymmetric shape and its radial velocity varied according to a sinusoidal law with a period of 26 years. As the model, we proposed a rotating turbulent vortex located at the center of the red amplification corridor of a Keplerian disk. Here, we numerically estimated the line asymmetry. The mean asymmetry for the entire monitoring of S269 is $\sim 11\%$.

In S128, the H_2O emission in the radial-velocity range from -73 to -70 km s^{-1} was continuously observed during our entire monitoring. The emission from several features alternately appeared in this part of the spectrum. Since 1998, the emission has originated from a single feature with a mean radial velocity of -71.9 km s^{-1}. The line shape was symmetric. There was a correlation between the flux and line FWHM variations (Lekht *et al.* 2002), characteristic of an unsaturated maser. The absence of line asymmetry indicates that the model of a homogeneous maser spot is most plausible.

Asymmetric lines are common in the H_2O maser spectra. The causes of the asymmetry can be density nonuniformities and a radial-velocity gradient (including a gradient nonlinear along the line of sight) in the masing region (maser spot).

In addition, we explored the possibility of absorption of the emission in the medium near the maser spot. The molecules in this medium and in the spot have similar radial velocities; the difference is that they have no inverse level populations. The results of such studies will be presented in a forthcoming publication.

The line asymmetry, together with the flux and radial velocity, is an important parameter for choosing a maser spot model. Collectively, these characteristics of maser emission make it possible to study the structure of maser spots and their interaction with the medium where they are localized.

CONCLUSIONS

Below, we present our main results.

(1) The shapes of the emission components of H_2O maser sources in star-forming regions can be both symmetric and asymmetric. The asymmetry, i.e., the deviation from a symmetric line of the same FWHM, ranges from 5 to 15%.

(2) Despite the variations in the flux and FWHM of the single asymmetric line, its asymmetry was preserved (S269, G43.8−0.1, and ON1).

(3) The strong short flares of H_2O emission in W75N (Bb), which is identified with a protoplanetary disk, could result from a chance projection of numerous clumps of matter onto each other.

(4) As the 1988−1990 flare developed in G43.8−0.1, the emission feature at 37.6 km s^{-1} broke up into two components. We found a small drift of both components with different radial velocities. The breakup of the condensation responsible for the emission at 37.6 km s^{-1} into two parts could be caused by its interaction with the dense envelope matter.

(5) In NGC 2071, we observed a narrowing of the asymmetric line ($V_{LSR} \approx 16.8$ km s^{-1}) with the simultaneous displacement of the emission peak in radial velocity. This phenomenon can be explained by the passage of some wave (not a shock) that changed the radial-velocity gradient of the medium where the maser emission originated.

ACKNOWLEDGMENTS

REFERENCES

1. P. Goldreich and J. Kwan, Astrophys. J. **190**, 27 (1974).
2. E. E. Lekht, Astron. Astrophys., Suppl. Ser. **141**, 185 (2000).
3. E. E. Lekht and R. L. Sorochenko, Astron. Zh. **758**, 76 (1999) [Astron. Rep. **43**, 663 (1999)].
4. E. E. Lekht, S. B. Likhachev, R. L. Sorochenko, and V. S. Strel'nitskii, Astron. Zh. **70**, 731 (1993) [Astron. Rep. **37**, 367 (1993)].
5. E. E. Lekht, J. E. Mendoza-Torres, and N. A. Silant'ev, Astron. Zh. **76**, 248 (1999).
6. E. E. Lekht, N. A. Silant'ev, J. E. Mendoza-Torres, *et al.*, Astron. Astrophys. **377**, 999 (2001).
7. E. E. Lekht, J. E. Mendoza-Torres, and I. I. Berulis, Astron. Zh. **79**, 63 (2002) [Astron. Rep. **46**, 57 (2002)].
8. K. Mattila, N. Holsti, M. Toriseva, *et al.*, Astron. Astrophys. **145**, 192 (1985).
9. L. I. Matveenko, Pis'ma Astron. Zh. **7**, 100 (1981) [Sov. Astron. Lett. **7**, 54 (1981)].
10. L. I. Matveenko, L. R. Kogan, and V. I. Kostenko, Pis'ma Astron. Zh. **6**, 505 (1980) [Sov. Astron. Lett. **6**, 279 (1980)].
11. L. I. Matveenko, P. J. Diamond, and D. A. Graham, Astron. Zh. **77**, 669 (2000) [Astron. Rep. **44**, 592 (2000)].
12. R. L. Sorochenko, M. M. Berulis, V. A. Gusev, *et al.*, Tr. Fiz. Inst. Akad. Nauk SSSR **159**, 50 (1985).
13. V. S. Strel'nitskiĭ, Usp. Fiz. Nauk **113**, 463 (1974) [Sov. Phys. Usp. **17**, 507 (1974)].
14. V. S. Strel'nitskiĭ, Pis'ma Astron. Zh. **8**, 165 (1982) [Sov. Astron. Lett. **8**, 86 (1982)].
15. J. M. Torrelles, J. F. Gómes, L. F. Rodríguez, *et al.*, Astrophys. J. **489**, 744 (1997).
16. J. M. Torrelles, J. F. Gómes, L. F. Rodrígues, *et al.*, Astrophys. J. **505**, 756 (1998).

Translated by G. Rudnitskiĭ